INVESTIGATING THE PERFORMANCE OF LAMINATED GLASS PANELS UNDER WINDBORNE DEBRIS IMPACT

G.C.S. Jayaweera

228001N

Master of Science (Major Component of Research)

Department of Civil Engineering

Faculty of Engineering

University of Moratuwa

Sri Lanka

December 2023

INVESTIGATING THE PERFORMANCE OF LAMINATED GLASS PANELS UNDER WINDBORNE DEBRIS IMPACT

G.C.S. Jayaweera

228001N

Thesis submitted in partial fulfilment of the requirements for the degree

Master of Science (Major Component of Research)

Department of Civil Engineering

Faculty of Engineering

University of Moratuwa

Sri Lanka

December 2023

DECLARATION

I declare that this is my own work and this thesis does not incorporate without acknowledgement any material previously submitted for a degree or diploma in any other University or Institute of higher learning and to the best of my knowledge and belief it does not contain any material previously published or written by another person except where the acknowledgement is made in the text. I retain the right to use this content in whole or part in future works (such as articles or books).

Signature: UOM Verified Signature Date: 30/12/2023

The above candidate has carried out research for the MSc thesis under my supervision. I confirm that the declaration made above by the student is true and correct.

Name of Main Supervisor: Dr. H.G.H. Damruwan

Signature of the Main Supervisor: UOM Verified Signature Date: 30/12/2023

Name of Co-Supervisor: Dr. B. Baleshan

Signature of the Co-Supervisor: UOM Verified Signature Date: 30/12/2023

DEDICATION

In profound appreciation, I dedicate this thesis to my cherished parents.

ACKNOWLEDGEMENT

Foremost, I would like to express my profound gratitude to my research supervisors, Dr. H.G.H. Damruwan and Dr. B. Baleshan for their great support and unwavering guidance, which have played a pivotal role in the successful completion of this study. I am immensely grateful for the opportunity to work as a research student in their esteemed research group. Without their guidance, the fruition of this study would not have been possible.

I wholeheartedly appreciate the support and guidance provided by the Faculty of Graduate Studies, University of Moratuwa, Sri Lanka during my research.

I greatly acknowledge the enormous support, valuable suggestions, and advice given by the examiners Dr. K. Baskaran, Dr. L.B. Jayasinghe, and Dr. A.U. Weerasuriya throughout the research period, enabling me to excel in this research work. Furthermore, in profound appreciation, I would like to extend my deepest gratitude to Prof. H.M.Y.C. Mallikarachchi and Dr. A.U. Weerasuriya for granting access to high-performance computing facilities essential for conducting finite element modelling and analysis in this research.

I would like to acknowledge all the academic and non–academic staff members at the Department of Civil Engineering, University of Moratuwa, Sri Lanka for their invaluable support and assistance in various capacities.

I am grateful to all of my teachers who guided me during my preschool and school years, as well as my parents and family members who have encouraged me with positive encouragement.

Finally, I am taking this great opportunity to thank my friends for their valuable comments and support in completing this research study.

G.C.S. Jayaweera

Department of Civil Engineering,

Faculty of Engineering,

University of Moratuwa, Sri Lanka

December 2023

ABSTRACT

Glass façades, a prominent feature in modern buildings, have garnered widespread popularity despite the inherent brittleness of glass due to its non-crystalline molecular structure. While glass is commonly utilised as a structural material following quality and performance enhancement measures, its susceptibility to extreme loads, particularly impact loads, is higher compared to other structural elements. Past investigations into windstorms have revealed that the generation of various debris poses a significant threat to glass façades during extreme wind conditions. This research addresses the imperative need to comprehensively study the response of Laminated Glass (LG) panels to windborne debris impact, emphasising the potential consequences of damage during windstorms. LG, known for its safety features and higher post-crack load carrying capacity, is employed in buildings. The study focuses on fully framed LG window panels and employs a finite element (FE) based numerical modelling approach to assess their impact performance. The FE models are validated using results from past experiments, and subsequent examinations explore the impact performance of LG panels and their constituent components under various critical impact locations. Key findings suggest that support conditions and impact locations significantly influence the LG panel's impact performance. The Polyvinyl Butyral (PVB) interlayer plays a crucial role in resisting penetration by absorbing substantial impact energy. The study advocates purposeful design of LG window panels as sacrificial elements to enhance impact resistance, rather than relying solely on thicker glass panes. Energy absorption is found to be highest for mid-impacts, diminishing for long-span mid-impacts, short-span mid-impacts, and corner impacts, respectively. The research highlights the importance of an iterative design process for impact-resistant glazing, emphasising the need for designers to propose suitable layer thicknesses and configurations. Failure to do so may result in additional material costs without achieving satisfactory impact resistance. Hence, the findings of this research encourage manufacturers to create innovative materials with strong energy absorption, enabling engineers to implement impact-resistant glazing for safe, optimised, and aesthetically pleasing glass façades in cyclone-prone areas.

Keywords: Windborne debris impact; Impact-resistant glazing; Laminated glass; Finite element modelling; Material failure

TABLE OF CONTENTS

LIST OF FIGURES

LIST OF TABLES

LIST OF ABBREVIATIONS

Abbreviation	Description
AITHM	Australian Institute of Tropical Health and Medicine
ASCE	American Society of Civil Engineers
AS	Australian Standard
ASTM	American Society for Testing and Materials
AS/NZS	Australian/New Zealand Standard
CST	Central Standard Time
CTS	Cyclone Testing Station
FE	Finite Element
IDL	International Date Line
IMOC	Integrated Marine Operations Centre
LG	Laminated Glass
PDMS	Polydimethylsiloxane
PVB	Polyvinyl Butyral
SAA	Standard Association of Australia
SG	SentryGlas®
SGP	SentryGlas® Plus
SHPB	Split Hopkinson Pressure Bar
SLS	Serviceability Limit State
TPU	Thermoplastic polyurethane
TR 440	Technical Record 440
ULS	Ultimate Limit State
UTC	Coordinated Universal Time

CHAPTER 1

INTRODUCTION

1.1 Background

The building façade acts as an interface between the exterior and interior environment of a building. “Façade” is a word from the French language that has a meaning of frontage. Building façades can be considered as the skin of a building providing good appearance and protection to the building. Structural and building envelope elements can be seen in façades. Required horizontal and vertical resistance to the loads acting on the façades are provided by the structural elements of the façades. Building envelope elements are designed to comply with the required weather, fire, sound, and thermal resisting properties. The Glass façade is one of the most frequently used façade types in modern Civil Engineering projects. Good aesthetic appearance, visual comfort, and environmental compatibility can be achieved by using glass façades. Annealed, heat-strengthened, and fully tempered glass are the three main types of glass that can be categorized depending on their manufacturing process. The supporting structure, window frame, glass panel, and fasteners are the four main components that can be seen in glass façades. Annealed, heat-strengthened, and toughened glass are three primary glazing materials frequently utilised in glass façades. They can also be utilised as laminated glass (LG) (Hidallana-Gamage, 2015) or as components of an Insulated Glass Unit. Figures 1.1(a) and 1.1(b) showcase two captivating glass façade structures.

(a) Aldar Headquarters, Abu Dhabi (Wikipedia, 2013)

(b) The Parada Store, Tokyo (Architectuul, n.d.)

Figure 1.1 - Buildings with innovative glass façades

Different types of glass façades are used in the industry depending on the purpose of the building, regulatory criteria, architectural requirements, and aesthetic appearance, desired thermal comfort levels, loading, and other structural requirements, cost, sustainability aspects, preferences of the owners, etc. The cost of the glass curtain walls

is approximately 5 – 20% of the total cost of the building (Pratama & Susetyo, 2019). According to the available literature, the cost of a building envelope may be up to 25% of the total construction cost of a particular building (Kragh, 2011). Façade can be considered as one of the largest elements of a building which can significantly affect the sustainability of a building project (Gilani, 2020). Building façade acts as a major element of a building which contributes around 60% of the heat loss (Zavadskas et al., 2008). Therefore, care must be taken while designing building façades to achieve the expected requirements.

Façade engineers have a responsibility to prepare the technical and project-specific documents for the building façades and come up with reliable structural systems. Glass has a non-crystalline molecular structure. So, glass is a brittle material that is weak in tension (Makwana, 2013). However, with the help of proper quality improvement processes and performance analysis tools, glass is currently used as a structural material. Since glass is a frequently used material in the façade industry, it is very important to investigate the performance of different types of glass façades. Without following correct design methods, the expected performance of glass façades could not be achieved and unexpected failures might occur in glass façades. Extreme wind conditions, blasts, debris impacts, and earthquakes can be mentioned as some predominant events that can increase the vulnerability of the glass façades. Panel failures, connection failures, and façade frame failures are the common types of façade failures that can be seen (Powar & Jayachandran, 2021). There can be external faults and intrinsic faults that will lead to glass façade failures. External faults can be divided into two main categories such as man-made and natural. Accidental damages, purposeful damages, surface damages, and unaccounted extreme loadings can be mentioned as some man-made external faults. Thermal stresses, environmental conditions, pressure variations, moisture conditions, etc. can be considered as natural external faults. Stress concentrations, deteriorations in façade elements, impurities, low ductility properties, etc. can be categorized under the intrinsic faults for glass façade failures (Honfi et al., 2014). Moreover, errors during the manufacturing process, mistakes during transportation and storage, design errors, construction errors, potential deficiencies in design codes, and maintenance issues are some of the possible factors that can lead to failures in glass façades. (Honfi et al., 2014).

Most of the time curtain walls act as a barrier safeguarding the building and its occupants from adverse climatic conditions, windborne debris impacts, vicious attacks, etc. (Taywade & Shejwal, 2015). The research study which is presented in this thesis discusses the response of glass façade with LG panels to windborne debris impact. Previous windstorm investigation studies revealed that windborne debris is one of the major sources of damage to the building envelope elements during heavy wind conditions such as cyclones, hurricanes, and tornadoes (Minor & Mehta, 1979; Walker, 1991). Damages to the glass façades will result in unexpected damages to the building's occupants and other contents exposing them to continued wind flows, raindrops, and ejected glass fragments. When a windward glass façade is damaged forming structure openings, it leads to an increase in the internal pressure in the

building. Therefore, the outward-acting pressure on the façade also increases. As a result of this phenomenon, the internal pressure coefficients and the net outward-acting pressure will increase by a factor of four and two respectively (American Society for Testing and Materials (ASTM) E 1886-05, 2005). It has been found that the flying glass fragments which are ejected from fractured glass panels can cause severe casualties to the building occupants (Zhang et al., 2013). Therefore, it is observed that windborne debris impact on glass façades will cause unexpected damages to the building properties, its occupants, and neighbours. So, they will consume extra cost and time to carry out the required rectifications and replacements which may severely affect the safety, cost-effectiveness, reputation of the project authorities, and feasibility of the projects. Figures 1.2 (a) and 1.2 (b) show damaged glass façades due to windborne debris impact.

Therefore, it is very important to follow the design codes and use correct methods while designing impact-resistant glass façades. Nowadays, glass façades are frequently used for building envelopes. Therefore, it is required to obtain required technical support from the façade engineers to come up with innovative, structurally viable, practical façade designs. Proper methods should be followed during the refurbishment of existing façades as well.

(a) Failure of a glass panel (Powar & Jayachandran, 2021)

(b) Damages to the glass façade of Hyatt Regency Hotel, New Orleans (Nayer, 2011)

Figure 1.2 - Damaged glass façades due to windborne debris impacts

Some design engineers use design codes for designing glass facades. Some contractors use rules of thumb and their experience for selecting façade materials and designing glass facades as well (Fowza & Hidallana-Gamage, 2020). However, there is no proper investigation done to date to check the accuracy of using these rules of thumb. There can be some differences between the rules of thumb and design standards. Moreover, glass facades should be structurally viable under different types of loadings such as wind loads, earthquake loads, blast loads, impacts, fire, etc. If the designers neglect these possible load conditions, errors might occur in the predictions, analysis results, and the final design. Therefore, a proper investigation should be carried out to check

the performance of glass facades used in buildings under different loading conditions. This research is mainly focused on the windborne debris impact phenomenon.

The response of glass façades to windborne debris impacts can be investigated using numerical analysis methods with Finite Element (FE) software. Standard lab experiments can be used to validate the results from these FE codes as well. However, in the Sri Lankan context, only limited research has been done on glass façades and their performance. Therefore, this research will investigate the performance of LG panels used in buildings under windborne debris impact using the LS-DYNA FE code and previous laboratory experiments. The findings of this research work will help design engineers to make the correct decisions on selecting façade materials and come up with safer designs for impact-resistant glazing.

1.2 Research Problem

Glass façade is one of the most popular façade types which is used as the building envelopes. It is evident that glass has a non-crystalline molecular structure. Therefore, glass is a brittle material in nature which is weak in tensile stresses (Makwana, 2013). However, glass is being used not only as a transparent infill material but also, it is being used as a structural material in projects with the help of quality improvement processes such as heat tempering, heat strengthening, and chemical strengthening (ABRISA Technologies, n.d.; Swift Glass, 2016). Laminated glass (LG) is a type of safety glass which is frequently used in modern impact-resistant glazing.

Although most of the current design standards and test methods provide some guidelines for impact-resistant glazing, they do not explain enough justifications for their suggestions and do not discuss the influence of the different controlling parameters on the impact resistance of LG panels. Moreover, the cost and risk which are associated with the standard windborne debris impact tests on LG panels is comparatively higher. Therefore, a research study with comprehensive analysis is required on this phenomenon to overcome these limitations and shortcomings of the available design standards and testing methods.

Numerical modelling and analysis with FE software is one of the methods which has been suggested by previous research studies to predict the behaviour of LG panels to windborne debris impacts (Shetty et al., 2013; Zhang et al., 2014; Zhang et al., 2013). Although there are several research studies on this research area, there is limited knowledge on the influence of the impact locations and the support conditions on the impact behaviour of building façades fabricated with LG panels. Hence, this research study will examine the influence of support condition and impact location on the impact performance of LG panels and it will develop design strategies for impact-resistant glazing.

1.3 Aims and Objectives

The main aim of this research is to develop design strategies for impact-resistant glazing of building envelopes considering the response of the laminated glass (LG) window panels under different support conditions and impact locations. The following research objectives were set to achieve this research aim.

- Identify the different types of glass façades fabricated with LG panels used in buildings
- Compare the current design standards and standard testing methods associated with debris impact criteria
- Develop and validate the FE-based numerical techniques to investigate the behaviour of LG panels under different support conditions and impact locations
- Evaluate the performance of structural silicon sealant material and LG panel subjected to impacts at different impact locations
- Formulate design strategies for impact-resistant glazing

1.4 Research Scope

The scope of this research was limited to examining the behaviour of building façades fabricated with LG panels under windborne debris impacts. Cyclonic effects are frequently observed in both Australia and the United States. Hence, Australian and ASTM standards are regarded as the most dependable standards for windborne debris impact resistance. In contrast, Eurocode provides limited details on this aspect compared to the comprehensive details available in Australian and ASTM standards. Consequently, Australian/New Zealand (AS/NZS) and ASTM standards were considered in this study. As it has been suggested by international standards such as Australian/New Zealand (AS/NZS) 1170.2: 2011 and ASTM E 1886 – 05, a timber test member with a nominal cross-section of 100 mm × 50 mm and a mass of 4 kg was selected as the windborne debris. Therefore, this research was focused on the large missile test on LG panels. Although the impact locations cannot be controlled during a windstorm event, the impact locations which have been suggested in the standard, ASTM E 1996 – 09 were considered during this study to check the behaviour of LG panels with different impact locations.

The FE models were developed using the LS-DYNA explicit FE code. Since the studies were limited to numerical analysis, the FE models were validated using the results from previous laboratory experiments. After that, those validated numerical models were used to examine the influence of different support conditions and impact locations on the impact performance of the LG panels. While developing FE models, deformations of the supporting frame of the LG panel were not considered concerning the simplicity of the models. Since this research is on the windborne debris impact, the studies were mainly focused on buildings at the international level.

1.5 Significance of the Research

It is important to design glass façades against windborne debris impacts to confirm occupant safety and to prevent internal pressurisation. However, a lack of specificity can be seen in windborne debris impact on glass façades in the current design standards. For example, only a single clause regarding the windborne debris impact has been provided in the standard, AS/NZS 1170.2: 2011. Moreover, proper reasons have not been discussed for most of the suggestions and guidelines which have been codified in the standards (Williams & Redgen, 2012). Furthermore, the influence of the different parameters such as impact location and support conditions of the panel on the performance of LG panels under windborne debris impacts has not been discussed in the most of the research studies to date.

This research develops a FE-based analytical procedure to investigate the response of LG panels to windborne debris impacts. In addition to that, it develops design strategies for impact-resistant glazing based on the results from the current study. Therefore, this research will provide new information on the impact performance of LG panels and will help façade engineers to design glass façades fabricated with LG panels against windborne debris impacts optimizing the façade structures. Moreover, the comprehensive numerical techniques that have been developed in this research can be extended to simulate the other impact phenomenon on LG panels as well. Therefore, the accumulated knowledge of this research can be used to understand the impact performance of LG panels and to identify the possible design methods to improve the impact resistance of the LG panels.

1.6 Thesis Outline

In this thesis, a comprehensive study on the response of LG panels to windborne debris impacts is presented. A FE based analytical procedure with a comprehensive numerical approach was followed to perform the analysis in this research study.

The outline of the thesis is given below.

i. Chapter 1: Introduction and background of the research. The research problem, aims and objectives, scope, and significance of the research are described in this chapter.

ii. Chapter 2: In this chapter, a comprehensive literature review is presented on the manufacturing process of glass, windborne debris impact phenomenon, design standards and standard test methods for impact-resistant glazing, different impact-resistant glazing methods, case studies on selected glass façades located in cyclone-prone areas, material behaviour of LG composites under impact loads, previous experimental studies, and development of FE models for simulating windborne debris impact on LG panels. At the end of this chapter, a summary is given to highlight the literature review findings and knowledge gaps.

iii. Chapter 3: Research framework and methodology are presented here providing a detailed description of the FE modelling and numerical approach that was followed in this research.

iv. Chapter 4: This chapter contains the validation of the FE-based numerical techniques using previous experimental results.

v. Chapter 5: The response of the LG panel when subjected to an impact at its geometric centre is discussed here. Furthermore, the effects of support conditions and glass thickness on the impact performance of the LG panel are also discussed in this chapter.

vi. Chapter 6: The discussion presented in this chapter pertains to the response of the LG panel when subjected to windborne debris impact at distinct locations of the panel.

vii. Chapter 7: This chapter contains a summary of the overall research process, main findings, design strategies, limitations of the present research, and recommendations for future work.

CHAPTER 2

LITERATURE REVIEW

2.1 Introduction

This chapter presents a comprehensive literature review. There are nine sections (Sections 2.1 to 2.9) in this chapter. The content of each section of Chapter 2 is briefly discussed in this section.

Section 2.2 contains the manufacturing process of annealed glass and laminated glass (LG). Section 2.3 provides a detailed introduction to the windborne debris and windborne debris impact phenomenon. In addition, Section 2.3 presents the details of an in-depth investigation of cyclone-prone regions. The Asia-Pacific region is the cyclone-prone region that was selected for the in-depth investigations. At the end of Section 2.3, possible threats to the glass façades are illustrated by conducting hazard studies on windborne debris impacts. The codes and standards for impact-resistant glazing and their limitations are explained in Section 2.4. The modern impact- and cyclone-resistant façade technologies are described in Section 2.5. Section 2.6 presents the details of the case studies conducted on the selected glass façades located in cyclone-prone areas to identify the design requirements, codes and guidelines, design phase considerations, and design principles associated with glass façades. The Integrated Marine Operations Centre (IMOC), Port Hedland, Australia, and the Australian Institute of Tropical Health and Medicine (AITHM), Townsville, Australia are the two structures selected for the case studies. Section 2.7 discusses the material behaviour and failure criteria of different materials in LG composites under dynamic loads. Section 2.8 reviews the previous research studies conducted to study the behaviour of LG window panels under windborne debris impacts highlighting their limitations. At the end of Chapter 2, Section 2.9 summarises the main findings of the literature review, the research gap, and the strategies adopted to address the identified research gap.

2.2 Manufacturing Process of Glass

Glass is brittle in nature. Randomly distributed surface flaws and scratches lead to brittle fractures in glass. With the modern advances of technology, glass is used as structural members in building façades. Annealed (float) glass, heat-strengthened glass, and fully tempered (toughened) glass are the three main types of glass which can be categorised based on their manufacturing process. Annealed glass is subjected to the reheating and cooling process while producing both the heat-strengthened and fully tempered glass. Laminated glass (LG) is a glass product that is manufactured by pasting a plastic adhesive interlayer material in between glass sheets. Both annealed and heat-strengthened glass break into larger fragments and adhere well to the interlayer after fracture. Therefore, they are usually recommended for laminated glass,

unlike tempered glass, which breaks into finer particles. The most commonly used interlayers in laminated glass are Polyvinyl Butyral (PVB) and Ionoplast. Thus, this section discusses the manufacturing process of annealed glass and LG because it aids in understanding the material composition, arrangement, and behaviour of LG.

2.2.1 The Float Glass Process

Annealed (float) glass is the basic glass type that is used in practice and it is flat glass which is produced by the float glass process. Sir Alastair Pilkington invented the float glass process and it was presented to the public on 20th of January, 1959. After that, the production was begun by the Pilkington Brothers Company, St, Helens, Great Britain. As a result of the invention of this new method, the previous methods of casting and blowing which were used in flat glass production were completely replaced (GW News, 2021). It has been estimated that nearly 970,000 tonnes of glass are produced by float lines in the world (Nippon Sheet Glass Co., Ltd., n.d.). Glass consists of Silica sand (SiO_2), Soda ash (Na_2O), Limestone (CaO), MgO, Alumina (Al_2O_3), and several other minor materials. In the early days, the Silica sand content of the float glass was about 73.7% (Holmquist et al., 1995). But, nowadays, considering the environmental aspects and sustainability of materials, float glass is produced with 51% of Silica sand which is comparatively lower than the percentage amount used in the early days (Zhang et al., 2012). Table 2.1 gives the percentage chemical composition of float glass.

Table 2.1 - Chemical composition of float glass

Percentage Chemical Composition (%)							
(Holmquist et al., 1995)	SiO_2	Na_2O	CaO	MgO	Al_2O_3	K_2O	Fe_2O_3
	73.7	10.6	9.4	3.1	1.8	1.1	0.2
(Zhang et al., 2012)	SiO_2	Na_2O_3	Cullet	$CaMg(CO_3)_2$	$CaCO_3$	Other	
	51	16	15	13	4	1	

Since this research investigates the response of LG which is manufactured by pasting an interlayer film (PVB interlayer) in between two float glass sheets, it is important to have an idea about the manufacturing process of float glass. Figure 2.1 shows a schematic diagram of the float glass manufacturing process.

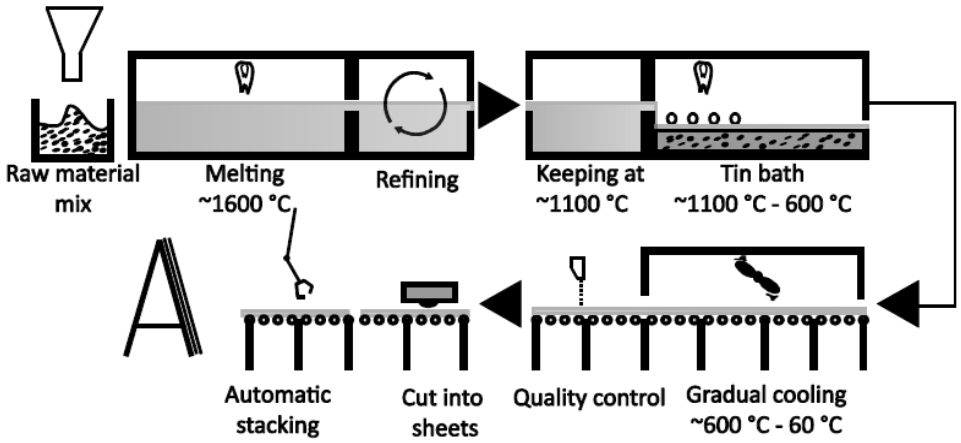

Figure 2.1 - A schematic diagram of the float glass manufacturing process (Achintha, 2016)

As the first step of the float glass manufacturing process, a batch is prepared by mixing the raw materials and it is heated to around 1600°C in a furnace to prepare molten glass. The ingredients are subjected to melting, refining, and homogenising at separate zones during this stage. The melting process acts as one of the key processes that can affect for the quality of the glass. Secondly, the glass from the furnace enters a tin bath. During this stage, glass is floated on a molten tin surface and the system is initially kept at about 1100°C. A flat glass ribbon having a uniform thickness and a smooth surface is produced by floating glass on this molten tin surface (Francis, 2016). This flat glass ribbon is kept at 600°C while leaving the tin bath. Thirdly, coatings can be applied to the glass ribbon to have the desired optical properties. Chemical vapour deposition is an advanced technology that is used for laying down the coatings. Fourthly, the glass ribbon moves through the annealing lehr, which is a special type of furnace used in the annealing process. The thickness of the glass ribbon can be controlled by adjusting the moving speed of the ribbon into the lehr (Achintha, 2016). The glass is subjected to gradual cooling at this stage and special heat treatment techniques are used to minimise the stresses which can be developed in the glass ribbons as they cool. Then, quality inspections are conducted to ensure the desired quality of the glass. It helps to identify the possible faults in the manufacturing process and the flaws in the glass material. After that, the glass ribbons are cut into sheets with the required sizes, and the final products are stacked in an orderly manner. Then, the glass is delivered to the customers. (Nascimento, 2014; Nippon Sheet Glass Co., Ltd., n.d.; Pilkington, 1969)

Float glass is subjected to the reheating and cooling process while producing both the heat-strengthened and fully tempered glass. Heat-strengthened glass is produced by uniformly heating annealed glass to 650°C – 700°C in an electrically heated furnace and cooling it down slowly at a slower rate. While cooling the system, the compressive stress of 24 – 69 MPa is developed on the glass surface. However, the central core is subjected to tensile stress. Heat-strengthened glass is two times stronger than float

glass. A similar process is used to make fully tempered glass except that the heated glass is subjected to rapid cooling. Fully tempered glass is usually four times stronger than float glass and has a surface compression higher than 69 MPa (AS 1288, 2021; Glass Academy, 2016).

2.2.2 The Laminated Glass (LG) Process

Laminated glass (LG) is manufactured by pasting a layer or multiple layers of plastic interlayer material in between two or more glass sheets and their arrangement is shown in Figure 2.2. Permanent mechanical and chemical bonds are there in between those layers. LG is used in practice as a special form of security and safety glass. Furthermore, it is used in cyclone and impact-resistant glazing, solar control glazing, sound proof glazing, blast-resistant glazing, insulated glazing, and automotive industries (Magic Glass, n.d.). During the manufacturing process, LG composites are subjected to high temperatures and pressures to make a tough seal removing air bubbles. It helps to strengthen the glass to resist stress. Even after failing the LG panel, the possibility of forming free-flying fragments is lower because of the ability of interlayer material to hold the failed glass fragments. Therefore, the risk and injuries due to free-flying shards can be minimised by using LG in the glass façades (Glass Academy, 2016; Jayaweera et al., 2022).

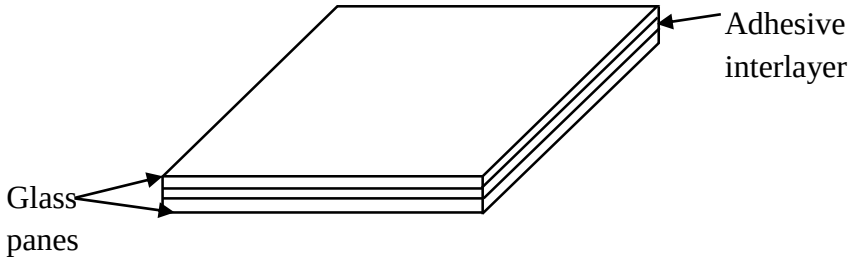

Figure 2.2 - Laminated glass unit

The flow chart given in Figure 2.3 shows the manufacturing process of LG. While producing LG, firstly, glass is selected and cut into the required shapes and sizes according to the approved drawings and clients' requirements. Proper inspections should be done to check the unevenness of the glass. If there is any unevenness in the glass, a complete bond cannot be made between the glass panes and the plastic interlayer films. Then, glass panes are transferred to the washing machines using roller tables to remove the dust, dirt, and oils on the glass surface. It helps to develop proper adhesive bonds between the interlayer films and the glass. After that, the glass sheets are cleaned and dried. Then, the laminating process is done in the clean room (see step 5 in Figure 2.3). The temperature and humidity inside this laminating room are controlled at 20 ± 3°C and 23 ± 3% respectively. At this stage, while stacking the glass panes, the stacking difference of each side should not exceed 1.5 mm. Furthermore, the interlayer film should be 5 mm larger than the glass pane (Qingdao Morn Building Materials Co. Ltd., 2019). Then, the sandwich unit is conveyed for pre-pressing (see step 6 in Figure 2.3). Pre-pressing is done to remove the air that has been trapped in

between the layers. The temperature and pressure should be properly controlled at this stage to maintain the expected quality of the pre-pressed glass without forming air bubbles. After that pre-pressed LG panels are transferred to the autoclave for final pressing and high temperature and pressure treatment. After completing the final pressing inside the autoclave, the temperature in the autoclave drops to 45°C. Then, LG panels are moved to the outside and the glass edges are trimmed (see step 7 in Figure 2.3). After that, the final products are packed and delivered to the customers (Glass Academy, 2016; Magic Glass, n.d.; Qingdao Morn Building Materials Co. Ltd., 2019).

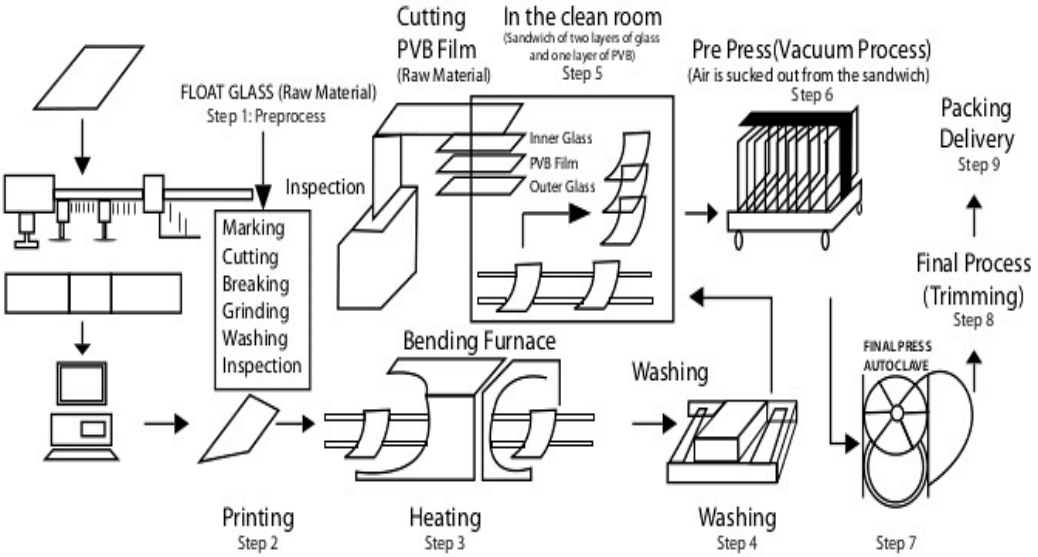

Figure 2.3 - Laminated glass production process (AIS Windshield Expert, 2014)

2.3 Windborne Debris Impact Phenomenon and Windborne Debris Hazards

As explained previously in Chapter 1, this research is focused on the windborne debris impact phenomenon. Therefore, it is worth having some basic understanding of windborne debris, geographic areas that are mostly affected by windborne debris, and the vulnerability of glass façades to their impacts. This section presents the details on the above topics.

2.3.1 Windborne Debris Impact Phenomenon

Previous windstorm investigations show that windborne debris is one of the most important sources which can cause severe damage to building envelopes during strong wind conditions (Minor, 2005; Minor & Mehta, 1979; Walker, 1991). Windborne debris can be generated from various types of sources such as building components, special items that are attached to the buildings, natural objects in the environment, etc. Shingles and tile pieces from roofs, timber rods from wooden frames, and free-flying shards from shattered windows and cladding sheets are some examples of windborne debris which can be generated from building components. Items attached to the

heating, ventilation, and air conditioning system of the building, signboards attached to the building envelope, and unbound construction materials such as small gravel particles on roofs, wooden chips, and demolished waste materials on rooftops of the buildings are some examples for special items which are attached to the buildings which can act as windborne debris during extreme wind events. Loose gravel particles on the open ground, tree branches, road furniture items, etc. are some examples of other sources of debris (Minor, 2005; Owen, 2015; Tamura, 2009). By conducting comprehensive investigations on tornadoes, Minor et al. identified the timber from failed timber structures as one of the common types of windborne debris in residential areas (Minor et al., 1993). A spherical steel ball of 8mm diameter and 2g mass and a 100 mm × 50 mm timber block of 4 kg mass are the commonly used missiles in most of the international standards such as AS/NZS 1170.2: 2011, ASTM E 1886 – 05, and ASTM E 1996 – 09 to represent the windborne debris. In 2012, Williams and Redgen identified the 100 mm × 50 mm timber blocks as the typical debris in cyclone-prone residential areas based on a comprehensive review which was conducted on the windborne debris impacts in Australia (Williams & Redgen, 2012). The research which is presented in this thesis is mainly focused on tall buildings in cyclone-prone residential areas. Therefore, the 100 mm × 50 mm wooden block of 4 kg mass was selected as the windborne debris in this study. Hence, it is important to understand the damage correlation which is associated with timber blocks. In 1992, Uematsu et al. explained this damage correlation in their study as it is explained below (Uematsu et al., 1992).

Strong wind flows can create comparatively high local suctions underneath the eaves. As a result of this scenario, the eaves can be damaged. Therefore, the vertical forces on the roof structures acting in the upward direction increase because of the sudden increase of the internal pressure inside the building. Consequently, the roof materials are uplifted and they travel away from their sources with comparatively high velocities. If the structural connections of the roof structure are not strong enough, the whole roof will be removed by the high-pressure forces. Then, these timber pieces and roof gravels will act as windborne debris causing successive damages to the buildings in the downwind direction which is generally known as the damage chain (Tamura, 2009; Uematsu et al., 1992). Figures 2.4 and 2.5 show the schematic diagrams for the damage correlation and damage chain respectively.

Several past research studies have been conducted on the trajectories of the different types of windborne debris. Wills et al. (2002) divided windborne debris geometrically into three main categories; Those are compact missiles, sheet-type missiles, and rod-type missiles. Roof and road gravel particles having spherical and cube shapes are some examples of compact missiles. Roof tiles, plywood boards, and shingles are sheet-type missiles. Tree branches, broken timber rods from timber structures, and bamboo poles are some examples of rod-type missiles (Wills et al., 2002).

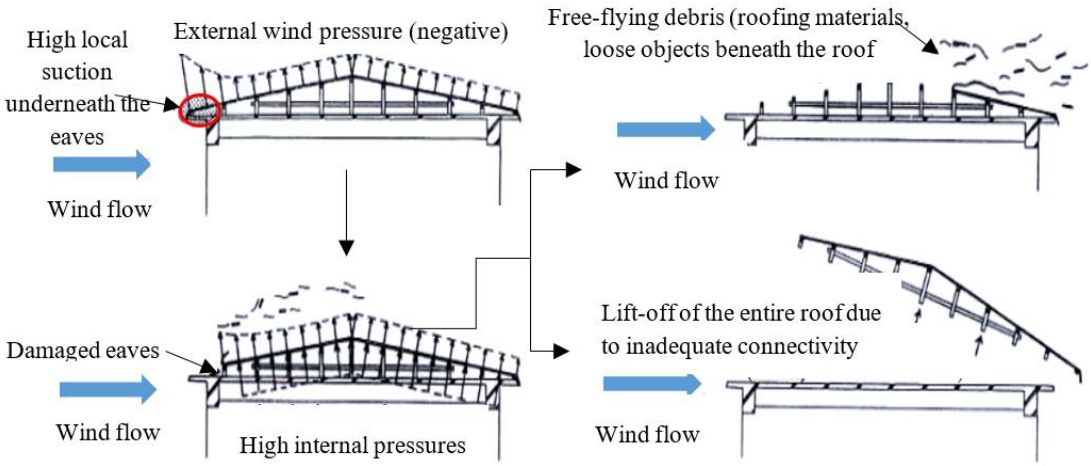

Figure 2.4 - Damage correlation (Uematsu et al., 1992)

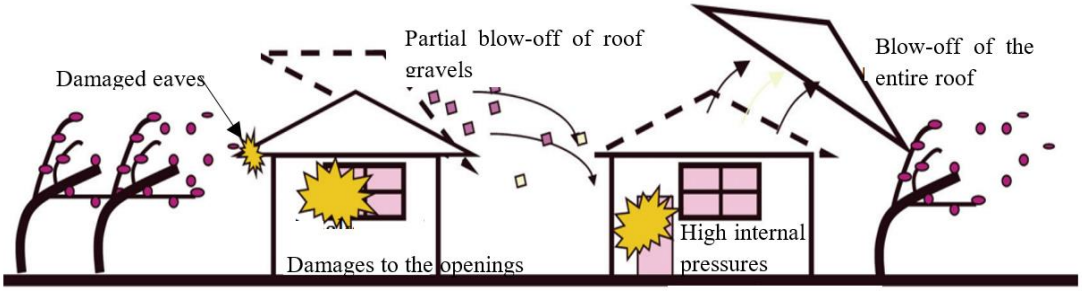

Figure 2.5 - Damage chain (Tamura, 2009)

Tachikawa (1983) presented an experimental program using wind tunnel simulations and derived empirical expressions for the drag, lift, and moment force coefficients of rotating plate-type objects in a uniform wind flow. Then, Tachikawa (1983) compared experimental results with the numerical results. Furthermore, he defined a dimensionless parameter (K) which gives the ratio of wind force to gravity force (Tachikawa, 1983). The parameter K is defined in Eq. 2.1.

$$K = \frac{\rho_a U^2 A}{2mg} \qquad \text{Eq. 2.1}$$

Where $\rho_a, U, A, m,$ and g denote air density, wind speed, reference debris area (area of the largest face), debris mass, and acceleration due to gravity respectively.

Lin et al. (2007) studied the horizontal trajectories of compact missiles and rod-type debris under a collaborative research study that was done at Texas Tech University and Louisiana State University in the United States of America. They did extensive experiments in wind tunnels at Texas Tech University under strong wind flows which were generated using C-130 aircraft. Since the present study is focused on the rod-type debris (i.e., 100 mm × 50 mm timber members of 4 kg mass), the characteristics of the horizontal trajectory of the rod-type debris are reviewed in this section. Lin et al. (2007) derived an empirical expression (see Eq. 2.2) for the dimensionless horizontal

velocity of the missiles ($\bar{u}$) considering the $\bar{u}$ versus $K\bar{x}$ curve (i.e., best-fit curve) which was plotted for the empirical data. $\bar{x}$ is the dimensionless horizontal distance. $\bar{u}$ and $\bar{x}$ are defined in Eq. 2.3 and Eq. 2.4 respectively (Lin et al., 2007).

$$\bar{u} \approx 1 - e^{-\sqrt{1.6K\bar{x}}}, \sigma = 0.0616 \quad \text{Eq. 2.2}$$

$$\bar{u} = \frac{u_m}{U} \quad \text{Eq. 2.3}$$

$$\bar{x} = \frac{gx}{U^2} \quad \text{Eq. 2.4}$$

Where u_m and x denote the horizontal velocity of the debris and horizontal displacement of the debris respectively.

By using Eq. 2.1 and Eq. 2.2, the ratio of the horizontal speed of the debris to wind speed can be rewritten in terms of the horizontal flight distance of the debris. Therefore, the velocity ratio above is a function of the horizontal flight distance of the debris (see Eq. 2.5 which has been developed for a 100 mm × 50 mm × 2400 mm, 4.1 kg timber block). However, this is not valid for the vertical component of the debris velocity (Lin et al., 2007).

$$\bar{u} \approx 1 - e^{-\sqrt{0.058\bar{x}}}, \sigma = 0.0616 \quad \text{Eq. 2.5}$$

Based on the horizontal velocity ratio, the horizontal impact speed of windborne debris can be estimated at a particular horizontal travel distance. Figure 2.6 compares the empirical and numerical trajectories of 100 mm × 50 mm timber rod of 4.1 kg mass. The numerical trajectories which are shown in Figure 2.6 are insensitive to wind speed (Lin et al., 2007). However, these curves have been developed considering a gust wind speed of 60 ms^{-1}.

According to ASTM Standards E 1886 – 05, for the representative large missile of 100 mm × 50 mm timber block, the specified impact speed is in the range of 0.10 to 0.55 of the 3s gust wind speed. Therefore, it is evident from Figure 2.6 that if designers use the specifications given in the Standard straightforwardly, there would be a possibility of underestimating or overestimating the actual impact speed of the missile, depending on its actual horizontal flight distance.

Figure 2.6 shows that the impact speed of the missile increases with the horizontal flight distance. However, if the missile lands on the ground surface early before reaching the target, it will not make any impact on that target. Hence, it is important to estimate the horizontal flight distance for the flight time of the missile. Wind flows create the driving force of the windborne debris. Therefore, the trajectories of the windborne debris are changed depending on the wind direction (Lin et al., 2007).

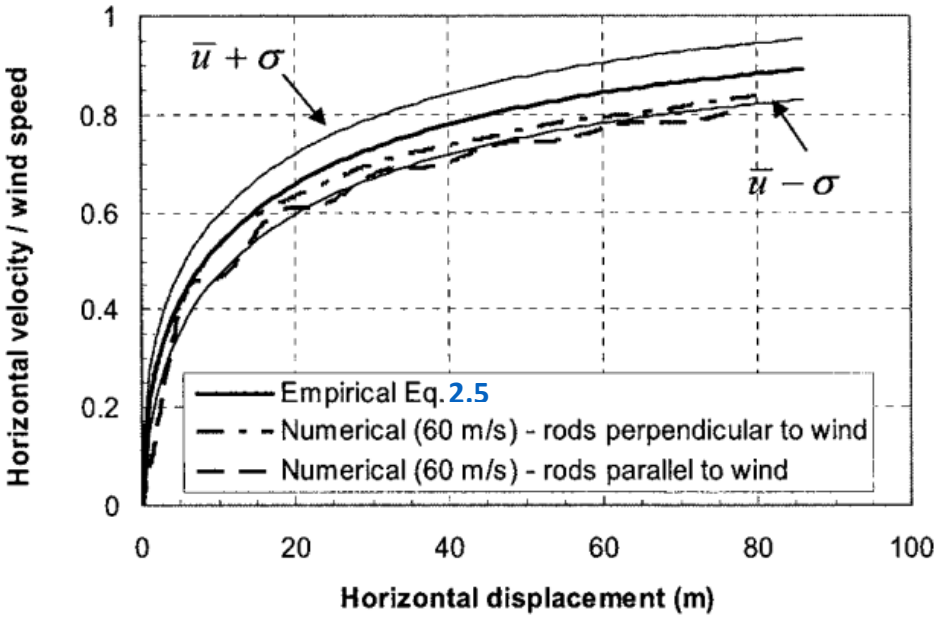

Figure 2.6 - Trajectory of a 100 mm × 50 mm × 2400 mm, 4.1 kg timber missile (Lin et al., 2007)

Lin et al. (2007) found that the numerical curves shown in Figure 2.6 are insensitive to wind speed. However, a gust wind speed of 60 ms^{-1} has been considered while developing the numerical curves in Figure 2.6. In addition, Lin et al. (2007) developed empirical expressions to estimate the horizontal flight distance of rod-type missiles. They developed two different expressions for the rods perpendicular to the wind flows (see Eq. 2.6) and for the rods parallel to the wind flows (see Eq. 2.7). Those expressions have been developed based on the empirical horizontal trajectories of rod-type debris which were plotted between $K\bar{x}$ and $K\bar{t}$ (where $\bar{x}$ and $\bar{t}$ are dimensionless horizontal distance and dimensionless time which is defined in Eq. 2.8). Figure 2.7 shows these horizontal trajectories.

Figure 2.7 shows that $K\bar{x}$ values of the rods parallel to the wind flows are lower than those values of the rods perpendicular to the wind flows. Lin (2005) found that the contribution of the vertical speed of plate-type and rod-type debris to the resultant speed is much smaller than that of compact debris. For the windborne debris that impacted buildings, the vertical component of the velocity is less significant than the horizontal component (Lin et al., 2007).

$$K\bar{x} \approx 0.4005(K\bar{t})^2 - 0.16(K\bar{t})^3 + 0.036(K\bar{t})^4 - 0.0032(K\bar{t})^5, \sigma = 0.0854 \qquad \text{Eq. 2.6}$$

$$K\bar{x} \approx 0.4005(K\bar{t})^2 - 0.294(K\bar{t})^3 + 0.088(K\bar{t})^4 - 0.0082(K\bar{t})^5, \sigma = 0.1492 \qquad \text{Eq. 2.7}$$

$$\bar{t} = \frac{gt}{U}; \text{t: time} \qquad \text{Eq. 2.8}$$

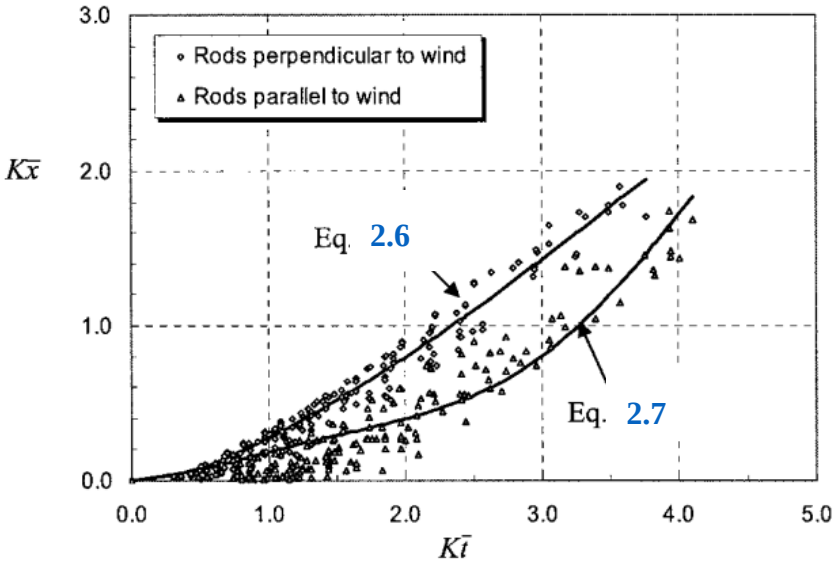

Figure 2.7 - Horizontal trajectories of rod-type missiles as $K\bar{x}$ versus $K\bar{t}$ (Lin et al., 2007)

These research findings provide justifications for specifying lower ratio for the vertical trajectories of timber members in international standards (i.e., A ratio of 0.1 of regional wind speed for the vertical trajectory of 100 mm × 50 mm, 4 kg timber member has been specified in AS/NZS 1170.2: 2011. However, for the spherical steel ball of 8 mm diameter and approximately 2g of mass, the ratio is 0.3 which is slightly higher than that of the timber member.).

2.3.2 Threats of Windborne Debris Impacts in Cyclone-Prone Regions

Cyclone-prone regions have been identified as the most affected geographic areas that have a higher risk of windborne debris impacts (Lee & Wills, 2002; Mejorin et al., 2019). Since the present study is focused on glass façades of tall buildings in cyclone-prone regions, this section presents an in-depth investigation of the cyclone-prone regions. Mejorin et al. (2019) identified the Asia-Pacific region as one of the most affected geographic areas by these cyclone events in terms of their frequency and intensity. Therefore, the Asia-Pacific region is selected in this study.

Heavy rains and extreme wind flows are produced by tropical cyclones which mainly arise over the ocean surface in tropical or subtropical regions. In the Northern Hemisphere, the spiral-shaped wind flows of cyclones blow in a counterclockwise direction. On the contrary, in the Southern Hemisphere, they blow in a clockwise direction. Generally, they spread over large water surfaces which are at relatively high temperatures. Cyclones may originate in different geographic areas. Therefore, based on the region in which they originate, cyclones can be named in different ways such as hurricanes, typhoons, etc. In the Southwest Pacific Ocean, they are called “Cyclones”. They are named “Hurricanes” when the origins are in the Caribbean Sea, Gulf of Mexico, Atlantic Ocean, and east of the International Date Line (IDL), and “Typhoons” when they are west of the IDL in the Pacific Ocean (Mejorin et al., 2019).

Figure 2.8 shows the regions which are affected by cyclones, hurricanes, and typhoons with their occurrence periods.

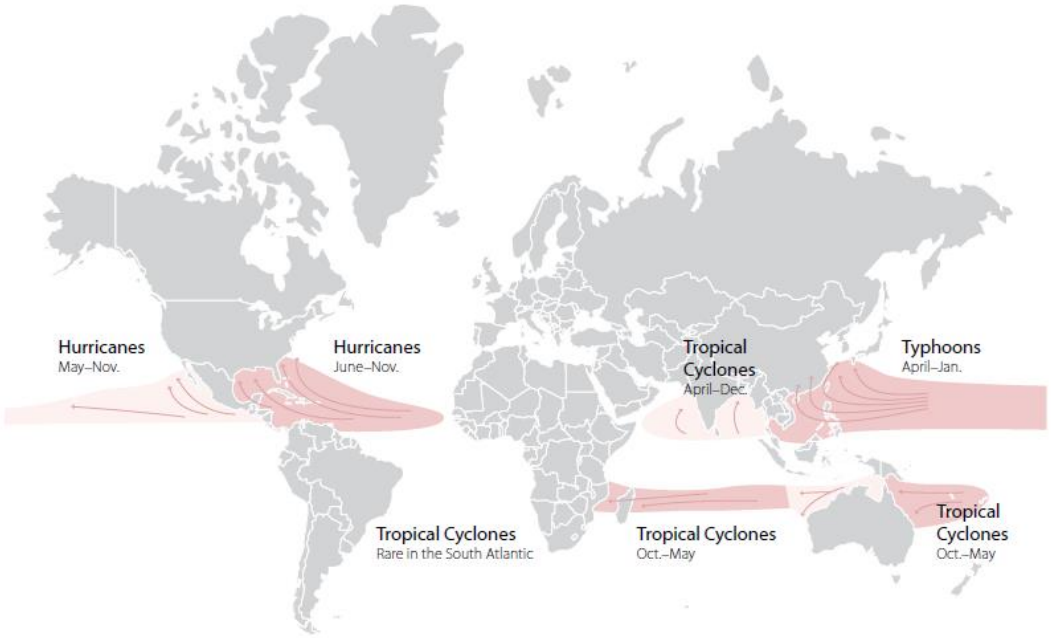

Figure 2.8 - Geographic regions affected by extreme wind events (Mejorin et al., 2019)

It should be noted that the economy and the population in the Asia-Pacific region increase with time (Mejorin et al., 2019). For example, from 1960 to 2017, the average increase in urban population in Australia, China, Hong Kong, Japan, the Philippines, and South Korea were 4.37%, 41.76%, 14.80%, 28.26%, 16.39%, and 53.79% respectively (Mejorin et al., 2019). With the growth of the urban population, the demand for tall buildings has increased in megacities to fulfil the requirements of new residential and office spaces. Most of these high-rise buildings have comparatively higher ratio of glass to surface area as well. It has been identified that urban growth has taken place in coastal areas which would lead to an increase in the possible risks and damages due to extreme wind events. Table 2.2 shows the average occurrences of typhoons in several selected countries in the Asia-Pacific region and compares the number of tall buildings in those regions based on the data available as of December 2017.

The total number of tall buildings as of December 2017 in the 12 cyclone-prone regions which are given in Table 2.2 has been identified as 7086. According to Table 2.2, more than half of those tall buildings (i.e., 4569 out of 7086) were situated in cyclone-prone regions. Before 2016 in the above regions, the total number of tall buildings, affected by typhoons, was 1778.

Table 2.2 - Occurrence of typhoons and number of tall buildings in typhoon-prone areas (Mejorin et al., 2019)

	No. of Typhoons as a proportion of disasters (Average annual no. of natural disasters, 2005-2014)	**No. of tall buildings affected by typhoons (Before 2016)**	**No. of existing tall buildings in typhoon-prone regions (As of December 2017)**	**No. of tall buildings in the construction stage in typhoon-prone regions (As of December 2017)**
Taiwan, China	81.3% (3)	78	102	12
Hong Kong, China	78.3% (1)	575	819	12
Japan	55.4% (6)	470	564	10
Bangladesh	52.8% (6)	1	5	4
South Korea	51.6% (2)	192	371	21
Philippines	51.3% (18)	74	144	47
Vietnam	48.7% (7)	9	102	57
Australia	43.5% (4)	68	170	27
China	33.2% (29)	300	1,675	387
New Zealand	32.3% (1)	5	10	0
Thailand	25.7% (4)	0	0	0
India	22.7% (16)	6	25	5
Total	**-**	**1,778**	**3,987**	**582**

However, the count of tall buildings in the same cyclone-prone regions was 3987 as of December 2017. It surpasses more than double the number of affected buildings prior to 2016. These buildings have experienced cyclone events periodically. Moreover, there were 582 buildings under construction. Depending on the intensity and frequency of the major wind events, the tall buildings in regions such as Thailand which were not initially affected by typhoons might be affected by them in the future.

That is because of the possible changes in the wind patterns which can occur due to new urban topology, rise in sea level with time, and enhanced greenhouse effects. Li and Stewart (2011) revealed that enhanced greenhouse effects lead to an increase in the intensity and frequency of tropical cyclones. As a result of this matter, the damages and risks associated with these cyclones will increase (Li & Stewart, 2011).

Therefore, it should be noted that these tropical cyclones are the main causes of windborne debris in the Asia-Pacific region. Because of the increasing threat of windborne debris impacts on glass façades in this area, it is important to adhere to the impact and cyclone-resistant glazing technologies while designing building envelopes.

2.3.3 Hazard Studies on Windborne Debris Impacts

The building envelope plays a dominant role in maintaining the performance and stability of the entire building during windstorms. Therefore, the building envelope also has a similar level of importance as it is there while designing the main structural frame of the building (Minor, 2005). Hence, façade engineers should concentrate on their designs in terms of cost-effectiveness, building performance, aesthetic appearance, occupants' safety, and stability of the building. As explained in Section 2.3.2, windborne debris impacts are one of the main threats to the glass façades in cyclone-prone regions. Therefore, it is important to learn lessons from past failures by conducting hazard studies on windborne debris impacts to develop impact-resistant glazing technologies and design strategies. Hence, this section presents some details on past windborne debris impacts and damages to the building envelopes that occurred due to three major windstorms; Cyclone Tracy (1974) in Darwin, Australia, Hurricane Andrew (1992) in South Florida, United States, and Typhoon Mangkhut (2018). Furthermore, this section highlights the lessons which can be learned from those failures and extreme wind events in terms of designing glass façades, so that the damages to the glass façades might be minimised during windstorms in the future.

Cyclone Tracy in Darwin, Australia (1974)

Tropical cyclone "Tracy" hit Darwin on 25th of December, 1974 in the early morning hours. It was developed as a result of the formation of a tropical low in the Arafura Sea about 700 km northeast of Darwin at 0930 Central Standard Time (CST) on 20th of December, 1974. The low-pressure region shifted slowly towards the southwest direction and gradually became a cyclone. The first warning alert about the development of this cyclone was issued at 1600 CST on 21st of December. However, the first official warning was issued at 2200 CST on that day and it was named "Tracy". By 1530 CST on 22nd of December, the eye of 37 km diameter was clearly observed by the radar images and it was roughly 200 km North of Darwin at that time. During the period of 0000 CST to 0100 CST on 25th of December, the recorded gust wind speed in Darwin exceeded 100 kmh^{-1}. After 0100 CST, the Bureau's Tropical Cyclone Warning Centre received several reports on severe damages that occurred in Darwin. At 0305 CST, a peak gust wind speed of 217 kmh^{-1} was recorded in the Darwin airport. At 0350 CST, the eye passed the Darwin airport. The cyclone was becoming weak

after 1100 CST on the 25th and it moved in the southeast direction across southern Arnhem Land into Western Queensland (Department of Science, Bureau of Meteorology, 1977).

71 deaths and 650 injuries were reported due to this cyclone. In the early 1970s, there were approximately 8,000 houses and 3,000 flats in Darwin (Mason & Haynes, 2010). Walker (1975) conducted a preliminary survey after the cyclone to find out the damage statistics. He selected 6,981 houses for his survey and found that 3,675 (i.e., 53%) houses were destroyed. 1,168 (i.e., 16%) of them were with repairable roof and wall damages. He reported that 10% of flats were destroyed and 40% of them had repairable damages to the roof, walls, and top floor. However, damages to the engineered buildings were comparatively lower than the damages to the houses and flats. Past investigations show that 20% of engineered structures were completely destroyed by Tracy. But, for the houses, it was as high as 53% (Mason & Haynes, 2010; Walker, 1975). Walker (1975) considered three key factors while conducting the investigations on damage patterns of the buildings in Darwin. Those are the wind field of the cyclone, the topography of the area, and the strength of the building (Walker, 1975). According to the wind field data, the basic wind speeds in all areas of Darwin were high during the cyclone. The duration of extreme wind flows also played a significant role in causing severe damage to the buildings. The damages to the buildings in exposed areas such as coastal lines, top of the slopes facing the sea, and open lands were comparatively high (Walker, 1975). The resistance to the wind flows which is produced by water bodies is significantly low. Therefore, the buildings that were facing the sea had been severely affected by the high-velocity winds. In addition, vegetation and neighbouring buildings can reduce the wind speed by increasing the roughness of the earth surface. It is interesting to note that although there were buildings subjected to approximately the same wind speeds, different damage levels could be identified depending on the strength of the buildings. Therefore, severe damages could be seen in weaker buildings than those in stronger buildings (Walker, 1975).

In the 1970s, asbestos-fibrous cement sheets and bricks were the commonly used wall cladding materials in residential houses. But ribbed metal and corrugated iron claddings could be seen in larger buildings (Mason & Haynes, 2010). The residential houses with asbestos fibrous cement wall claddings were severely affected by windborne debris giving rise to extensive damages. Although asbestos cement sheets have some capacity to resist in-plane shear, their performance is very poor under impact loads. Figure 2.9 shows the debris which was carried by the strong wind flows during the cyclone. The debris was lifted and driven by the high-velocity winds causing severe damages to the roof claddings, wall claddings, windows, doors, etc. Hence, they were found to behave as windborne debris during the cyclone. Figure 2.10 shows the damaged wall cladding of a house due to windborne debris impacts. The asbestos fibrous cement sheets had been used in the wall cladding shown in Figure 2.10.

Figure 2.9 - The debris in Darwin after the Cyclone Tracy (Walker, 1975)

Figure 2.10 - The damaged wall cladding (Walker, 1975)

Past investigations show that non-structural veneers that had been constructed using brick masonry and concrete blocks were also damaged due to windborne debris impacts because of their inability to resist the sudden impacts (Mason & Haynes, 2010). The damages to the ribbed metal and corrugated iron claddings were comparatively lower because of their ability to deform plastically under the sudden impacts. Figure 2.11 shows a well-performed metal cladding during the cyclone.

According to post-disaster investigations, mainly, there were two predominant cases of window failures. One of those was a failure of windows due to flying debris impacts. The second case was blowing out of the entire frame of the window from its original position due to wind pressure. By studying the damage pattern of the windows which were subjected to debris impacts, it was found that impact-resistant glass panels were not used in those windows. However, most of the windows that had been protected by using sunshades or additional protective layers did not fail due to windborne debris impacts. The most prominent reason for the second case was inadequate connectivity between the window frames and the main structure. Figure 2.12 shows the survival of a window protected by sunscreens during the windborne debris impact of Cyclone Tracy.

Figure 2.11 - Survived metal cladding of a house (Walker, 1975)

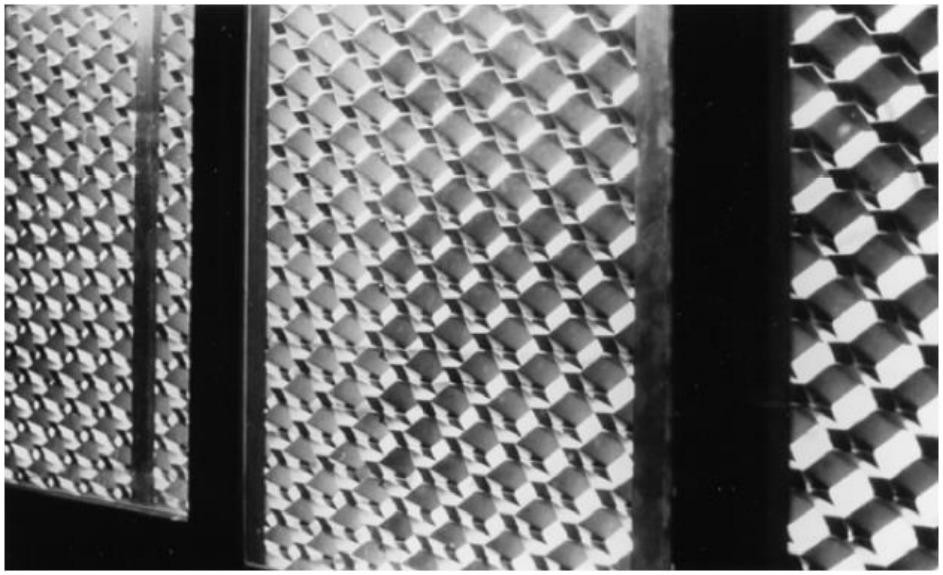

Figure 2.12 - Survival of a window with sunscreen (Walker, 1975)

It is important to highlight the lessons that can be learned from cyclone Tracy in terms of windborne debris impacts on building envelopes. The key lessons are explained

here. When windward walls or windows are damaged by flying debris during a heavy wind event, additional loads are applied to the structure as a result of the internal pressurization. This phenomenon was identified as one of the main reasons for the severe damages that were reported during the cyclone. Therefore, it was suggested to consider internal pressurization while designing the houses (Walker, 2010). This aspect was not significantly considered before cyclone Tracy. Moreover, the significance of providing adequate connections between the window frames, door frames, and the main structure was identified. It was found that some connections could not perform better even under high wind pressures. Therefore, those connections should be designed such that they can effectively transfer the loads that are produced on the window and door frames due to wind pressure and sudden impacts. In addition, builders also have to follow the specified design requirements while doing their construction. Furthermore, damages to the main structure of a building because of the internal pressurization and risk of occurring injuries and damage to the properties due to free-flying glass fragments which were generated by sudden debris impacts were found to be the most significant threats due to windborne debris impacts.

Hurricane Andrew in South Florida, United States (1992)

According to the evidence given by the satellite images, Hurricane Andrew was formed by a tropical wave on 14th of August, 1992. Around 1800 Coordinated Universal Time (UTC) on 16th of August, that tropical wave transformed into a tropical depression. By 1200 UTC on 17th of August, that depression became stronger and developed into Andrew. By 22nd of August, the strength of Andrew attained the strength of a hurricane. At 1800 UTC on 23rd of August, the windstorm reached Category 5 of the Saffir-Simpson hurricane scale by attaining its 1-minute maximum sustained wind speed of 280 kmh^{-1} (Landsea et al., 2004). At 2100 UTC on the same day, Andrew hit Eleuthera with a wind speed of 260 kmh^{-1}. While moving over the Bahama Banks, the hurricane became weaker to some extent. It made landfall on the Southern Berry Islands at 0100 UTC on 24th of August having a Saffir-Simpson hurricane scale of Category 4 and a wind speed of 240 kmh^{-1} (Landsea et al. 2004). While crossing the warm water body of the Gulf Stream, the hurricane became stronger again (Rappaport, 1993). On the 24th, Andrew reached Florida. It hit the Gulf of Mexico after moving over South Florida. On the 26th, the hurricane emerged into Louisiana around 0830 UTC with a wind speed of 185 kmh^{-1}. After that, the hurricane weakened with time.

Bahamas, Florida, and Louisiana were severely devastated by Andrew. Approximately, 177,000 people became homeless because of the damages which were caused to more than 63,500 residential structures by the windstorm. 65 fatalities were reported and the cost of the damage was US $ 27.3 billion (i.e.; US $ 53 billion in 2021) (Rappaport, 1993; National Hurricane Centre, 2018). Behr and Minor (1994) highlighted that damages to the glazing systems due to windborne debris impacts were a common threat during the hurricane (Behr & Minor, 1994). The windward wall (east wall) of the American Bankers Insurance Group building, Cutler Ridge was damaged by the windborne debris that was generated by Andrew (see Figure 2.13). By observing

the broken glass pieces of the glass panels Behr and Minor (1994) reported that 6 mm thick annealed or heat-strengthened glass had been used in the spandrel glass. They found that 6 mm thick fully tempered monolithic glass had been used in the vision glass and structural silicone sealant was used along the supporting frame of the glass panel (Behr & Minor, 1994). Roof gravels and segments of failed roof structures were identified as the common debris types that made severe impacts on that building.

Figure 2.13 - Extensively damaged glass panels of the American Bankers Insurance Group Building, Cutler Ridge, Florida (Behr & Minor, 1994)

In addition, the glass window panels of Datran Tower One in Kendall, Florida were severely damaged by the windborne debris generated from the gravel ballast layer on the roof of the Marriott Hotel (Behr & Minor, 1994). After conducting a comprehensive survey on the response of glass façades to Hurricane Andrew, Behr and Minor (1994) highlighted that building envelopes should be designed and constructed as structural elements. In addition, they have emphasised the importance of having a proper anchorage system in between the façade elements, wall cladding, and the main structural elements of the buildings to resist extreme loadings such as windborne debris impacts.

Super Typhoon Mangkhut, Hong Kong (2018)

Mangkhut originated in the western North Pacific region approximately 2,330 km east of Guam on 7th of September, 2018, and hit Hong Kong on 16th of September (see Figure 2.14). The maximum gust wind speed and maximum hourly mean wind speed recorded on 16th of September at Hong Kong International Airport were 157 kmh^{-1} and 99 kmh^{-1} respectively (Hong Kong Observatory, 2020). However, the maximum

hourly mean wind speeds recorded at Waglan Island and Cheung Chau were as high as 158 kmh^{-1} and 151 kmh^{-1} respectively (Hong Kong Observatory, 2020).

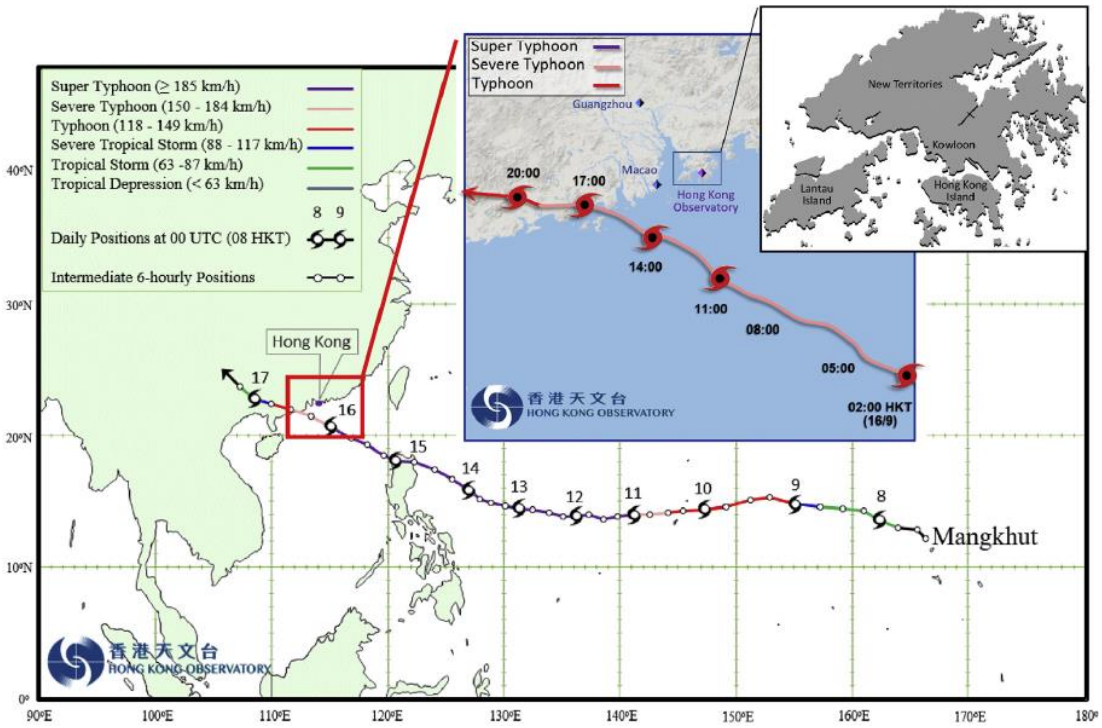

Figure 2.14 - The path of Mangkhut from 7th to 17th of September, 2018 (Choy et al., 2020; Hong Kong Observatory, 2020)

It was found that approximately 500 cases of failed and broken windows had been reported due to Typhoon Mangkhut (Legislative Council, 2018). For example, damages to the windows of high-rise buildings in Hong Kong are shown in Figure 2.15.

Peng and Li (2019) have highlighted three different mechanisms that can lead to the failure of glass window panels during an extreme wind event. Those three mechanisms are the high wind pressures on glass panels which can go beyond the design pressure values, windborne debris impacts, and the performance of glass under dynamic wind loads. However, after examining these three mechanisms, they identified the windborne debris impact phenomenon as the primary cause of window damage during Typhoon Mangkhut (Peng & Li, 2019). Figure 2.15 (a) shows the severe damage to glass window panels of the Two Harbourfront Office Tower in Hong Kong. It shows a comparatively higher number of damaged glass panels at lower floor levels of the building. Generally, wind pressures are high at upper floor levels of the building due to the wind profile. Therefore, most of the glass panels at the upper floor levels were damaged by the high wind pressures forming glass fragments. Those glass fragments had also caused some successive damages to the window panels at lower floor levels of the building in addition to the windborne debris originating from external sources. Figures 2.15 (b) and 2.15 (c) showcase the damages to glass window panels of Hang Seng Bank Headquarters Building and Immigration Tower in Wan Chai respectively.

(a) Two Harbourfront Office Tower, Hong Kong (Wikimedia, 2018)

(b) Hang Seng Bank Headquarters Building (Wikimedia, 2018)

(c) Immigration Tower, Wan Chai (Wikimedia, 2018)

Figure 2.15 - Damaged glass panels of buildings in Hong Kong due to windborne debris impacts during Typhoon Mangkhut 2018

Therefore, based upon the pieces of evidence discussed above in this section, it is true that windborne debris impacts are not only capable of causing severe property damage but also can cause some severe injuries and health risks. Hence, it is worthwhile to design and construct cyclone-resistant façade systems adopting the lessons learned from past failures.

2.4 Design Standards and Standard Testing Methods

This section discusses the first steps to introduce the windborne debris impact criteria and cyclone-resistant glazing in the design standards, and the standard testing methods and guidelines that have been considered in the present study. Furthermore, the limitations of the available design standards and standard testing methods are highlighted at the end of this section.

Before Cyclone Tracy, Standard Association of Australia (SAA) Interim 350 (up to 1971) and Australian Standard (AS) CA 34.2 (from 1971 to 1973) were used as the wind codes in Australia (Holmes et al., 2012). In 1973, the AS CA 34.2 wind loading code was republished as AS 1170.2: 1973 Edition by converting it to metric units. Subsequently, several revisions were made to AS 1170.2 over the years. After Cyclone Tracy, the Darwin Area Building Manual was developed in 1976 by introducing debris impact criteria to the building codes. That was the first step in introducing debris impact criteria in building codes anywhere in the world (Minor, 2005). In 1978, "Technical Record 440 (TR 440): Guidelines for the Testing and Evaluation of Products for Cyclone-Prone Areas" was published to showcase the technical decisions that were taken during a workshop that was held in July 1977 at the Experimental Building Station of the Department of Housing and Construction, New South Wales, Australia. The recommendations for loading criteria, testing methods, and assessing the performance of window panels, roof claddings, and wall claddings were highlighted in TR 440 (Experimental Building Station, 1978). Furthermore, the American Society of Civil Engineers (ASCE) standard; ASCE 7 (ASCE, 2022) also provides guidelines for wind loading and impact-resistant covering. The standard testing methods and performance criteria have been specified in the ASTM standards as well for designing cyclone-resistant building envelopes. ASTM E 1996 outlines the criteria for evaluating the performance of building envelopes to design hurricane-resistant impact protective exteriors of buildings and ASTM E 1886 specifies the standard test methods for building exterior elements.

AS/NZS 1170.2: 2011, ASTM E 1886-05, and ASTM E 1996-09 codes of standard were used in the present study. The two representative missiles: a timber block of 4 kg mass, of a nominal cross-section of 100 mm × 50 mm and a density of at least 600 kgm^{-3}; and a spherical steel ball that has a diameter of 8 mm and approximately 2 g mass have been specified in AS/NZS 1170.2: 2011 for windborne debris impact loading. Furthermore, it suggests $0.4V_R$ and $0.1V_R$ speed (where V_R is the regional wind speed) for the horizontal and vertical trajectories of the timber test member respectively. For the spherical steel ball, the specified values are $0.4V_R$ and $0.3V_R$ for

the horizontal and vertical components of the impact speed respectively. However, this code of standards does not outline a test procedure or an evaluation criterion for the windborne debris impact phenomenon. ASTM E 1886-05 outlines the specific methods for mounting the specimen, impacting the specimen with a representative missile(s), applying the cyclic pressure loads on the test specimen, observing and taking the measurements of the specimen, and interpreting the results. It has suggested three missile propulsion devices: (i) Large missile air canon; (ii) Bungee test apparatus; and (iii) Small missile air canon. ASTM E 1996-09 provides some set of guidelines to conduct the impact tests which are given in ASTM E 1886-05 and criteria for evaluating the performance of building envelopes.

The impact location can be considered as one of the important aspects of impact-resistant testing methods because the level of firmness and flexibility of the window panels will vary based on the impact locations of the panel where the debris hit (Williams & Redgen, 2012). Therefore, different technical reports and standards have specified different impact locations on a window panel to consider while carrying out the impact tests on window panels. However, the specified impact locations may vary depending on the standard or technical report. TR 440 mandates to use of timber missiles and suggests two impact locations: one within 300 mm of the geometric centre of the panel, and the next within 300 mm of the supporting frame. In addition, it suggests to conduct the tests on two different specimens. However, if the user prefers, one specimen can be used as it is mentioned in TR 440. Therefore, TR 440 assumes that the likelihood of two impacts occurring on one single specimen is low. However, Williams and Redgen emphasised that the tolerance level of 300 mm for centre impacts and edge impacts is comparatively large (Williams & Redgen, 2012). The document named "Design Guidelines for Queensland Public Cyclone Shelters" also outlines some specifications for the timber test members. Most of these guidelines are quite similar to the guidelines specified in TR 440. However, it shows some flexibility while specifying the impact locations. For example, it allows the testing authority to decide the most critical impact locations (Williams & Redgen, 2012). Furthermore, it recommends considering two impact locations; centre of the panel, and the location closer to the supporting frame which corresponds to the impact location specified in TR 440. But it does not specify any tolerances. (Department of Public Works, 2006). It should be noted that because of the flexibility given in these cyclone shelter guidelines, the manufacturers and testing authorities may only consider some random locations that are not the critical impact locations of the window panel.

In 2017, the Cyclone Testing Station (CTS) at the James Cook University in Australia published a document named "Simulated Windborne Debris Impact Testing of Building Envelope Components – Technical Note No.04" (CTS, 2017). It specifies different impact locations to carry out the impact tests on window panels. However, the tolerance levels have not been defined in these guidelines. CTS Technical Note No.04 recommends performing impact tests at the geometric centre of the panel, interface corner, and interface edge of the panel. Additionally, it suggests performing impact tests at the centre of the mullions, and the base of the mullions as well as if the

window panel has interior mullions. The Viridian Glass specifies impact locations with a more practical tolerance range. It suggests that the timber missiles are to be impacted at the geometric centre of the panel, centre of the edge, and at the corner. For the impacts at the centre of the edge and corner, the impact locations should be at 100 mm distance from the relevant fixing edges (Viridian Glass, 2011).

ASTM E 1996-09 suggests different impact locations where the missiles should be impacted. It specifies different impact locations for small missiles and large missiles separately. Since the present study is mainly focused on large missile impacts, the impact locations that have been specified for the large missiles are discussed in this thesis. Figure 2.16 shows the specified impact locations for the large missiles. In Figure 2.16, the white circle and the black circle represent the first impact and the second impact respectively. As shown in Figure 2.16, the code suggests making a single impact on the specimen either at the centre or at the corner for the wind zones 1, 2, and 3 which have been categorized in ASTM E 1996-09. However, the specimens should be subjected to two impacts for wind zone 4 where the basic wind speed is greater than 63 ms^{-1}.

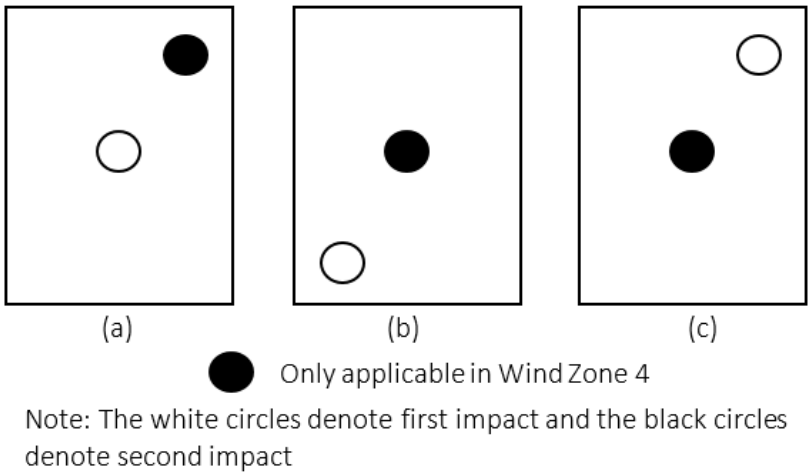

Figure 2.16 - Impact locations in ASTM standards for large missile test (ASTM E 1996-09)

As it has been specified in ASTM E 1996-09, the centre of the missile must be within a 65 mm radius of the circles which are shown in Figure 2.16. The centre of the circles that are shown in the middle of the specimens coincides with the geometric centre of the specimen (ASTM E 1996-09). In addition, For the impacts at corners, the centre of the circle must be 150 mm away from the supporting members. A comprehensive review was conducted by Williams and Redgen in 2012 on the debris test methods and evaluation criteria for impact-resistant glass façades. Based on that study, they have proposed different impact locations for large missiles and small missiles separately (Williams & Redgen, 2012). The impact locations that have been proposed for the large missiles are shown in Figure 2.17.

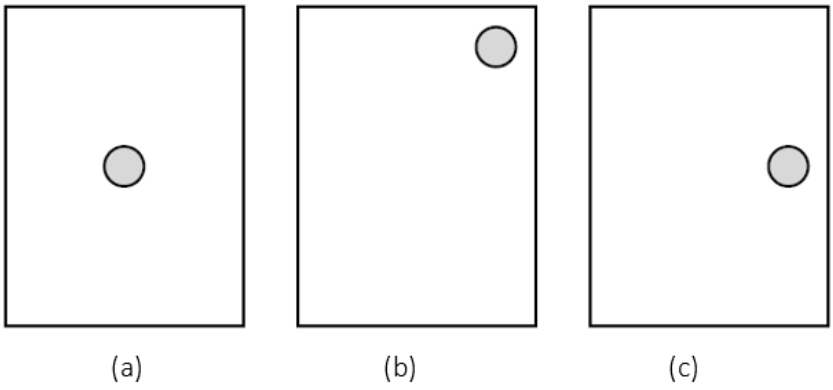

Figure 2.17 - Impact locations for large missile test (Williams & Redgen, 2012)

However, it is worth highlighting the major limitations of the design standards and standard testing methods. The higher cost associated with the standard testing methods is one of the major limitations. In particular, the cost of glass panels is comparatively high. Therefore, project authorities have to incur considerable costs for purchasing glass specimens to conduct standard tests before using these glass panels in their actual projects. In addition, university funding agencies and other government agencies are also facing some difficulties in purchasing glass specimens and conducting extensive laboratory experiments in their research studies because of the higher cost involved with the standard testing methods. Furthermore, the risk involved with the laboratory experiments on glass panels is also high at higher impact velocities. Therefore, special precautions should be carried out for health and safety before conducting these experiments.

2.5 Impact- and Cyclone-Resistant Glazing Technologies

One of the major threats of strong wind events is the potential damage to the glass façades due to windborne debris impacts. There are several consequences of failing window panels and glass façades: injuries due to free-flying glass fragments; internal pressurisation; detachment of the roof structures; and rainwater penetration. Consequently, the durability of the structures will also be severely affected. Therefore, it is worth reviewing the modern impact- and cyclone-resistant glazing technologies. This section includes these state-of-the-art technologies adopted in current practice.

Window shuttering systems are used as one of the alternative solutions for windborne debris impact-resistant glazing (Mejorin et al., 2019). There are different types of shutters available in the market such as roll-down, accordion, storm panels, perforated barrier, colonial, and plywood shutters. These shutters can provide protection for window systems against strong wind conditions and flying debris impacts. However, they can affect the appearance of the buildings and some shutters can also disrupt the view from the inside of the building. The engineers and architects therefore consider these aspects when they select an appropriate shuttering system.

In addition, window frame design and installation of glass in the window frame are the two important aspects of impact-resistant glazing (Mejorin et al., 2019). The window framing system is usually designed such that the glass panels are to be held properly on the window frame without throwing it away from the supporting frame under high wind pressures and sudden impact loads. Usually, the glass bite is designed to be deeper to facilitate the façade system to behave as a unit protecting the building interiors from possible environmental threats. If the façade system is designed to resist the debris impact, the entire system should be designed to perform well during strong wind conditions. Therefore, it is important to select a suitable glazing material considering the possible impact loads and wind loads that the window panels will experience.

Currently, polycarbonate is widely used in bulletproof glazing applications. However, it is comparatively harder and more expensive than LG (Hidallana-Gamage, 2015). Figure 2.18 (a) shows a polycarbonate specimen that has been tested for its bullet-resistant behaviour. It has been found that LG also provides good protection against windborne debris impact (Zhang et al., 2013; Zhang et al., 2014). Therefore, LG has been identified as a very popular safety glass material among designers and architects because of its safety features, cost advantages, and unique aesthetic appearance. Figure 2.18 (b) shows a closer view of the edge of an LG panel. LG is a flexible material compared to polycarbonate. Therefore, LG panels can absorb a significant amount of impact energy and transfer relatively reduced forces to the supporting structure of the window frame. This research study is therefore mainly focused on the impact behaviour of LG under windborne debris impact.

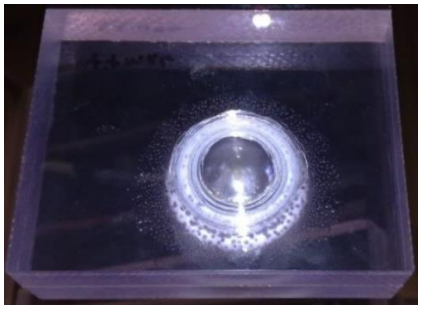

(a) Polycarbonate specimen (Hidallana-Gamage, 2015)

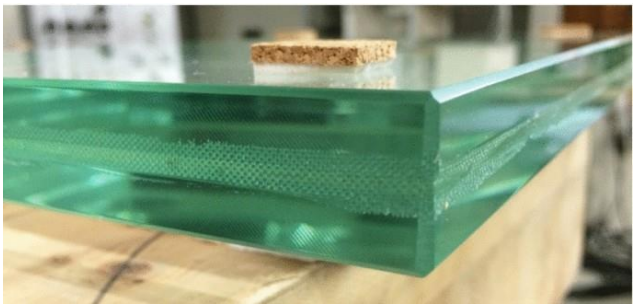

(b) LG panel (Silvestru et al., 2019)

Figure 2.18 - Safety glass materials

The case studies presented in Section 2.6 showcase further insights into the impact-resistant façade technologies used in current practice.

2.6 Case Studies on Impact-Resistant Façade Technologies

The details of the case studies conducted on the selected glass façades located in cyclone-prone areas are presented in this section. These case studies were conducted to identify the design requirements, codes and guidelines, design phase considerations, and design principles associated with impact-resistant glazing technologies. The Integrated Marine Operations Centre (IMOC), Port Hedland, Australia, and the Australian Institute of Tropical Health and Medicine (AITHM), Townsville, Australia are the two structures reviewed in this section.

2.6.1 Integrated Marine Operations Centre (IMOC), Port Hedland, Australia

Integrated Marine Operations Centre (IMOC) is situated in Port Hedland, Australia. It was constructed by replacing the previous control tower in this area and the constructions were completed in 2018. The project details are summarised below (Mejorin et al., 2019).

- Developer - Pilbara Ports Authority
- Architect and Structural Engineer - Pindan Group
- Façade Consultant - Inhabit Group
- Façade Contractor - JML-Craft

IMOC has a control tower and a two-storey podium and it is shown in Figure 2.19. The western elevation of the structure is shown in Figure 2.20. A perforated screen (see Figure 2.19) has been constructed around the podium covering the majority of the podium. The glass curtain wall is behind the perforated screen with a 1 m offset. At Level 5 of the tower, there is a full-height glass curtain wall system (see Figure 2.20). In addition, an inclined glazing system with a slope of 67.5° has been used at Level 6 (see Figure 2.20).

Figure 2.19 - Integrated Marine Operations Centre (IMOC), Port Hedland, Australia (Inhabit Group, n.d.)

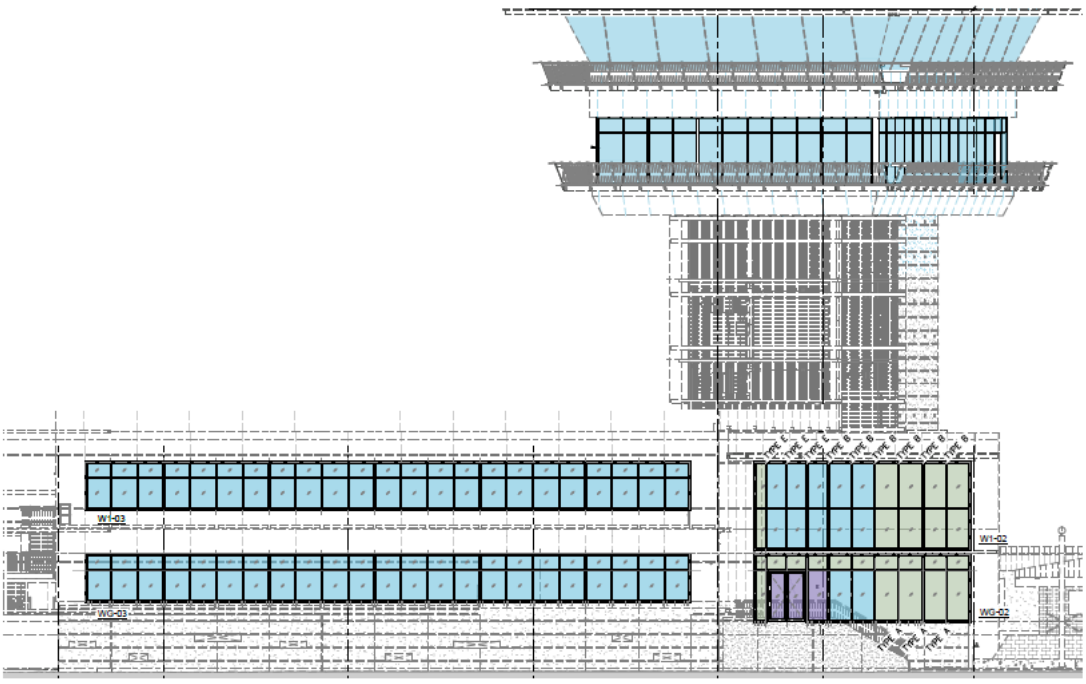

Figure 2.20 - Glass façade system of the Integrated Marine Operations Centre – Western Elevation (Mejorin et al., 2019)

The design team has used AS/NZS 1170.1: 2002, AS/NZS 1170.2: 2011, AS 1288 – 2006, AS/NZS 1644.1, AS 4100 – 1998, and Technical Note No.04 – Simulated Windborne Debris Impact Testing of Building Envelope Components as standard specifications and guidelines for designing this building. During this project, a podium-level façade system has been considered for impact-resistant glazing. However, the impact resistance of the outer perforated screens has not been considered. Since AS/NZS 1170.2:2011 provides limited specifications regarding the testing procedure, designers have followed the testing procedure specified by the CTS at the James Cook University in Technical Note No.04. For the project site, $0.4V_R$ (V_R is the regional wind speed) is approximately 39.6 ms^{-1}. Although cyclic loading is considered in American testing requirements, it is not considered in Australian Standards. Hence, cyclic loading has not been considered while designing a façade system for IMOC (Mejorin et al., 2019). Design pressure has been calculated considering the 3-second gust wind speed of a 2000-year return period. The load factor has been taken as 0.35 for serviceability wind loads. The IMOC has been designed as a structure with importance level 4 with post-disaster functionality.

The façade support system of the podium consists of an aluminium captive system. Steel stiffeners have been used in mullions at the podium level. While selecting the glass material, façade designers focused their attention on both the wind pressure loads and the sudden impact loads. Typical LG panels composed of 6 mm heat-strengthened glass, 6.08 mm PVB, and 12 mm argon-filled air gap have been used in the façade glazing at the podium level. The arrangement of typical LG panels is as follows.

Heat-strengthened glass (6 mm) + PVB (6.08 mm) + Heat-strengthened glass (6 mm) + Argon-filled air gap (12 mm) + Heat-strengthened glass (6 mm)

The purpose of having an argon-filled air gap is to provide the required thermal comfort to the building. The glass window panels were tested at the Azuma Lab following the standard specifications given in the Australian Standards. Figure 2.21 shows a tested glass panel that was impacted by a standard timber missile at 40 ms^{-1} impact speed. In addition, a standard steel ball bearing test was also conducted on windows panels. After conducting standard tests, engineers identified that the selected typical window panel satisfied the impact-resisting requirements, and neither the standard timber missile nor steel balls penetrated the glass panel (Mejorin et al., 2019). Furthermore, as it was suggested by the experts, an additional impact test was conducted by impacting the timber missile at the corner of the panel. It was observed that the glass panel deformed out of the window frame and failed. Although the cyclic loading phenomenon was not tested during this testing procedure, it can also lead to tearing the glass panes from the sealant joints due to the possible movements in the outward and inward directions. However, the tested panels satisfied the minimum required performance for the podium façade system. For cyclone testing, the fracture of the inner glass pane was not considered as a failure.

Figure 2.21 - Tested window panel (Mejorin et al., 2019)

The control tower of the IMOC has glass façade systems at Level 5 (Incident control room) and Level 6 (Vessel traffic service room). Level 5 façade system has mullions with steel stiffeners. Level 5 façade consists of an aluminium captive glass façade system which is similar to the podium façade. As described previously, an inclined façade system has been used for the Level 6 façade. The arrangement of the Level 6 glass façade panel is as follows.

Toughened glass (15 mm) + SentryGlas® (SG5000) interlayer (2.28 mm) + Toughened glass (15 mm) + SG5000 (2.28 mm) + Toughened glass (15 mm) + Argon-filled air gap (12 mm) + Monolithic heat-strengthened (10 mm)

However, the design team confirmed that windborne debris impact testing is not required for the Level 6 façade system.

After conducting standard testing methods, the designers of the IMOC concluded that the selected LG material had passed the design requirements. The pass/ fail criterion was identified by inspecting the penetration status of the panel and comparing the aperture size with 5000 mm^2. In addition, they identified that there will be a possibility of disengaging of glass edge from the window panel, especially under the impacts hit the corner of the panel if the connection between the panel and frame is insufficient. Furthermore, they concluded that the inner glass pane will shatter under sudden impacts regardless of whether the heat-treated glass is used or not.

2.6.2 Australian Institute of Tropical Health and Medicine (AITHM), Townsville, Australia

The Australian Institute of Tropical Health and Medicine (AITHM) is a health and medicine research institute located at the James Cook University's Douglas Campus in Townsville, Australia. It houses certified laboratories, a biobank, offices, and meeting rooms. The project details of the AITHM are as follows (Mejorin et al., 2019).

- Architect – Jackson Architecture
- Structural Engineer – Opus Group
- Façade Contractor – G.James Glass & Aluminium

The north and south elevations of the building consist of horizontal strip glass windows and metal wall claddings. Punched windows have been used to the west and east elevations of the building. A proper solar control system with sunshade screens and sunshade hoods has been designed to minimise solar heat gain during the daytime. Figure 2.22 shows the AITHM at Townsville.

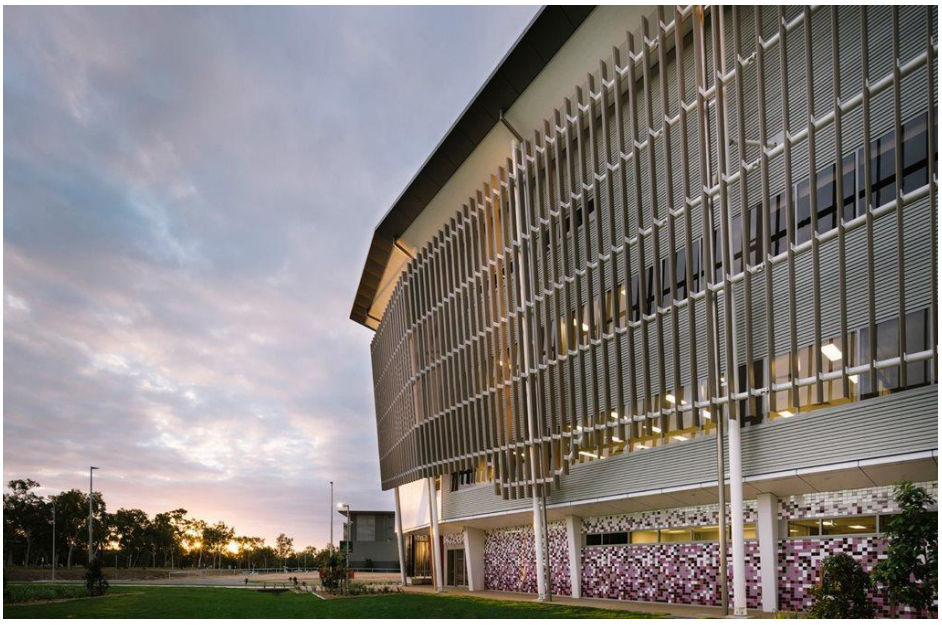

Figure 2.22 - Australian Institute of Tropical Health and Medicine, Townsville, Australia (Architecture & Design, 2017)

AS/NZS 1170.0: 2002, AS/NZS 1170.1: 2002, AS/NZS 1170.2: 2011, AS 1288 - 2006, AS 2047 – 2014, and AS/NZS 1664: 1997 were used to design the AITHM. Wind loads and human impact loads were identified as the critical loads during the design phase of this building. However, snow load and earthquake load were considered to be insignificant compared to wind loads. This building was categorised under cyclonic region C. In addition, while designing this facility, special attention was given to effectively and efficiently handling the hazardous materials within the building. The design engineers have considered a regional wind speed of 73.4 ms^{-1} in their design calculations (Mejorin et al., 2019).

The specifications suggested that the window panels and wall claddings in laboratory areas should resist the flying debris impacts satisfying the guidelines given in AS/NZS 1170.2: 2011. However, the building was designed to resist comparably high internal pressure loads assuming that the remaining envelope glazing could be breached by cyclone debris. Hence, the designers used significantly higher internal pressure coefficient values which are equal to external wind pressure coefficient values (Mejorin et al., 2019). The factored ultimate limit state (ULS) local wind pressure load considered on the debris impact-resistant glazing was 5.1 kPa while applying a ULS pressure of 6 kPa on glass panels at building corners. However, the debris impact phenomenon was not considered for the glass panels at the building corners. As specified in AS 2047 – 2014, 30% of the serviceability limit state (SLS) positive wind pressure of a 25-year return period was considered to check the water penetration resistance of the glass panels (Mejorin et al., 2019).

AS 1288 – 2006 was used to determine the glass thickness. The windborne debris impact resistance of glazing was checked by adopting AS/NZS 1170.2: 2011. Since there is no specification given on the testing procedure and pass/ fail criteria in AS/NZS 1170.2: 2011, the design team followed the testing methods and pass/ fail criterion given in CTS Technical Note No.04 during this project. It should be noted that the glass panels were tested for different impact locations: the centre of the panel; the edge of the panel; and the corner of the panel. The specified debris impact tests were conducted on full-scale test specimens (see Figure 2.23) at the Azuma Testing Laboratory which is accredited by the National Association of Testing Authorities. The glass panels were tested for two successive loads specified in AS/NZS 1170.2: 2011. The test loads were as follows.

Load 1: Debris test using the standard timber missile

Load 2: Debris test using five standard spherical steel balls

For acceptance criteria, engineers considered two main aspects: (i) Glass panel has an ability to prevent penetrations; (ii) If the panel is penetrated, the maximum width of the aperture is less than 8 mm. A fixed glass window with a maximum nominal frame size of 2000 mm (height) × 900 mm (width) and a sash window with a maximum nominal frame size of 900 mm (height) × 1800 mm (width) have been used as the impact-resistant window types in this building. The glass openings are properly supported by the concrete structure or steel sections. Traditional aluminium-framed

window panels have been used in this building which can provide better weather resistance. Additionally, an extra aluminium adapter frame has been attached to the traditional window frame to improve its debris impact resistance. For debris impact-resistant glazing, an 18.84 mm thick heat-strengthened LG has been used. The window panels were tested at an impact speed of 37 ms^{-1}. After conducting these tests, it was found that the selected window panels satisfy the desired impact-resisting requirements.

Figure 2.23 - Fixed glass window used in mock-up test (Mejorin et al., 2019)

Based on the test results, some key lessons learned from this case study can be highlighted as follows. The recent revisions of the Australian wind code suggest considering increased projectile velocity based on the regional wind velocity. Therefore, it is important to select an economically viable window type that performs well under critical debris impact loads. Interlayer materials are effectively used to reinforce the glass panes to improve their resistance to sudden impact loads. While designing impact-resistant glazing, sufficient care must be taken to strong support system for the façade panels. By adopting cost-effective methods, nowadays, designers have found innovative façade solutions with thin glass held in a narrow glazing pocket

which can effectively resist the tension forces at the glass edges during sudden impact loads.

2.7 Material Behaviour and Failure Analysis

Material failure is one of the important aspects of material science. Considering the failure mechanism of materials, two main types of engineering materials can be identified. They are brittle materials and ductile materials. LG is composed of both brittle and ductile materials. For instance, glass panes are brittle while interlayer and sealant materials show ductile behaviour. Therefore, the material behaviour of these composed materials under sudden impact loads and their failure criteria adopted in the present study are discussed in this section.

2.7.1 Glass

Glass is a brittle material. It shows very little or no plastic deformations. Predicting the behaviour and failure of glass is a challenging task because random surface flaws and scratches across the glass panel also lead to brittle fractures. Since glass is brittle in nature, it cannot withstand the high strains.

Comprehensive research studies have been conducted to investigate the dynamic material properties of float glass (Holmquist et al., 1995; Peroni et al., 2011; Zhang et al., 2012; Zhang et al., 2014; Zhou et al., 2019). Holmquist et al. (1995) carried out quasi-static tension and compression test, Split Hopkinson Pressure Bar (SHPB) test, flyer plate test, and depth of penetration ballistic impact tests on float glass (Holmquist et al., 1995). They conducted SHPB tests at two strain rates: 1×10^{-3} s^{-1}; and 250 s^{-1}. By using the test results, they developed the Johnson-Holmquist Ceramic constitutive (JH-2) model to model float glass considering the strain rate effects and material damage. However, during the testing procedure, tests were conducted at two strain rates as it was mentioned previously.

The standard compressive tests were conducted on float glass by Peroni et al. (2011) to study the strain rate effects on the compressive and tensile strength of glass (Peroni et al., 2011). They conducted the tests at different strain rates in the range of 1×10^{-3} s^{-1} to 1000 s^{-1}. The standard test equipment was used for quasi-static tests while using a SHPB for dynamic tests. Their compressive test results show that the effect of strain rate on ultimate compressive strength and Young's modulus is very small. However, they observed a significant increment in ultimate tensile strength while increasing the strain rate. For example, while increasing the average test speed from 9×10^{-3} ms^{-1} to 7.7 ms^{-1}, the ultimate tensile strength showed an increment of about 30 MPa from 60 MPa to 90 MPa.

Zhang et al. (2012) performed laboratory experiments to investigate the effects of strain rate on strength and Young's modulus of glass (Zhang et al., 2012). Firstly, they conducted quasi-static tests to find the static strength and Young's modulus of annealed glass. According to their test results, at a strain rate of 1.33×10^{-4} s^{-1}, the

average static compressive strength and Young's modulus of glass were about 256 MPa and 66 GPa respectively. After that, dynamic compressive tests were conducted on annealed glass using a modified SHPB at strain rates from 98 s^{-1} to 376 s^{-1}. In addition, split tensile tests (Brazilian tests) were conducted at strain rates from 35 s^{-1} to 990 s^{-1} to determine the effects on the tensile strength of glass. After analysing the test results, they found that both the compressive and tensile strengths of glass are sensitive to the strain rate. For instance, at strain rates of 100 s^{-1} and 375 s^{-1}, the average compressive strengths were 475 MPa and 700 MPa respectively. In addition, their split tensile test results showed an ultimate tensile strength of 24 MPa and 34 MPa at the strain rates of 58 s^{-1} and 696 s^{-1} respectively. Therefore, they found that the increment of compressive strength of annealed glass is more substantial compared to its tensile strength. However, the test results revealed that the effect of strain rate on the Young's modulus of glass is negligible. After analysing the test results, Zhang et al. (2012) formulated empirical relations between strain rate and Dynamic Increment Factor. They developed different sets of formulae to determine the Dynamic Increment Factor for compressive and tensile strength of glass separately.

Zhang et al. (2014) carried out extensive laboratory experiments together with comprehensive numerical simulations to study the dynamic material properties of annealed soda-lime glass and to check the accuracy of the Johnson-Holmquist Ceramic constitutive (JH-2) model in modelling annealed glass especially under high strain rates (Zhang et al., 2014). They conducted static compressive tests and dynamic compressive tests on glass specimens using a SHPB. Subsequently, the test results were used to determine the constitutive constants of the material model and to study the strain rate effects. After that, the new JH-2 model was verified by conducting a SHPB compressive test, a field blast test on LG panels, and a full-scale flying debris impact test on LG panels and comparing the test results with the numerical results. Their findings indicated that the new JH-2 model can approximately predict the behaviour of annealed soda-lime glass with a good accuracy. In addition, they found that the original JH-2 model overestimate the strength of glass currently used in practice. Therefore, the original JH-2 model shows limited damage under the dynamic impact and blast loads. The different chemical composition and surface treatments of modern glass compared to the glass used years ago can result in a notable difference between the original and new JH-2 models. For example, considering environmental conditions, currently, manufacturers are trying to optimise SiO_2 composition in glass and use lower percentages which will result in slightly lower strength (Zhang et al., 2014).

Zhou et al. (2019) carried out research studies to perform damage assessment of float glass under blast loads (Zhou et al., 2019). They combined the JH-2 model parameters found by Zhang et al. (2014) with the findings made by Holmquist et al. (1995) and other relevant experimental results. After that, they proposed a new set of parameters for the JH-2 model. The proposed model was used in their numerical models to simulate the blast behaviour of float glass and found that the new material model can approximately predict the material damage of float glass under blast loads.

The failure criterion of glass can be defined by analysing principal stresses: 1st principal stress (σ_{11}); 2nd principal stress (σ_{22}); and 3rd principal stress (σ_{33}) (Hidallana-Gamage et al., 2014). The σ_{11} and σ_{33} denote the largest and smallest stress components respectively. The σ_{11} usually gives the tensile stress of glass. The addition of the hydrostatic stress (σ_{Hyd}) and the deviatoric stress (σ') in a particular direction gives the principal stress in the same direction. The σ_{Hyd} and σ' account for the volumetric strain and the shape change of the material respectively. The principal stress can exceed the tensile strength of glass (T). After conducting a comprehensive research study, Hidallana-Gamage et al. (2013) found that T = 60 – 65 MPa for blast loads (Hiallana-Gamage et al., 2013). The glass material is considered to fail if the maximum principal stress of the glass element exceeds the dynamic breaking strength of glass (T_b) (i.e. $\sigma_{11} > T_b$) (Hidallana-Gamage et al., 2014). This failure criterion was used to identify the glass failure in the present study. In the present study, the dynamic breaking strength of annealed glass is taken as 80 MPa (Cormie et al., 2009; Hidallana-Gamage et al., 2014). However, the random surface flaws and micro-cracks will result in a further reduction in T_b (Netherton & Stewart, 2009). In addition, T_b reduces with age as the glass ages (Hidallana-Gamage et al., 2014).

2.7.2 Polyvinyl Butyral (PVB) Interlayer

In this study, PVB is considered as the interlayer material of the LG composite. Pure PVB shows some stiff and brittle behaviour. However, the ductility and toughness of PVB can be improved by adding plasticisers. PVB has a glass-liquid transition point at temperatures around 18°C to 25°C (Hidallana-Gamage, 2015). Consequently, PVB shows significant changes in shear modulus even under the small changes in temperature.

Previous researchers have done comprehensive studies on the material behaviour of PVB (Nawar et al., 2021; Suwen et al., 2018; Zhang et al., 2015). Zhang et al. (2015) conducted low-speed and high-speed uniaxial tensile tests at different strain rates ranging from 8×10^{-3} s^{-1} to 1360 s^{-1} to investigate the mechanical properties of PVB (Zhang et al., 2015). The low-speed tensile tests were conducted at a temperature of 23°C ± 5°C by using Baldwin and Instron hydraulic testing machines. A high-speed servo-hydraulic testing machine was used in high-speed dynamic tests. The high-speed dynamic tests were conducted on PVB at a temperature of 30°C ± 3°C at strain rates in the range of 8.6 s^{-1} to 1360 s^{-1}. By analysing the test results, Zhang et al. (2015) found that PVB shows viscoelastic properties when it is subjected to quasi-static loading. After that, PVB material undergoes a transition from a viscoelastic state to a bilinear viscoelastic state as the strain rate further increases. Furthermore, they found that the pseudo yield stress tends to increase with the strain rate. They noted that the pseudo yield stress is nearly 3 MPa at a strain rate of 8 s^{-1}, and about 20 MPa at a strain rate of 1360 s^{-1}. However, the pseudo yield strain did not show any significant increment while increasing the strain rate in the tested range. The yield stress increases because of the growth of the initial modulus. The test results showed that the engineering failure stress of PVB was approximately 24 MPa at a strain of 8×10^{-3} s^{-1}

and nearly 40 MPa at a strain rate of 1360 s^{-1}. The corresponding failure stains at these two strain rates were about 280% and 140% respectively. Additionally, for dynamic tests, it was found that the secondary modulus of PVB is insensitive to strain rate.

Suwen et al. (2018) carried out experimental and analytical studies to study the mechanical behaviour of PVB under varying strain rates and temperatures (Suwen et al., 2018). An Instron high-speed servo-hydraulic testing machine was used during the testing procedure. They conducted their tests at strain rates in the range of 6×10^{-2} s^{-1} to 200 s^{-1}, and temperatures of -30°C, -5°C, 25°C, and 40°C. They found that PVB shows viscoelastic properties at low strain rates and high temperatures. It was revealed that the PVB behaviour gradually transforms into an elasto-plastic state from a super-elastic state while increasing the strain rate or decreasing temperature. The initial modulus of PVB showed a wide range of variation from 1 MPa to 600 MPa within the tested strain rate range and temperatures. The test results indicated that the initial modulus tends to increase as the strain rate increases. However, the initial modulus of PVB decreased as the temperature getting higher. It was evident that the strain rate effects are significant at lower temperatures. The true failure stress of PVB increased with strain rate and varied in the range of 24 MPa to 129 MPa during the testing procedure. On the contrary, the true failure strain of PVB decreased with strain rate and varied from 0.861 to 1.308. However, the effect of temperature on true failure stress and strain was not very clear, and it did not exhibit any distinct variation. Suwen et al. (2018) observed that the pseudo-yield stress of the material increases as the strain rate increases, whereas an increase in temperature leads to a decrease in it. The pseudo yield strain also decreased with temperature. However, the effect of strain rate on pseudo yield strain was not significant under the tested range. Furthermore, it was found that PVB exhibits good energy absorption performance at high strain rates and low temperatures.

Nawar et al. (2021) performed an experimental program using an impact drop weight apparatus together with an analytical study to investigate the dynamic behaviour of PVB and ultraviolet-cured one-component acrylic resin (UVEKOL-S) interlayer materials used in LG (Nawar et at., 2021). Their research findings that are relevant to the PVB material are reviewed in this paragraph. They followed a different methodology to conduct their experiments compared to the previous studies and conducted dynamic tests on identical virgin PVB specimens and extracted PVB specimens. The virgin PVB specimens were obtained from rolled PVB sheets, whereas the extracted PVB specimens were extracted from LG panels that had been tested up to their failure by using a water chamber. Since the extracted PVB specimens had been subjected to a lamination process, they were softer compared to the virgin PVB specimens. Nawar et al. (2021) conducted their tests at average stain rates varied from 30 s^{-1} to 40 s^{-1}. It was found that Young's modulus of virgin PVB material was 1.6 times greater than that of the extracted PVB material. The hardening modulus of virgin PVB material was 1.2 times greater than that of the extracted PVB material. Nawar et al. (2021) have mentioned that the PVB interlayer will not be affected by the glass fragments before the failure of the glass panes and it will be significantly affected by

shards after the failure. Hence, they recommended using Young's modulus of virgin PVB, and the hardening modulus of extracted PVB for engineering designs. By analysing the test results, they proposed a modified bilinear model for PVB to use for design purposes. The yield stress, initial Young's modulus, hardening modulus, and failure strain of this newly proposed model are 11.41 MPa, 221 MPa, 9.45 MPa, and 1.60 mm/mm respectively. Furthermore, it has been noted that the mechanical properties of PVB material found from quasi-static test results cannot be used to simulate the behaviour of PVB under dynamic loadings such as impact and blast loading. Additionally, Nawar et al. (2021) have mentioned that the dynamic behaviour of PVB material, observed during their research, cannot be accurately represented solely by modifying static material parameters using dynamic increment factors. It was found that the initial modulus and dynamic energy of PVB material are sensitive to strain rate. The test results from Nawar et al. (2021) were used in the present research while modelling the PVB interlayer in LS-DYNA.

PVB interlayers show ductile behaviour under impact loads. The distortion energy theory is usually used to study the failure of ductile materials (Hidallana-Gamage et al., 2014). This theory states that the total energy within a system is composed of two components of energy: volumetric (hydrostatic) strain energy; and shape (distortion) strain energy, and the failure will occur if the distortion energy surpasses the energy at the yield point of the material observed in a simple tensile test. In this context, the failure criterion of the material can be defined in terms of Von Mises stress (σ_v) and yield stress (σ_y) of the material, where failure occurs when σ_v exceeds the σ_y (i.e. $\sigma_v > \sigma_y$). Since the failure stress of PVB is greater than its yield stress, this approach is conservative. Hidallana-Gamage et al. (2014) used this failure criterion to study the failure of PVB interlayer and structural silicone sealant joints used in LG window panels under blast loads (Hidallana-Gamage et al., 2014). The same criterion is used in this thesis to study the failure of the PVB interlayer.

2.7.3 Structural Silicone Sealant

Structural silicone sealant contains a special polymer called polydimethylsiloxane (PDMS) in its chemical composition. PDMS shows viscoelastic properties and improves the durability and elastomeric properties of silicone sealant materials. Silicone sealant has a glass transition temperature of about -120°C. Therefore, silicone sealant is in the rubbery region at room temperature and shows comparatively less sensitivity to temperature fluctuations in the proximity of room temperature. In comparison to its tensile strength, structural silicone sealant exhibits relatively high ultimate shear strength. As a result, the silicone sealant joints can effectively resist the in-plane deformations induced by the sudden impact loads (Hidallana-Gamage, 2015). The strain rate influences the mechanical properties of silicon sealant. Figure 2.24 shows the stress-strain behaviour under tension for a typical silicon sealant material at two distinct movement rates: 8×10^{-4} ms^{-1}; and 5 ms^{-1} (Yarosh et al., 2008). It was found that the tensile strength and corresponding strain of silicon sealant increased by 200% and 250% respectively as the movement rate increased from 8×10^{-4} ms^{-1} to 5

ms^{-1} (Yarosh et al., 2008). Figure 2.24 demonstrates that silicon sealant exhibits elastoplastic characteristics when it undergoes high strain rates. Furthermore, it was found that some improvements can be seen in the strength parameters of silicon sealant as the strain rate gets higher (Hidallana-Gamage, 2015).

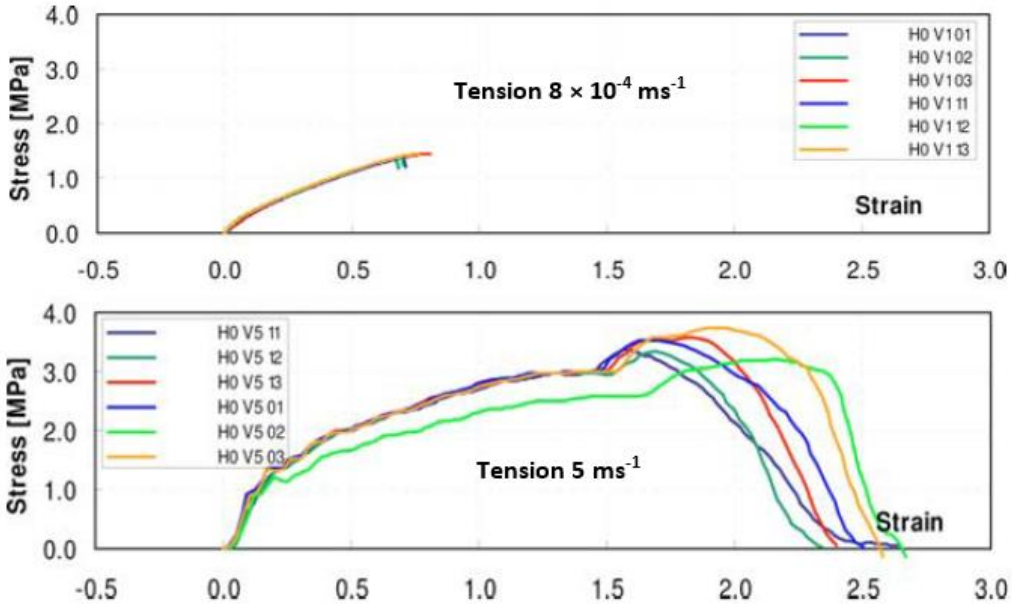

Figure 2.24 - Stress-strain curves of a typical silicon sealant specimen in tension at different movement rates (Yarosh et al., 2008)

Hidallana-Gamage (2015) performed a comprehensive numerical analysis to examine the blast behaviour of LG window panels and silicon sealant material was considered as an elastoplastic material that has a failure strain of 2.5, and a failure stress of 3.5 MPa. In addition, the density, Young's modulus, Poisson's ratio, and yield stress were treated as 1100 kgm^{-3}, 2.3 MPa, 0.495, and 2.3 MPa respectively (Hidallana-Gamage, 2015). Figure 2.25 shows the stress-strain characteristics of silicon sealant material used by Hidallana-Gamage (2015). The accuracy of this material model was checked by conducting a comprehensive validation procedure (Hidallana-Gamage, 2015; Hidallana-Gamage et al., 2014). The same validated material properties of silicon sealant are used in the present study.

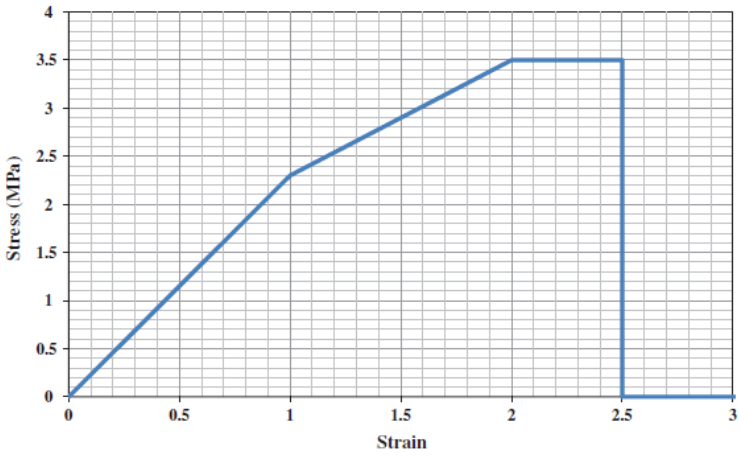

Figure 2.25 - Stress-strain curve of silicon sealant material (Hidallana-Gamage, 2015; Hidallana-Gamage et al., 2014)

As it was explained previously for PVB in Section 2.7.2, the same conservative failure criterion is considered while examining the failure of silicon sealant material in the present study, where the silicon sealant is treated as failed when the Von Mises stress exceeds its yield stress (Hidallana-Gamage et al., 2014).

2.8 Previous Impact Studies on Laminated Glass (LG)

LG is a widely used load-bearing safety glass material. Hence, it is currently used in a wide range of structural applications, including glass façades and window panels. Previous researchers have carried out extensive studies on the impact behaviour of LG (Chen et al., 2017; Huang et al., 2021; Liu et al., 2015; Teotia & Soni, 2018; Wang et al., 2021; Yuan et al., 2017; Zhang et al., 2020; Zhang et al., 2014; Zhang et al., 2013; Zhao et al., 2019). Their studies are summarised and reviewed in this section.

Chen et al., (2017) thoroughly reviewed the numerical simulation techniques used to simulate the impact failures of automotive LG panels (Chen et al., 2017). They found that the element deletion method, discrete element method, combined discrete-finite element method, continuum damage method, cohesive zone modelling, and extended finite element method have been widely used in numerical studies to simulate automotive LG cracking. They have mentioned that generally, the combined discrete-finite element method, extended finite element method, and cohesive zone modelling method have been used to simulate the glass cracking of small LG specimens while using the element deletion method for real-size automotive windshield panels. Furthermore, Chen et al. (2017) pointed out that previous studies have used three different approaches for the adhesion modelling of LG. They are the shared-node approach, the penalty-based approach, and the intrinsic cohesive zone modelling approach. The shared-node approach is the simplest method which assumes a perfect bond between the glass pane and interlayer material. The tied contact algorithm in LS-DYNA introduces similar behaviour to that of the shared-node approach. The penalty-based approach usually resists the relative movements between the glass pane and interlayer material by introducing penalty springs. The tie-break algorithm in LS-DYNA is based on the penalty-based approach. The intrinsic cohesive zone modelling approach can be used to model the adhesion between glass and interlayer by accounting for their debonding behaviour. The shared-node approach is used in the present study by considering a perfect bond between glass and PVB interlayer.

Huang et al. (2021) proposed a nonlinear analytical model for square shape simply supported LG panels to predict their behaviour at the pre-crack stage under low-velocity hard body impacts and verified the accuracy of their model by comparing the analytical results with the experimental results obtained from the drop weight impact tests (Huang et al., 2021). They found that the peak impact force results obtained from their analytical model showed good consistency with their experimental results at impact velocities lower than 1.22 ms^{-1}. However, the analytical model slightly overestimated the peak impact force as the impact velocity exceeded 1.22 ms^{-1}. The average difference between the analytical and experimental results was 2.76% with a

standard deviation of 2.67. It was also found that the impact performance of LG varied with the viscoelastic properties of different interlayer materials because varying cushion effects of polymeric interlayers usually lead to changes in the stress wave propagation patterns through LG. The research findings indicated that the effect of the elastic modulus of interlayer material on pre-crack impact force was less substantial. In addition, it was observed that the impact force could be reduced by more than 63% by using a safety window film. Furthermore, it was revealed that the material indentation decreased with the thickness of the safety window film.

A comprehensive numerical study was carried out by Liu et al. (2015) together with an experimental program to investigate the energy absorption mechanism of PVB LG windshield under head impact. The experimental studies were conducted at different impact velocities ranging from 6.6 ms^{-1} to 11.2 ms^{-1}, and different impact angles varying from 60^0 to 90^0. They identified three stages in the energy absorption process, named as glass failure stage, the large deformation stage, and the rebounding stage (Liu et al., 2015). It was found that the peak headform acceleration is sensitive to impact speed and impact angle, as it increased with impact speed or impact angle. In addition, the energy absorption plateau was found to be increased and appeared earlier as impact speed getting higher, or impact angle getting lower. It should be noted that the effect of PVB interlayer on energy absorption of windshield was examined using two evaluation indexes: maximum counter force on headform; and head injury criterion. It was revealed that the maximum counter force solely depends on the properties of the glass layer and it is insensitive to the mechanical properties of PVB. However, both the glass failure and crack propagation pattern and the deformation of the PVB interlayer showed a combined effect on the head injury criterion value. It was also found that the head injury criterion value is very sensitive to the interlayer thickness. Furthermore, it was observed that the influence of Young's modulus and yield stress of PVB on evaluation indexes was negligible.

Teotia and Soni (2018) reviewed the FE techniques that have been used by previous researchers to perform failure analysis of LG. In their comprehensive review, they highlighted the major challenges of the FE modelling of LG. While developing FE models, special care must be taken to avoid poor interpretations and erroneous modelling methods in order to obtain correct results. In addition, mesh size convergence is also another challenge. Because larger mesh sizes usually introduce high-frequency energies to the model. Therefore, they recommended conducting a mesh convergence study to select an optimum mesh size. Moreover, adhesion modelling and material modelling have also been identified as challenging tasks. Teotia and Soni (2018) recommended to use of 2D modelling techniques in comparative analysis and 3D models in numerical analysis where a higher level of accuracy is required. The 3D FE modelling approach was adopted in the present study.

Wang et al. (2021) studied the impact behaviour of multi-layered LG under low-velocity hard body impact at the pre-crack stage (Wang et al., 2021). Firstly, they conducted drop-weight impact tests on LG specimens. After that, an analytical model was developed to predict the impact response of LG using the test results. Test results

indicated that: the indentation of the impactor into the glass pane played a dominant role in glass failure; the time interval for impact response before initiating the cracks was within 0.6 ms. Additionally, it was revealed that the input energy appeared to be transferred to the glass panel during the timeframe of 0.5 ms to 0.6 ms as the impact velocity got closer to the threshold fracture velocity. The developed analytical model based on these test results was then validated with experimental data. While conducting the validation procedure, it was also found that the interlayer type and its thickness had less influence on impact force at the pre-crack stage (Wang et al., 2021). Finally, they conducted a parametric study to examine the effect of the number of glass layers, glass thickness ratio, and panel size on the pre-crack impact behaviour of multi-layered LG. The findings from the parametric study showed that the pre-crack impact response was insensitive to the glass thickness ratio when the total thickness of glass layers was kept constant. However, the increase of peak force and indentation exhibited a significant variation with the increase of total glass thickness when the thickness was greater than 24 mm. When the thickness became 57 mm, it showed less sensitivity (Wang et al., 2021). Furthermore, it was observed that the pre-crack impact response was more sensitive to the panel size compared to the total glass thickness.

Yuan et al. (2017) developed an analytical model to predict the nonlinear deformation and glass damage of fully clamped rectangular LG panels under low-velocity impact (Yuan et al., 2017). They used first-order shear deformation plate theory and damage mechanics concepts while developing their model. An experimental program was conducted to verify the accuracy of the analytical model using PVB and SentryGlas® Plus (SGP) laminates. It was observed that the LG panel composed of stiff interlayer material (i.e. SGP) exhibited comparatively lower central deflection and higher contact force. In addition, the results indicated that comparatively thin LG panels with thin interlayers showed significant maximum central deflections and minimal first peak contact force (Yuan et al., 2017). Meanwhile, they identified that the proposed analytical model can efficiently produce reliable results compared to the FE models.

Zhang et al. (2020) examined the impact behaviour of LG with different interlayer materials under low-velocity impact by using a drop-weight apparatus. For their study, they selected four interlayer materials: PVB; SGP; Thermoplastic polyurethane (TPU); and a hybrid TPU/SGP/TPU interlayer. The impact response was studied at four different impact energies: 3 J; 5 J; 10 J; and 15 J. The corresponding impact velocities were about 1.71 ms^{-1}, 2.21 ms^{-1}, 3.13 ms^{-1}, and 3.83 ms^{-1} respectively (Zhang et al., 2020). The test results revealed that PVB and TPU interlayers showed better impact resistance compared to the remaining two types at the impact energies of 3 J and 5 J. The obvious difference in the observed impact behaviour was believed to be attributed to the varying modulus of the interlayers. Since the SGP interlayers usually have comparatively higher stiffness, SGP can introduce relatively high bulk modulus to the LG panel. Consequently, the bending stresses will be higher in the back layers of the LG panel. Meanwhile, it was observed that SGP and the hybrid interlayer exhibited better impact performance at higher impact energies (i.e. 10 J and 15 J). Additionally, it was observed that both the glass panes were fractured after the impacts and the elastic

properties of interlayers significantly contributed to rebounding the impactor. Test results indicated that the impact behaviour of LG was primarily governed by the glass layers, resulting low absorbed energy to impact energy ratio values at low impact energies (i.e. 3 J and 5 J). At higher impact energies of 10 J and 15 J, the viscoelastic behaviour of interlayers affected the rebounding phenomenon of the impactor. As different interlayers have different rate-dependent characteristics, experimental results showed different energy ratio values for different interlayers.

Zhang et al. (2013) conducted a combined experimental and numerical study to investigate the response of LG window panels subjected to windborne debris impact. A standard timber block missile with a cross-section of 100 mm × 50 mm was considered in their study. The study was carried out at different impact speeds, ranging from 9 ms^{-1} to 35 ms^{-1}, and for different debris masses: 2 kg; 4 kg; and 8 kg. Two typical panel sizes, 2000 mm × 1100 mm and 1200 mm × 600 mm were also considered in the study to examine the effect of panel size on impact performance. A testing apparatus with a two-spring actuated catapult system and a high-speed camera was used in their laboratory experiments. Laboratory tests were conducted on four different specimens at an impact speed of 15 ms^{-1}. These test specimens had different configurations with varying interlayer and glass thicknesses. Figure 2.26 shows the impact testing apparatus that was used during their tests. After conducting the experimental program, they used those laboratory test results to validate their numerical models before using those numerical models in their parametric study. It was found that the developed numerical models could approximately predict the glass cracking, maximum dynamic deflection, penetration status, and maximum strain of the back glass pane.

Figure 2.26 - Impact testing apparatus with a two-spring catapult system (Zhang et al., 2013)

Figure 2.27 shows the tested LG panels and their crack patterns. Specimen 4 in Figure 2.27 (c) is smaller than specimens 1 and 2. It was noticed that the smaller LG panel showed some stiffer behaviour than the larger panels, resulting in finer cracks and more brittle damages (see Figure 2.27). Separation of fractured glass fragments from the interlayer was also observed, which is thought to have arisen due to comparatively diminished tensile adhesive strength between glass panes and interlayer film. Another notable finding was that the maximum central strain of the back glass pane decreased as the glass pane got thicker under the impacts that hit the geometric centre of the

panel. For example, the maximum strain values of 7.52 mm thick (i.e. with 3mm thick float glass panes) and 13.52 mm thick (i.e. with 6 mm thick float glass panes) LG panels were 1.54×10^{-3} and 8.90×10^{-4} respectively. In addition, it was observed that the maximum central dynamic deflection decreased with the increase in the thickness of the glass panes. For instance, 7.52 mm thick and 13.52 mm thick LG panels exhibited the maximum central deflection values of 180 mm and 60 mm respectively. Furthermore, it was noticed that the impact performance of LG was very sensitive to the interlayer thickness. LG panel composed of a 1.52 mm thick PVB interlayer was penetrated by the impactor. However, an identical panel composed of a 1.88 mm thick PVB interlayer exhibited better impact resistance by preventing penetration under the same impact load. Anti-penetration performance of a 2000 mm × 1200 mm LG window panel against a 2 kg timber block could be improved by 75% by increasing its PVB interlayer thickness from 1.52 mm to 2.66 mm. For 4 kg and 8 kg timber missiles, results showed 70% and 100% improvements respectively.

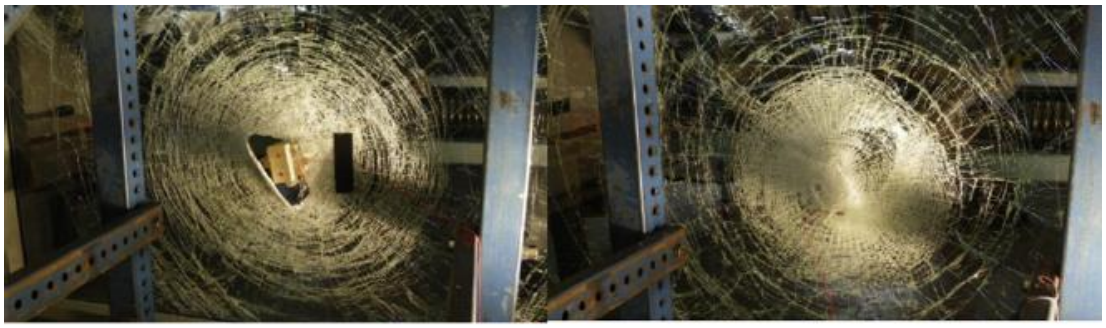

(a) Specimen 1 (b) Specimen 2

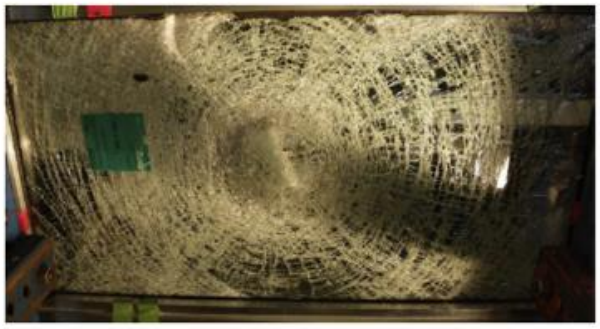

(c) Specimen 4

Figure 2.27 - Tested laminated glass panels (Zhang et al., 2013)

By conducting a parametric study, Zhang et al. (2013) examined the effect of interlayer and glass thickness, panel size, debris mass, and impact velocity on the penetration resistance of LG window panels using a calibrated numerical model. A gradual variation of the experimental strain-time history curve was observed up to its maximum value. However, the numerical strain-time history curve demonstrated a rapid increase at the beginning and a gradual increase thereafter until the failure (Zhang et al., 2013). The difference was thought to be attributed to the extremely fragile failure of the front glass pane, which was induced by the original JH-2 material parameters. It was noted that the crack simulation of glass layers was a significant

challenge during the FE modelling procedure. Three mechanisms were identified in the impact energy dissipation process: energy dissipation due to glass breakage; deformation of the interlayer and its penetration; and window panel vibration. It was therefore noticed that penetration occurred only after the deformation exceeded the ultimate capacity of the PVB interlayer. The penetration vulnerability of a window panel composed of LG which was subjected to smaller debris low-velocity impact was significantly higher than that of an identical window panel subjected to the same impact momentum with a larger debris with high-velocity impact. By getting the summation of the eroded and the detached elements using the numerical models, Zhang et al. (2013) calculated the total volume of the glass fragments. By analysing the total fragment volume, it was realised that the total fragment volume of glass increased with the impact velocity and debris mass before the penetration. The fragment volume reached its maximum value for a given debris mass under an impact velocity that was sufficiently high to introduce penetration. However, the total fragment volume decreased as the impact speed exceeded the penetration velocity. It was also noted that the variation of the total fragment volume satisfied the energy conservation concepts. For example, after the penetration occurs, the debris retains some amount of kinetic energy. Consequently, the fragment volume is reduced satisfying the energy conservation concepts.

As it was explained previously in Section 2.7.1, Zhang et al. (2014) carried out a comprehensive study to identify an appropriate dynamic material for annealed soda-lime glass and developed a modified JH-2 material model for annealed glass. After that, a series of laboratory tests including windborne debris impact tests was performed to verify the accuracy of the newly developed material model together with numerical analysis. It was found that when the debris struck the window panel, the original JH-2 model showed minimal glass damage compared to the modified JH-2 model. This difference was believed to be attributed to the overestimated glass strength of the original JH-2 model. It was noticed that the numerical FE models with the modified JH-2 model could effectively predict the glass crushing at the impact area and brittle damage of the outer glass panes. After conducting the laboratory debris impact tests on a 2000 mm × 1200 mm LG window panel, deflection-time history curves were developed and these curves are shown in Figure 2.28. The thickness of these LG panels was 7.88 mm (i.e. 3 mm thick glass/1.88 mm thick PVB interlayer/3 mm thick glass). Figure 2.28 illustrates that the FE model with the original JH-2 model underestimates the maximum central deflection and dynamic deflection behaviour of the window panel, giving a maximum central deflection of 58 mm, whereas experimental data gives a maximum central deflection of 118 mm. However, the modified JH-2 model showed a maximum deflection of 132 mm and the new model effectively captured the dynamic deflection behaviour of the panel. It is also shown in Figure 2.28 that the original JH-2 model shows stiff behaviour under debris impact, rebounding the debris earlier at 6 ms. The overestimated glass strength introduced by the original JH-2 model has been identified as the reason for this variation. The experimental results from

Zhang et al. (2013) and Zhang et al. (2014) were used to validate the FE modelling techniques in the present research.

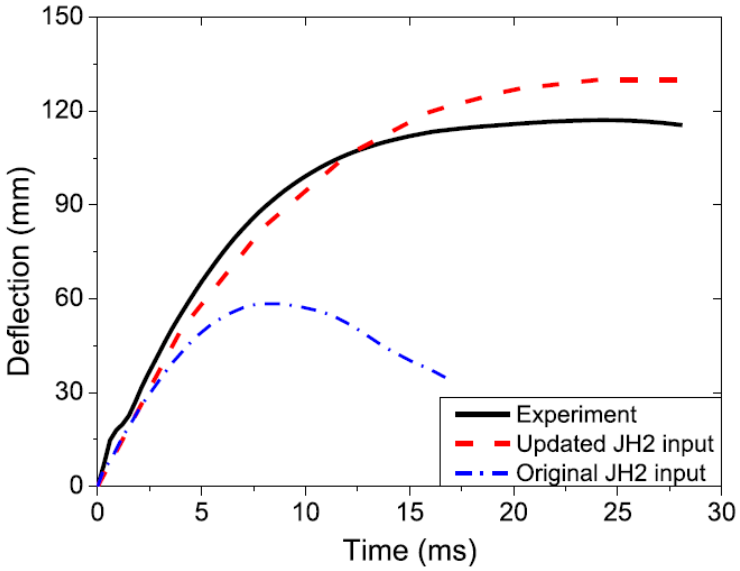

Figure 2.28 - Variation of central deflection of the window panel (Zhang et al., 2014)

Zhao et al. (2019) carried out an experimental program to investigate the post-crack behaviour of SentryGlas® (SG) LG panels. Firstly, a drop-weight impact test apparatus was used to form cracks in glass panes. Then, these cracked LG specimens were subjected to a static load until they collapsed. The post-crack performance of LG panels was evaluated based on their initial stiffness, and peak post-breakage resistance (Zhao et al., 2019). By comparing the post-breakage performance of LG panels under different support conditions, it was concluded that the yield line pattern and post-breakage performance are sensitive to the support condition. For example, the LG panel with simple support (i.e. the LG panel was connected to a steel frame by using neoprene gaskets) and bolted supports (i.e. the LG panel was connected to the support system by using countersunk bolts at four corners) showed X-type and cross-type yield line patterns respectively as shown in Figure 2.29.

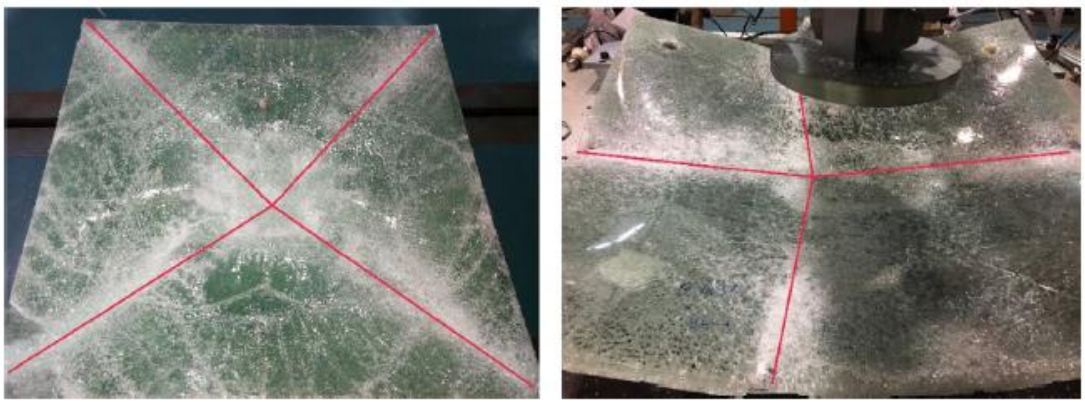

(a) X-type (simple support) (b) Cross-type (bolted support)

Figure 2.29 - Yield line pattern of tested laminated glass (LG) panels (Zhao et al., 2019)

Zhao et al., (2019) found that the initial stiffness of the LG panel with simple support was four times greater than that of the panel with bolted supports. Fully-framed LG window panels are therefore considered in the present study. It was also observed that the crack patterns significantly affect the post-breakage performance of double-layer (i.e. composed of two glass panes and one interlayer) LG panels. It was also noticed that the initial stiffness of the window panel could be improved by 120% by increasing the SG interlayer thickness from 3 mm to 5 mm. The initial stiffness and peak resistance of the tri-layer LG panel (i.e. composed of three glass layers, and two interlayers) was two times greater than that of the double-layer LG panel. However, the tri-layer LG configuration exhibited a central penetration. Compared to a double-layer LG panel, a hybrid LG panel composed of SG and PVB interlayers demonstrated a 19% increase in the initial stiffness and a 27% improvement in the peak resistance. By comparing the post-breakage behaviour of LG panels composed of annealed glass panes and LG with fully tempered glass, it has been concluded that the LG panel composed of annealed glass panes exhibits a superior ability to maintain its load-bearing capacity after breakage (Zhao et al., 2019).

2.9 Chapter Summary

The key findings of the comprehensive literature review and identified knowledge gaps are summarised in this section.

2.9.1 Key Findings of the Literature Review

The key findings of the literature review are summarised below.

- Windborne debris can make severe impacts and damage to building envelopes, particularly glass façades and window panels
- Two main purposes of impact-resistant glazing technologies can be identified. They are: the prevention of internal pressurisation; and confirmation of occupant safety
- LG is a very popular safety glass material used in modern impact- and cyclone-resistant glazing
- While designing buildings in cyclone-prone regions, designers have three options that can be used to prevent possible damages and building failures during strong wind conditions. These options are: impact-resistant shuttered envelopes; impact-resistant façades; and designing buildings to resist high internal wind pressures
- Different chemical composition and surface treatments of modern annealed glass compared to the glass used years ago can result in a notable difference between the previous material models and newly updated material models
- PVB shows viscoelastic properties at low strain rates, and high temperatures and its behaviour gradually transforms into an elastoplastic state from a super-elastic state while increasing strain rate or decreasing temperature
- Silicon sealant exhibits elastoplastic characteristics when it undergoes high strain rates. Furthermore, some improvements can be seen in the strength parameters of silicon sealant as the strain rate gets higher

- Polymeric interlayer films in LG play a prominent role in enhancing the impact resistance of LG
- The layer configuration of the LG panel significantly affects its impact resistance and post-breakage behaviour

2.9.2 Knowledge Gap

After conducting a comprehensive literature review, the knowledge gap was identified. The identified knowledge gap is summarised below.

As it was discussed previously in Section 2.8, comprehensive experimental, numerical, and analytical studies have been conducted by previous researchers to investigate the impact behaviour of LG window panels. However, there is limited research on the impact response of LG window panels subjected to windborne debris impact. Most of the previous debris impact studies on LG panels have examined the influence of the LG panel size, glass and interlayer thickness, layer configuration, impact speed, debris mass, and interlayer material on impact resistance and anti-penetration performance of the LG panels. However, still, there is still limited knowledge of the impact behaviour of LG panels under different support conditions and debris impact locations. It is believed that both the support condition and debris impact location significantly affect the impact performance of LG panels. Because a highly rigid structure undergoes greater force during a dynamic impact compared to less rigid structures. Conversely, less rigid structures, being more flexible, allow the energy or load from the impact to dissipate into the structure as it deflects, thereby absorbing the energy in the process.

Therefore, the research problem (see Section 1.2) of the present research was defined by considering this knowledge gap.

CHAPTER 3

METHODOLOGY AND RESEARCH DESIGN

3.1 Introduction

The research methodology adopted in the current research is presented in this chapter. In addition, this chapter contains a detailed discussion of the FE modelling approach used in this research. At the beginning of this chapter, the detailed research process is explained in Section 3.2. Section 3.3 presents the FE-based numerical procedure that was carried out in this study.

3.2 Research Process

The detailed research process is illustrated in Figure 3.1. Firstly, the research area was identified. Then, a preliminary literature survey was conducted at the beginning of this process which is followed by a comprehensive literature review carried out throughout the entire period of this research. Consequently, the research findings were gathered and the knowledge gap was identified. Subsequently, the research problem was defined considering the identified knowledge gap. After that, the aim of the research was set to address the research problem. The main aim of this research was achieved by attaining five research objectives defined in Section 1.3. The research methodology was formulated to attain the research objectives, ultimately culminating in the main aim. The first objective was to identify the different types of glass façades with LG panels used in buildings. It was achieved by conducting comprehensive case studies on impact-resistant glazing technologies used in current practice. The findings from case studies are discussed in Section 2.6. The second objective was to compare the available design standards and standard testing methods associated with debris impact criteria and the findings are illustrated in Section 2.4. The third objective was to develop and validate FE-based numerical techniques to investigate the behaviour of LG panels under different impact locations and support conditions and it is discussed in Section 3.3 and Chapter 4. Then, the performance of structural silicone sealant and LG panels was evaluated based on the numerical results from validated FE models to attain the fourth objective. Finally, the key findings of the current study were identified (see Section 7.3) and design strategies were formulated (see Section 7.4) for impact-resistant glazing to achieve the fifth objective. Hence, this research ultimately provides design strategies for impact-resistant glazing of building envelopes considering the response of the LG window panels under different support conditions and impact locations to achieve the main aim of the research. This study will therefore extend the existing design domain of LG window panels.

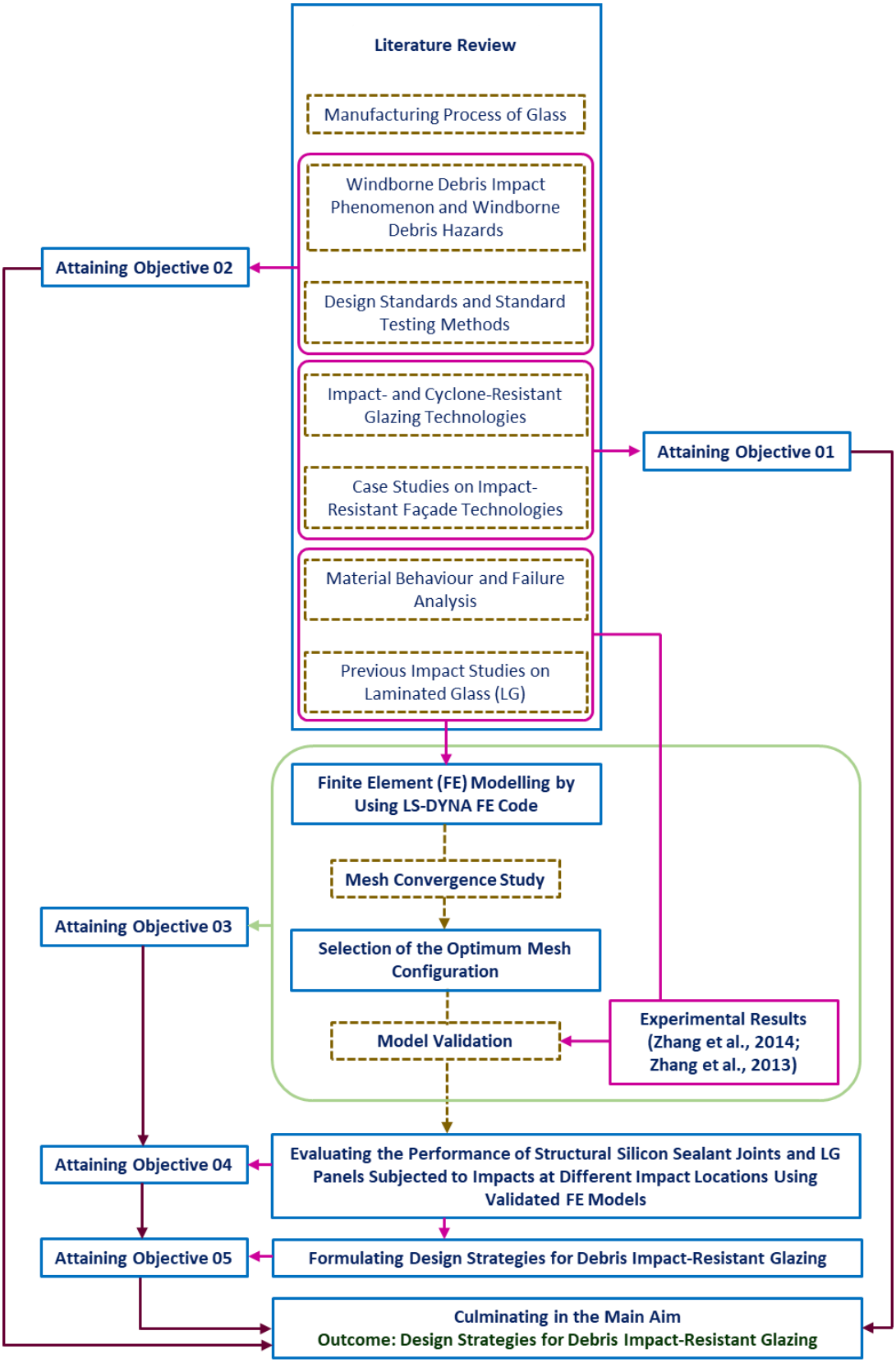

Figure 3.1 – A graphical representation of the research process

3.3 Numerical Modelling

The material models and the modelling techniques used for different materials are explained here from Section 3.3.1 to Section 3.3.3. A detailed explanation of the mesh sizes used in the current analysis is given in Chapter 4.

The thickness of the LG panel is very small compared to its planer dimensions. Therefore, two-dimensional (2D) shell elements or three-dimensional (3D) solid elements can be used to develop numerical models for LG panels (Hidallana-Gamage et al., 2014; Hidallana-Gamage et al., 2013). When using 2D shell elements, users have the option to employ material model 32 (MAT_LAMINATED_GLASS) for modelling the LG panel. However, this approach has some limitations, including challenges of capturing the fractured strength of glass, defining PVB failure, and modelling realistic support conditions. Hence, in this study, it was decided to use material models 110 and 24 that are compatible with 3D solid elements. This led to utilisation of 3D solid elements in the present study. LS-DYNA explicit FE code was used for the numerical simulations. Most of the past research studies do not provide sufficient details on material models, and failure analysis of different materials: glass; PVB interlayer; and structural silicone sealant.

Hence, a comprehensive and reliable FE-based analytical procedure is presented in this thesis to address the above knowledge gap. An LG panel with in-plane clear dimensions (excluding the width of the sealant layers) of 2000 mm × 1200 mm was considered for numerical modelling. The 3D FE model of the panel is shown in Figure 3.2. The width of the 6 mm thick structural silicone sealant layer is 15 mm. As it is shown in Figure 3.2, the LG panel consists of a 1.88 mm thick PVB interlayer and 3 mm thick float glass panes. Firstly, the analysis was done considering pinned support conditions along the perimeter of the LG panel. Then, the effect of the structural silicone sealant layer was examined by modelling a sealant layer along the perimeter of the panel. In the FE model, material model 110 (MAT_JOHNSON_HOLMQUIST_CERAMICS) was used for glass, and material model 24 (MAT_PIECEWISE_LINEAR_PLASTICITY) was used for both the PVB and sealant layer. The wooden debris was modelled using material model 20 (MAT_RIGID).

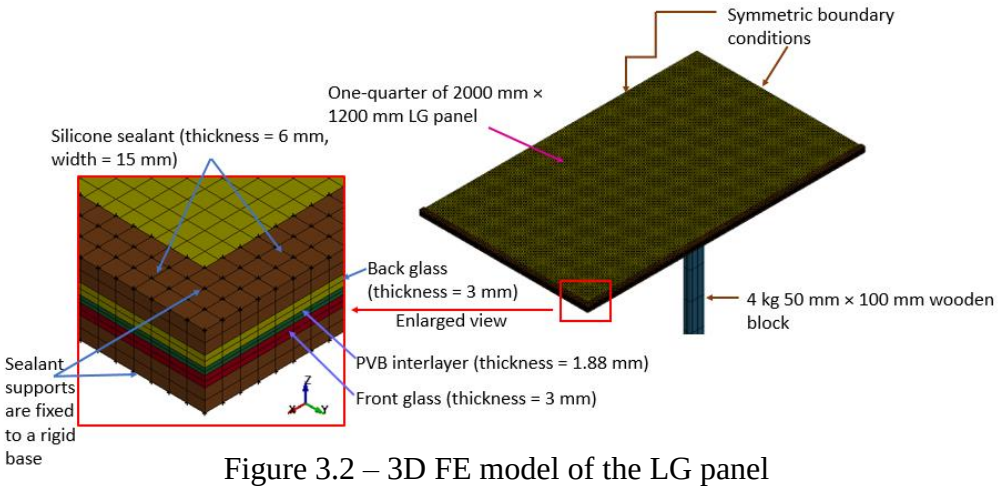

Figure 3.2 – 3D FE model of the LG panel

The impact speed of the wooden projectile is 15 ms^{-1}. The contact between the glass layers and the PVB layer was considered fully bonded. Similarly, a fully bonded contact was considered between the glass pane and the sealant layer as well. Hence, the delamination between the glass and the interlayer material was not considered in this study. The supporting frame of the panel was not modelled considering the simplicity of the model. Therefore, the deformations of the supporting frame were neglected and the relevant nodes of the sealant supports were fixed to a rigid base (Hidallana-Gamage et al., 2014). However, the sealant elements are free to deform with the glass panes.

3.3.1 Modelling of Glass Panes

In the present study, float (annealed) glass was considered as the glass material in the LG panel. Glass is a brittle material. Therefore, it shows a brittle failure in nature. The loading rate affects the fracture strength of glass (Zhang et al., 2013). Since the strain rates are considerably high under the windborne debris impact loads, an appropriate dynamic material model should be used for glass to make reliable predictions based on the numerical simulations. The Johnson-Holmquist ceramic constitutive (JH-2) model is widely used in current practice to model float glass under ballistic impacts (Zhang et al., 2014; Zhang et al., 2013). In the LS-DYNA FE code, material model 110 (MAT_JOHNSON_HOLMQUIST_CERAMICS) is available to model the ceramic composites that are subjected to extreme loads and high strain rates (Hidallana-Gamage et al., 2014; Hidallana-Gamage et al., 2013; Zhang et al., 2014; Zhang et al., 2013). The user can use the material card of the material model 110 to introduce the JH-2 model into the FE model. Johnson and Holmquist proposed the JH-2 model for simulating the ballistic behaviour of brittle materials (Holmquist et al., 1995; Johnson & Holmquist, 1993). The JH-2 model is comprised of a strength model, a model that accounts for the strain rate effects, a damage model, and an equation of state (EOS) and these models and EOS have been defined by a set of mathematical equations. The material parameters and the other important equations involved with the JH-2 model for float glass are briefly explained in this section.

Both the intact strength of the material and the strength at fracture are taken into account in the strength model. Eq. 3.1 gives the normalised equivalent stress (σ^*) of the material in terms of the normalised intact strength (σ_i^*) (see Eq. 3.2), the normalised fractured strength (σ_f^*) (see Eq. 3.3), and the damage scalar (D). The damage scalar (D; $0 \leq D \leq 1$) accounts for the transition of glass material from the intact state (i.e., D = 0) to complete fracture (i.e., D = 1). In Eq. 3.1, all the normalised stresses are calculated by dividing the relevant actual equivalent stresses by the equivalent stress at the Hugoniot Elastic Limit (HEL) (Holmquist et al., 1995; Johnson & Holmquist, 1993).

$$\sigma^* = \sigma_i^* - D\left(\sigma_i^* - \sigma_f^*\right) \qquad \text{Eq. 3.1}$$

$$\sigma_i^* = A(P^* + T^*)^N(1 + C \ln \dot{\varepsilon}^*) \quad \text{Eq. 3.2}$$

$$\sigma_f^* = B(P^*)^M(1 + C \ln \dot{\varepsilon}^*) \quad \text{Eq. 3.3}$$

In Eq. 3.1, Eq. 3.2, and Eq. 3.3, A, *B*, *C*, *M*, and *N* are material constants. P^*, T^*, and $\dot{\varepsilon}^*$ are the normalised pressure, the normalised maximum tensile hydrostatic pressure, and the dimensionless strain rate respectively, where $P^* = P/P_{HEL}$, $T^* = T/P_{HEL}$, and $\dot{\varepsilon}^* = \dot{\varepsilon}/\dot{\varepsilon}_0$ (Holmquist et al., 1995; Johnson & Holmquist, 1993). Here, $\dot{\varepsilon}_0$ is 1.0 s^{-1} and P, T, and $\dot{\varepsilon}$ denote the actual pressure, the maximum tensile hydrostatic pressure, and the actual strain rate respectively. The pressure at the HEL is denoted by P_{HEL}. In the original JH-2 model, Holmquist et al. determined the intact strength constants of glass by conducting static split tension tests, and static and dynamic uniaxial compression tests (Holmquist et al., 1995; Zhang et al., 2014). Although the JH-2 model is widely used in modelling glass material under blast and impact loads, it should be noted that it was initially implemented to model ceramic materials under ballistic impacts (Zhang et al., 2014). Hence, the glass behaviour in the tensile region is not well described in the original model (Zhang et al., 2014). Zhang et al. (2014) highlighted that the original JH-2 model overestimates the strength of float glass that is used currently in practice in window panels. Therefore, after conducting a series of compression and tensile tests on float glass using Split Hopkinson Pressure Bar (SHPB), Zhang et al. (2014) determined a new set of values for the material constants in the JH-2 model by carrying out an extensive validation procedure to simulate the dynamic response of float glass. Zhou et al. (2019) proposed reasonable values for the material constants by combining the available test results, the original values from Holmquist et al. (1995), and the new values from Zhang et al. (2014). Then, they used the validated model parameters to perform extensive simulations. The material constants that have been proposed by Zhou et al. (2019) are used in the present study to model float glass.

The damage level (i.e., the damage scalar, *D*) is defined in Eq. 3.4, where $\Delta\varepsilon_P$is the plastic strain of the material during a cycle of integration and ε_P^fdenotes the plastic strain to fracture under constant pressure, *P*. ε_P^f is defined in Eq. 3.5, where D_1 and D_2 are material constants.

$$D = \sum \varepsilon_P / \varepsilon_P^f \quad \text{Eq. 3.4}$$

$$\varepsilon_P^f = D_1(P^* + T^*)^{D_2} \quad \text{Eq. 3.5}$$

Although the intact strength of glass depends on its surface treatment, it is believed that the surface treatment does not change the material damage of glass and fracture

behaviour (Zhang et al., 2014). Hence, as it has been suggested by Zhang et al. (2014) and Zhou et al. (2019), the damage model that is described in the original JH-2 model is used in the present study to determine D1 and D2 constants.

The hydrostatic compression pressure and the tensile pressure of the glass material are given by Eq. 3.6 and Eq. 3.7 respectively, where K_1 (bulk modulus), K_2, and K_3 are constants.

$$P = K_1\mu + K_2\mu^2 + K_3\mu^3 + \Delta P \quad \text{Eq. 3.6}$$

$$P = K_1\mu \quad \text{Eq. 3.7}$$

μ varies with the deformation of the material and it is defined in Eq. 3.8. Here, ρ and ρ_0 are the current density and the initial density of the material respectively.

$$\mu = \frac{\rho}{\rho_0} - 1 \quad \text{Eq. 3.8}$$

Under compressive loading, excessive deviatoric stress leads to damage accumulation in a material by introducing a buckling pressure term, ΔP in Eq. 3.9. As a result of the accumulation of material damage, incremental internal elastic energy decreases, and this energy is transformed into potential internal energy. The extent to which this transformation occurs is contingent on the variable β (see Eq. 3.9). Typically, β has a value of 1.0 (Hidallana-Gamage et al., 2014). Eq. 3.10 gives the internal energy loss (ΔU). In Eq. 3.10, σ and G denote the effective stress, and the shear modulus of the material respectively, and $U(D) = \sigma/6G$ (Hidallana-Gamage et al., 2014).

$$\Delta P_{n+1} = -K_1\mu + ((K_1\mu + \Delta P)^2 + 2\beta K_1 \Delta U)^{0.5} \quad \text{Eq. 3.9}$$

$$\Delta U = U(D) - U(D_{n+1}) \quad \text{Eq. 3.10}$$

The material parameters that are used in the present research for modelling glass are shown in Table 3.1.

Table 3.1 - JH-2 material constants of annealed glass used in the numerical model (Hidallana-Gamage, 2015; Hidallana-Gamage et al., 2014; Hidallana-Gamage et al., 2013; Meyland & Nielsen, 2020; Zhang et al., 2014; Zhou et al., 2019)

	JH-2 constant	**Value**
Strength constants	A	0.70
	B	0.20
	C	0.035
	M	1.0
	N	0.72
	Max. tensile pressure, T (MPa)	60
	HEL (GPa)	4.50
	HEL strength (GPa)	3.15
	HEL pressure (GPa)	2.40
	Max. normalised fracture strength	0.5
	Shear modulus (GPa)	26.9
	Failure strain	0.0024
	Reference strain rate, $\dot{\varepsilon}_0$	1.0
Damage constants	D_1	0.043
	D_2	0.85
Pressure constants	K_1 (GPa)	43.2
	K_2 (GPa)	-67.2
	K_3 (GPa)	153.2
	Bulk, β	1.0
Density (kgm^{-3})		2530

3.3.2 Modelling of PVB Interlayer

PVB is one of the popular interlayer types that is used in LG panels. As described previously in Section 3.3, PVB is the interlayer material considered in this study, and material model 24 (MAT_PIECEWISE_LINEAR_PLASTICITY) is used in the numerical model to model the PVB interlayer. The validity of this material model has been affirmed by previous authors (Hidallana-Gamage et al., 2014; Hidallana-Gamage et al., 2013). When PVB interlayer materials are subjected to extreme loads, they exhibit elastoplastic characteristics under high strain rates (Hidallana-Gamage et al., 2014). In both tension and compression, material model 24 shows similar stress-strain characteristics (Hidallana-Gamage et al., 2014). To effectively simulate the behaviour of interlayer materials under extreme loadings, the material parameters obtained from quasi-static tests cannot be directly used in the numerical models (Nawar et al., 2021). The material properties of the PVB interlayer used in this study are presented in Table 3.2. The stress-strain variation of the PVB material is illustrated in Figure 3.3.

Table 3.2 - Material properties of PVB used in the numerical model (Hidallana-Gamage et al., 2014; Nawar et al., 2021)

Mass density	1100 kgm^{-3}
Initial Young's modulus	221 MPa
Yield stress	11.41 MPa
Failure stress	28 MPa
Tangent modulus	5.25 MPa
Poisson's ratio	0.485

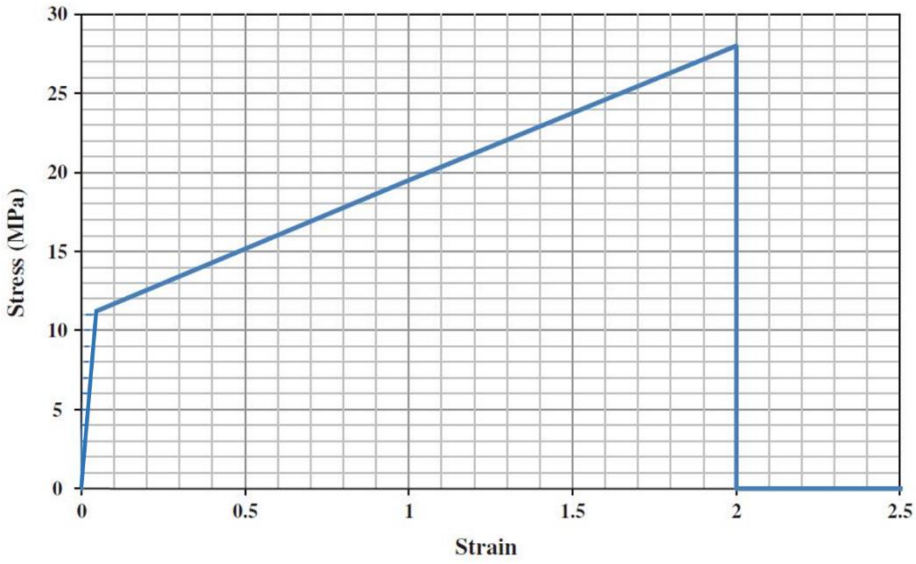

Figure 3.3 - Stress-strain variation of the PVB interlayer

3.3.3 Modelling of Structural Silicone Sealant Joints

While manufacturing LG window panels, manufacturers typically use rubber and silicone sealant along the perimeter of the panels as the structural sealant materials (Hidallana-Gamage et al., 2014). Structural silicone sealant is used as the sealant material in this study. It shows elastoplastic behaviour under extreme loadings. To simulate the behaviour of silicone sealant joints under extreme loadings in LS-DYNA, previous authors have used and validated material model 24 (MAT_PIECEWISE_ LINEAR_PLASTICITY) in their studies (Hidallana-Gamage, 2015; Hidallana-Gamage et al., 2014; Hidallana-Gamage et al., 2013). In this study, material model 24 is therefore used to model the sealant joints. The material properties of the silicone sealant used in the present study are shown in Table 3.3. The stress-strain variation of the sealant material is illustrated in Figure 2.25.

Table 3.3 - Material properties of silicone sealant used in the numerical model (Hidallana-Gamage, 2015)

Mass density	1100 kgm^{-3}
Young's modulus	2.3 MPa
Yield stress	2.3 MPa
Failure stress	3.5 MPa
Failure strain	2.5
Poisson's ratio	0.495

3.4 Chapter Summary

In this chapter, the methodology of the research was presented with a detailed description of the FE modelling approach adopted in the present study. A graphical representation of the research process (see Figure 3.1) has been included in Section 3.2 to visualise the steps in the methodology by mapping those steps with the relevant objectives attained in the current study.

The FE modelling techniques used by the previous researchers were thoroughly reviewed and those techniques were followed while developing the FE models. FE models were developed using 3D constant-stress solid elements in LS-DYNA. Material model 110 (MAT_JOHNSON_ HOLMQUIST_CERAMICS) was used for glass, and material model 24 (MAT_PIECEWISE _LINEAR_PLASTICITY) was used for both the PVB interlayer and sealant joints. The wooden debris was modelled using material model 20 (MAT_RIGID) by assuming it as a rigid material. The material properties and material constants used in the present research were found from

the existing literature and they were also presented in this chapter. The failure criterion and behaviour of glass, PVB, and silicone sealant have been discussed in Section 2.7 and those criteria were adopted to study the material failure in this study. The glass material was considered as failed if the maximum principal stress (σ_{11}) of a glass element exceeds the dynamic breaking strength of glass (T_b) (i.e. $\sigma_{11} > T_b$). The PVB and sealant materials were considered as failed if Von Mises stress (σ_v) exceeded the yield stress (σ_y) (i.e. $\sigma_v > \sigma_y$), which is a conservative approach.

The FE models were validated using previous experimental results and it is presented in Chapter 4.

CHAPTER 4

MESH CONVERGENCE STUDY AND VALIDATION OF NUMERICAL MODELLING TECHNIQUES

4.1 Introduction

This chapter contains the details of the mesh convergence study and numerical model validation procedure. During the FE modelling procedure, a mesh convergence study was conducted to select an appropriate mesh configuration as explained in Section 4.2. After that, the FE modelling techniques were validated by comparing the numerical results of the current study with the previous experimental results from Zhang et al., (2014), and Zhang et al., (2013), and it is discussed in Section 4.3. Consequently, the selected mesh configuration was used in further analysis, discussed in Chapter 5.

4.2 Mesh Convergence Study

Extensive experimental studies have been conducted by Zhang et al. (2013) and Zhang et al. (2014) to study the response of LG panels to windborne debris impacts. Those experimental results were used to validate the numerical techniques used in the present study. As explained previously in Section 3.3, FE models were developed using LS-DYNA explicit FE code. Firstly, a mesh convergence study was conducted to identify the correct element sizes to obtain good results from the FE models. While conducting the mesh convergence study, nine different mesh sizes were considered depending upon the response of the LG panel with varying mesh sizes. 100 × 60 × 3, 100 × 60 × 6, 150 × 90 × 6, 200 × 120 × 3, 200 × 120 × 5, 200 × 120 × 6, 200 × 120 × 7, 200 × 120 × 8, and 250 × 150 × 6 are the different mesh arrangements used in the mesh convergence study. The mesh arrangement, 100 × 60 × 3 indicates 100 elements along the clear length, 60 elements along the clear width, and 3 elements through the thickness of the LG panel. Similarly, the remaining eight arrangements also indicate the number of elements in these three directions. The number of elements through thickness was changed by dividing the two glass skin panes and the interlayer film into small mesh sizes through the thickness. For example, the case with three elements through thickness indicates one element through the thickness per layer. In addition, the case with five elements through thickness represents two elements through the thickness of the glass skin panes and one element through the thickness of the interlayer film. In this thesis, these two cases are denoted by (1/1/1) and (2/1/2) respectively. Likewise, (2/2/2), (3/1/3), and (3/2/3) are the arrangements for the other cases with six, seven, and eight elements through the thickness of the LG panel respectively. The mesh convergence study was conducted by assigning pinned conditions along the perimeter of the panel without modelling the silicone sealant joints to optimise computational efficiency by minimising processing time.

While performing a mesh convergence study, the convergence of maximum dynamic deflection at the geometric centre of the LG panel was checked with different mesh configurations. Figure 4.1 shows the variation of the maximum dynamic deflection under varying mesh configurations in in-plane directions. Figure 4.1 shows that the maximum dynamic deflection converges at the mesh arrangements of 200 × 120 × 6 and 250 × 150 × 6. However, increasing the number of elements beyond 200 × 120 in the in-plane directions does not exhibit an improvement in the results. Hence, 200 × 120 was selected for the in-plane direction.

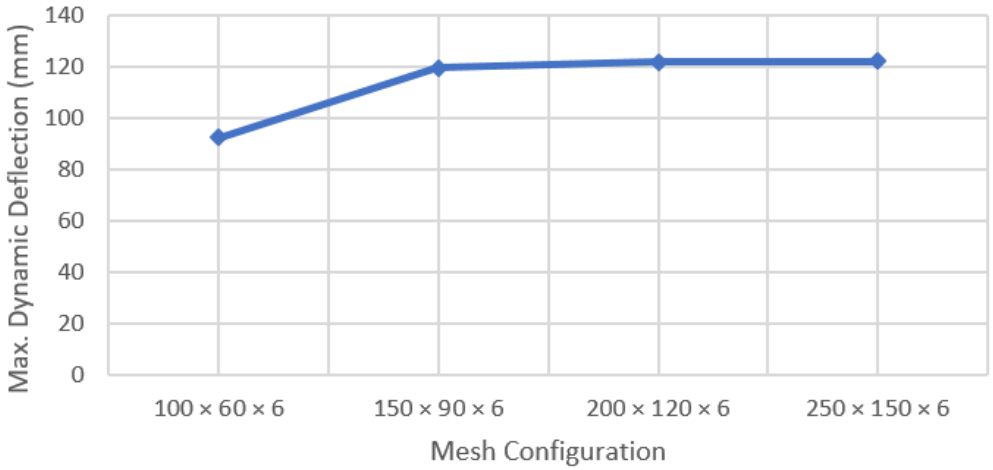

Figure 4.1 - Maximum dynamic deflection for varying in-plane mesh configurations

Afterwards, the effect of varying mesh arrangement through thickness was examined for the in-plane mesh arrangement of 200 × 120. Figure 4.2 depicts the variation of the maximum dynamic deflection under varying mesh configurations through the thickness. It should be noted that while increasing the number of elements through thickness from three to five, the maximum dynamic deflection tends to converge at the mesh arrangements of 200 × 120 × 6. However, further increasing the number of elements through thickness beyond six elements results in a poor aspect ratio in the brick elements, and these poor aspect ratio values lead to introduce shear-locking behaviour. Hence, this shear-locking effect introduces a nonphysical stiffness to the system which can lead to lower deflection values (see Figure 4.2). Shear-locking can be controlled by either using fully integrated 2^{nd} order quadratic elements or by specifying at least three elements across the thickness while using 1^{st} order rectangular elements in the model. For the purpose of achieving efficient and precise simulation, this study employs constant stress solid elements throughout the model, incorporating hourglass stabilisation.

Furthermore, the total energy variation of the LG panel was examined while conducting the mesh convergence study. Figures 4.3 and 4.4 show the results for varying mesh configurations. Figure 4.3 illustrates that the results tend to converge at

the mesh arrangement of 200 × 120 × 6. However, further mesh refinement does not exhibit a significant improvement in the results. Figure 4.4 demonstrates that 200 × 120 × 7 and 200 × 120 × 8 mesh arrangements exhibit slightly reduced maximum total energy values due to diminished deflections of the panel caused by shear-locking behaviour.

Therefore, the arrangement with 200 × 120 × 6 elements was selected as an appropriate mesh arrangement in this study.

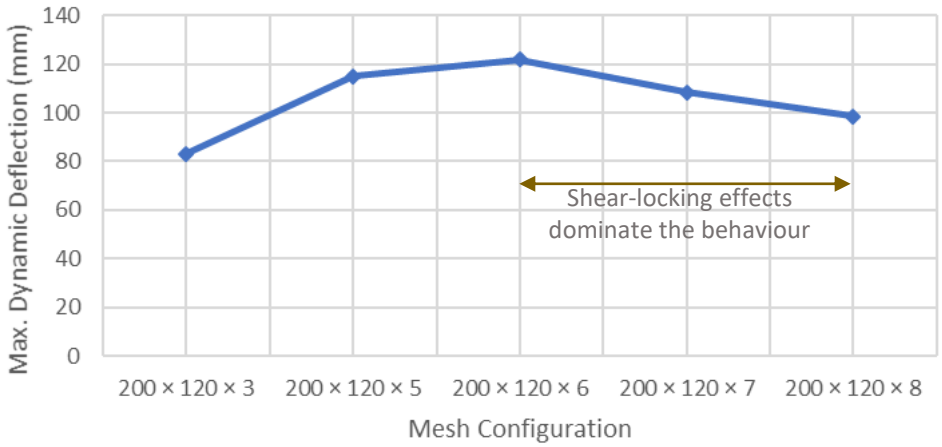

Figure 4.2 - Maximum dynamic deflection for varying through-thickness mesh configurations

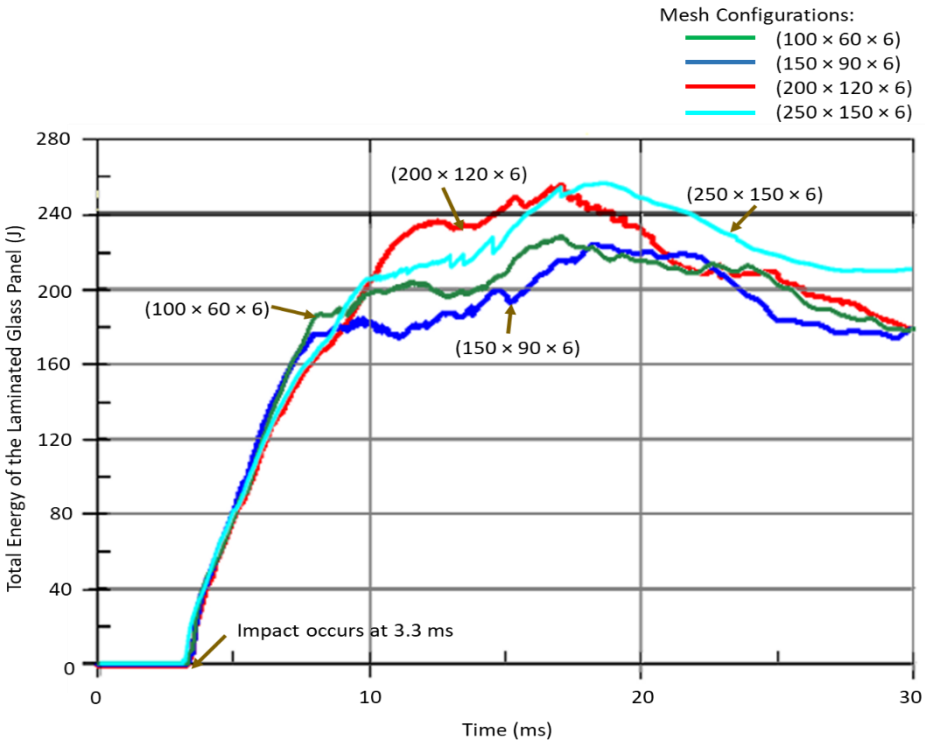

Figure 4.3 - Variation of the total energy of the LG panel for varying mesh configurations

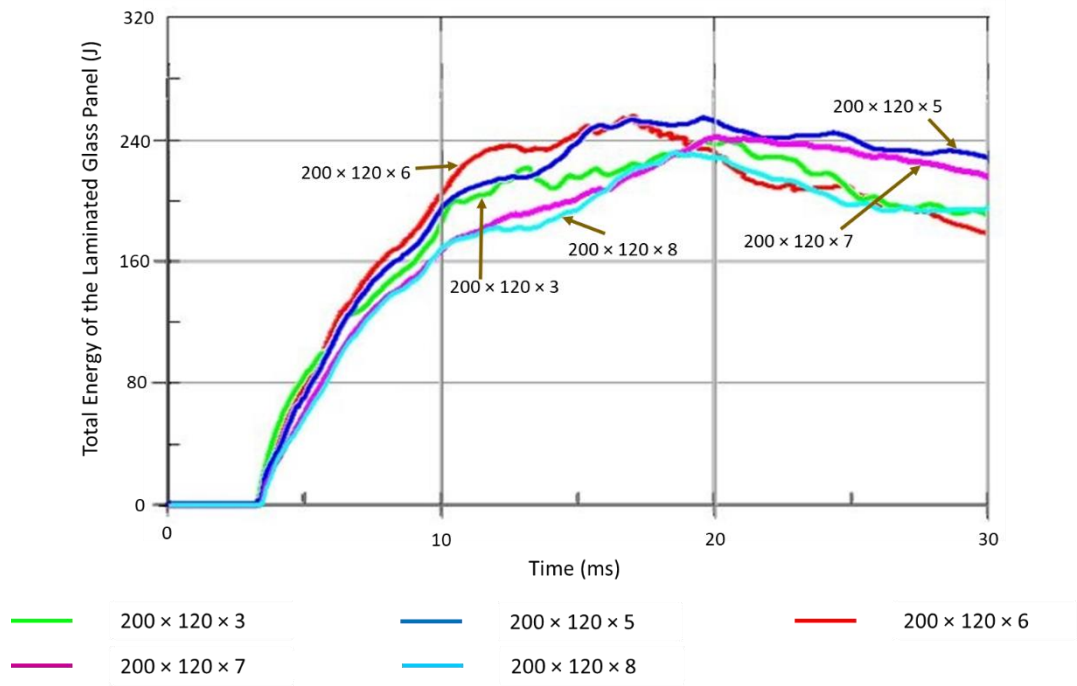

Figure 4.4 - Variation of the total energy of the LG panel for varying mesh configurations

4.3 Model Validation

The selected FE model in Section 4.2 (i.e. the FE model having 200 × 120 × 6 mesh configuration) was validated by conducting a comprehensive validation procedure as illustrated in this section. In addition, the accuracy of the selected mesh configuration was also compared with the accuracy of the other mesh arrangements to clearly visualise the influence of the mesh arrangement on numerical results.

While validating the FE modelling techniques, the experimental and numerical deflection-time history curves at the centre of the back glass pane which were obtained by Zhang et al. (2014) were used. Figure 4.5 illustrates the deflection-time history curves for the nine different mesh arrangements that were discussed previously in Section 4.2 (i.e. case 1 to case 9; see Figure 4.5). It compares the numerical curves of the present study with the previous experimental and numerical curves.

Upon comparing the curves in Figure 4.5, it is evident that the deflection-time history curves vary based on the mesh configurations. Cases 1 and 4, utilizing the (1/1/1) mesh arrangement through the thickness, exhibit undulations, resulting in noticeably lower deflections compared to other mesh arrangements. The (1/1/1) mesh arrangement employs only one element through the thickness of each glass pane and the interlayer, which is insufficient for effectively capturing dynamic deflections. The stress and strain of a glass element depend on those at the integration point, typically at the middle of the element, and the likelihood of the strain exceeding the failure strain is relatively low. However, employing several elements through the thickness of the

glass panes increases the likelihood of strain exceeding the allowable failure strain of the elements at the surface, leading to the deletion of those elements from the model and an overall increase in deflection. In Figure 4.5, the experimental curve shows a slight change in slope at around 1 ms. This can be attributed to potential imperfections in the support system of the test specimen. As a result, the LG panel exhibits a sudden change in deflection in the experimental curve immediately following the impact. However, subsequent experimental results reveal a gradual variation when the support system of the LG glass window panel functions correctly.

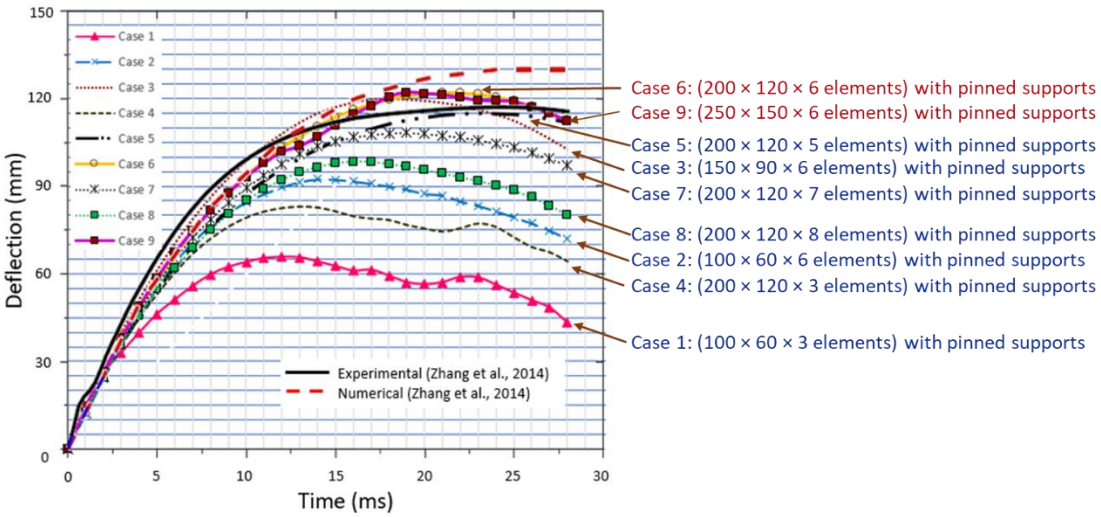

Figure 4.5 - Deflection-time history curves at the centre of the back glass pane of the LG panel subjected to mid-impact

Increasing the number of elements through the thickness yields improvements in the results (see case 2, case 5, and case 6 in Figure 4.5). When layers are divided into finer mesh sizes with more than one element through the thickness, additional elements effectively represent specific layers, even if some elements have been deleted. This finer mesh division enables the good prediction of the complete behaviour of the LG panel. However, as previously explained, cases 7 and 8 exhibit comparatively low deflection values due to the effects of shear-locking behaviour. It is essential to note that the deflection-time history results are highly sensitive to the mesh arrangement in the FE model. Therefore, an FE model with the identified optimum mesh arrangement is crucial for capturing the behaviour of the panel.

Furthermore, the selected mesh arrangement was evaluated by using the L2 norm error method (i.e. root mean square error method of numerical solution). The experimental results obtained by Zhang et al. (2014) were considered as the reference solutions while calculating the L2 norm error (E_{L2}) and E_{L2} was calculated by using Eq. 4.1 where, $D_c\,(i)$ is the panel deflection obtained from the FE model at time i, $D_{exp}\,(i)$ is the panel deflection obtained from the experiment at time i, and N_{exp} is the total number of experimental data points. In Figure 4.6, the experimental curve is plotted from 1 ms to 28 ms. Hence, N_{exp} was considered as 28 while performing the calculations.

$$E_{L2} = \sqrt{\frac{\sum_{i=1}^{N_{exp}} \left(\left\| D_c(i) - D_{exp}(i) \right\|^2 \right)}{N_{exp}}} \qquad \text{Eq. 4.1}$$

Figure 4.6 shows the variation of E_{L2} for varying mesh configurations. By comparing the E_{L2} value of the mesh configurations, 150 × 90 × 6 and 200 × 120 × 5, it can be observed that the error value of the arrangement, 150 × 90 × 6 is comparatively lower than that of 200 × 120 × 5. In the first arrangement, the PVB interlayer has been divided into two elements through thickness. However, in the second arrangement, the interlayer film has been divided into one element through thickness. Therefore, the elastoplastic behaviour of the PVB interlayer cannot be simulated effectively by using only one element through thickness along with the material deletion criterion used for the glass elements. In addition, the 100 × 60 × 6 arrangement has notable errors because of the slightly larger mesh sizes used in in-plane directions.

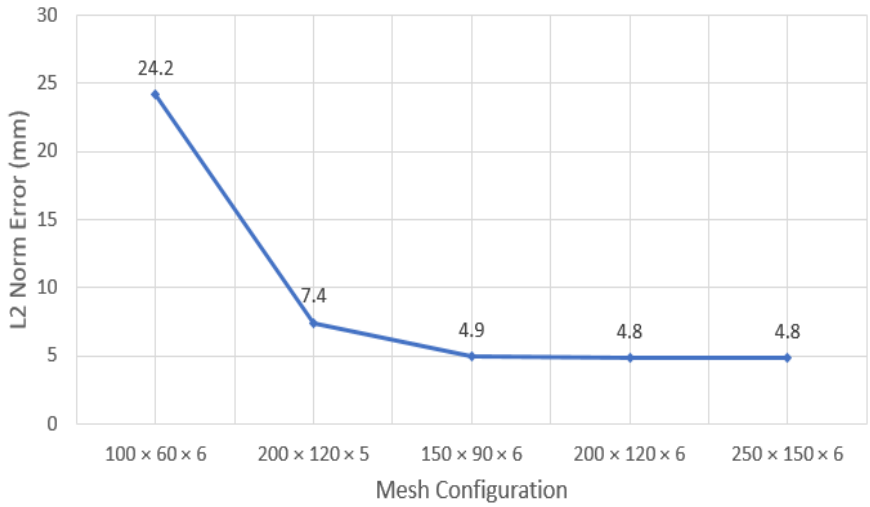

Figure 4.6 - L2 norm error for varying mesh configurations

The L2 norm error curve in Figure 4.6 indicates that the E_{L2} value tends to converge at the mesh arrangements of 200 × 120 × 6 and 250 × 150 × 6 where further mesh refinement does not show any significant reduction in the error. However, according to the E_{L2} value calculated for the 200 × 120 × 6 mesh arrangement, the total difference between the numerical and experimental results is approximately 5 mm. This error is to be attributed by the idealised boundary conditions and material properties. For example, pinned support conditions were used in the numerical models while performing mesh convergence study which do not perfectly match with the boundary conditions of the tested specimens. In addition, the behaviour of glass in the tensile region has not been fully understood yet. Nonetheless, the numerical model can predict the maximum dynamic deflection of the panel effectively.

After that, the validated FE model with the 200 × 120 × 6 mesh arrangement was modified by modelling the structural silicone sealant joints along the perimeter of the

panel instead of using pinned support conditions (see Figure 3.2). The material parameters in Section 3.3.3 were used while modelling silicone sealant joints in the present study. Figure 4.7 compares the deflection-time history curves at the geometric centre of the LG panel under pinned support conditions and with the perimeter silicone sealant joints. In Figure 4.7, the experimental curve exhibits a maximum centre deflection of 118 mm. With the silicone sealant joints, the panel shows a maximum centre deflection of 118.3 mm (representing a 0.25% difference compared to the experimental value), aligning precisely with the experimental results. Additionally, it shows that the LG panel with pinned support conditions approximately predicts the panel deflection for mid-impacts. However, it slightly overestimates the maximum centre deflection of the panel. Under the pinned support conditions, the maximum centre deflection is 121.9 mm (representing 3.31% difference compared to the experimental value). In Figure 4.7, the experimental curve exhibits a stiffer behaviour when contrasted with the numerical curves. This behaviour is attributed to the activation of the element deletion criterion and the use of idealised material models and boundary conditions in the numerical simulations.

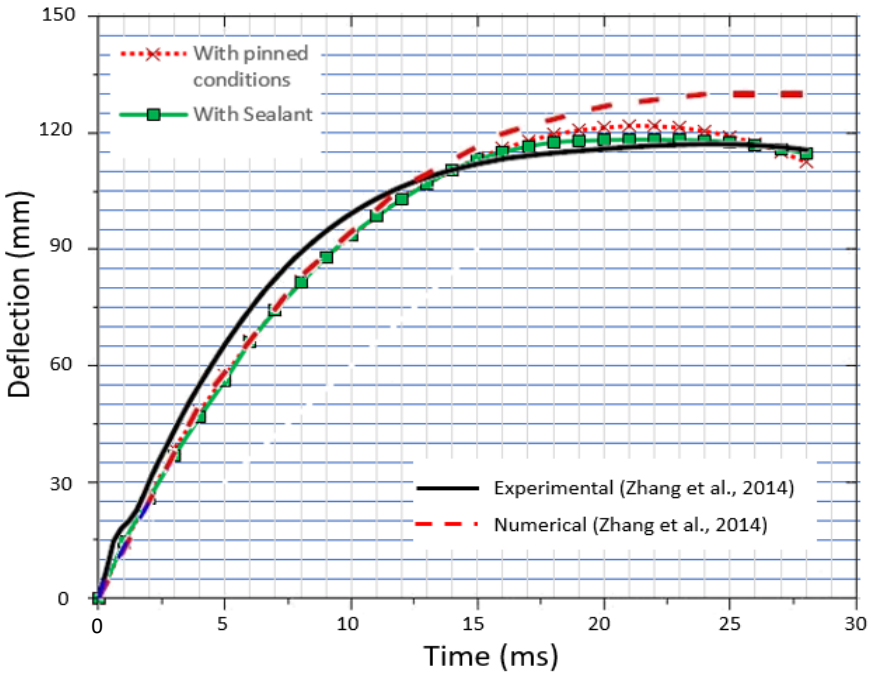

Figure 4.7 - Deflection-time history curve with the silicon sealant joints

4.4 Chapter Summary

This chapter presented the mesh convergence study and validation procedure of the numerical techniques used in this study. As it was explained in Section 4.2, nine different mesh configurations were considered while conducting the mesh convergence study by changing the in-plane and through-thickness dimensions of the 3D constant stress solid elements in the FE models developed to simulate the mid-impacts. While conducting the mesh convergence study, pinned support conditions

were used in the FE models. A detailed explanation of the behaviour of the LG panel under different mesh configurations has been included in this chapter. After conducting a mesh convergence study, the mesh configuration with 200 × 120 × 6 elements was selected as a better configuration for the analysis.

The FE model with the 200 × 120 × 6 mesh configuration was validated by comparing the numerical central deflection-time history curves with the results of a previous experiment. In addition, the accuracy of the selected mesh configuration was evaluated using the L2 norm error method. It was found that the total difference between the numerical and experimental central deflection-time history curve is about 5 mm, which was attributed by the idealised material models and boundary conditions used in the numerical model. Nonetheless, it was revealed that the FE model can effectively capture the behaviour of the LG window panel under windborne debris impact. After modifying the support conditions of the panel by modelling the perimeter sealant joints, the numerical results further precisely aligned with the experimental results.

CHAPTER 5

RESPONSE OF LAMINATED GLASS (LG) PANEL SUBJECTED TO MID-IMPACT

5.1 Introduction

After validating the numerical modelling techniques, the validated numerical models were used to understand the impact behaviour of the LG panel. Firstly, the response of the LG panel to impact at the geometric centre of the panel (mid-impact) was investigated and the findings are presented in this section. At the beginning of this chapter, the effect of different support conditions on the behaviour of LG panels is discussed in Section 5.2. Then, the impact performance of the LG window panel is examined considering the energy absorption of different parts of the window panel, and stress variation of the materials in Sections 5.3, and 5.4 respectively. The effect of glass thickness on the impact performance of the LG panel is discussed in Section 5.5.

5.2 Effect of Support Condition on Impact Behaviour of Laminated Glass (LG) Panel

The effect of support conditions on behaviour of the LG panel was investigated by considering three different support conditions: (i) pinned supports; (ii) fixed supports; and (iii) structural silicone sealant joints along the perimeter of the glass panel. Figure 5.1 shows the dynamic deflection curves at the centre of the panel for mid-impacts under the different support conditions stated above.

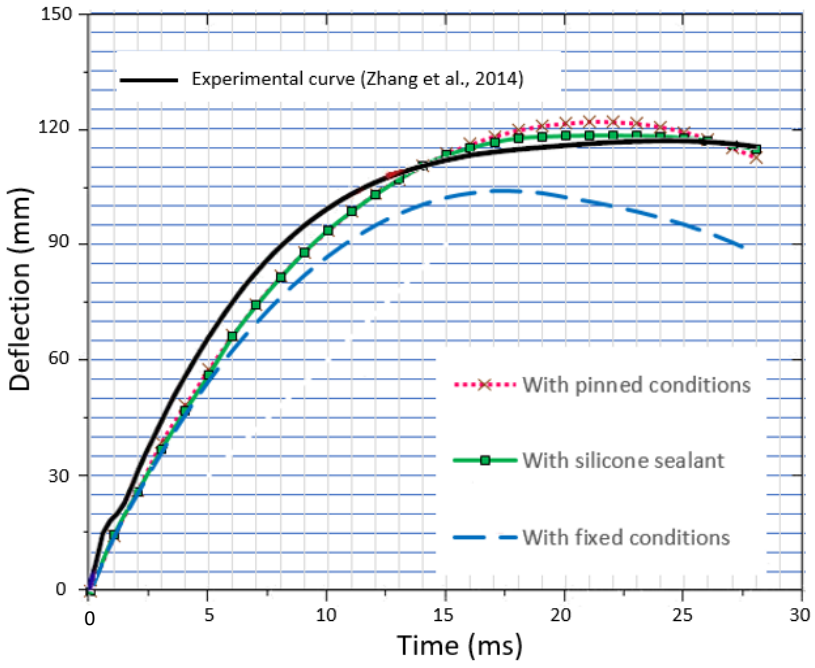

Figure 5.1 - Deflection-time history curves under different support conditions

The centre deflection of the panel with fixed support conditions is notably lower than those of the panels with pinned support conditions and sealant joints (see Figure 5.1). Pinned support condition allows for rotation at the supports whereas fixed supports restrict rotations providing some rigidity to the system. As a result, the fixed supports limit the overall deflection of the panel. On the other hand, sealant joints provide some freedom to deform (more freedom than fixed support, but less freedom than pinned support) at the perimeter of the panel, leading to increased deflection values that align with the experimental values (see Figure 5.1). Therefore, it is evident that the behaviour of the LG panel with sealant joints lies between pinned and fixed conditions under the applied load.

5.3 Energy Absorption

The energy absorption of different parts of the LG panel is discussed in this section. Figure 5.2 compares the total energy absorption of the different parts of the LG panel for mid-impacts for 35 ms.

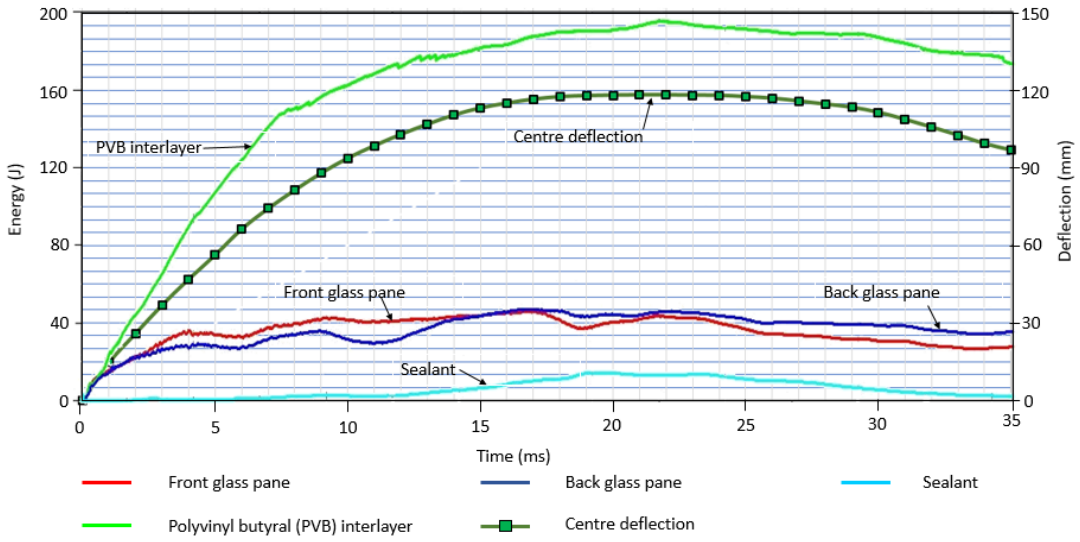

Figure 5.2 - Energy absorption of different parts of the LG panel

For the selected impact phenomenon, the front glass pane, back glass pane, and PVB interlayer initially absorb energy. The initial energy absorption rate of PVB interlayer is comparatively higher than those of glass panes and sealant material. PVB interlayer reaches the maximum value of 194 J at 22 ms when the panel reaches its maximum centre deflection value of 118 mm. Then the energy absorption of the PVB interlayer gradually decreases and reaches 173 J at 35 ms. Both the front glass pane and the back glass pane exhibit similar energy absorption patterns, with identical energy absorption values up to 2 ms. From 2 ms to 16 ms, the front glass pane shows slightly higher energy absorption than that of the back glass pane because wooden debris directly hits the front glass pane during this period. After 16 ms, the back glass pane demonstrates slightly higher energy absorption compared to the front glass pane up to 35 ms, when the panel reaches higher deflection values. The maximum energy absorption of both

glass panes is about 47 J at 17 ms and 22 ms. Since the impact location is far away from the sealant joints for mid-impacts, sealant joints do not exhibit significant energy absorption up to 5 ms. However, after 5 ms, sealant material absorbs more energy as the waves generated by the sudden impact phenomenon propagate over the LG panel towards the sealant joints and also due to increase in the deflection of the LG panel which apply additional in-plane stress on the sealant joints. The sealant material attains its maximum energy absorption value of about 14 J at 19 ms and maintains it until 24 ms. After that, the energy absorption of sealant material gradually decreases to 3 J. Therefore, it is evident for the mid-impacts that the PVB interlayer film plays a dominant role in resisting sudden impact loads by absorbing a significant amount of energy compared to the glass and sealant joints.

5.4 Stress Variation and Material Failure

The likelihood of material failure was examined by analysing the stress variation of glass, PVB, and sealant materials, and the results are presented in this section. The failure criteria explained in Section 2.7 were considered to identify the material failure in this study.

Usually, principal stresses are used to define the failure criterion of glass (Hidallana-Gamage et al., 2014). In the present study, the failure criterion of glass is defined considering the maximum stress component (i.e. 1st principal stress (σ_{11})). The glass panes in this study are considered to be failed, when σ_{11} exceeds the dynamic breaking strength (T_b) of annealed glass which is approximately 80 MPa (Cormie et al., 2009; Hidallana-Gamage et al., 2014). Both the PVB and silicon sealant materials exhibit a ductile behaviour. Consequently, the PVB and sealant material in this study are considered to be failed, when Von Mises stress (σ_v) exceeds the yield stress (σ_y) of the material (Hidallana-Gamage et al., 2014). The yield stress of PVB and silicon sealant considered in the present study are about 11.41 MPa and 2.3 MPa respectively (Hidallana-Gamage, 2015; Nawar et al., 2021). Figure 5.3 and Figure 5.4 illustrate the variation of the 1st principal stress of the front and back glass panes respectively at 0.3ms and 4.6 ms. Figure 5.3 (a) and Figure 5.4 (a) show that the 1st principal stress exceeds the dynamic breaking strength of glass (i.e. 80 MPa) at the impact location at 0.3 ms. As a result, glass cracking starts at the debris impact zone of the panel. As the stress waves propagate through the LG panel, cracks on the glass panes spread radially towards the panel boundary (see Figure 5.3 (b) and Figure 5.4 (b)). However, crack density gradually decreases towards the boundary of the panel. Figure 5.5 shows the variation of Von Mises stresses in the PVB interlayer. For the selected impact, the Von Mises stress at the impact location exceeds the yield stress of PVB material (i.e. 11.41 MPa), which indicates that the likelihood of PVB failing at the impact location is increased (see Figure 5.5 (a) and Figure 5.5 (b)). Therefore, it is evident that even though the PVB interlayer has slightly failed at the debris impact zone, it can absorb energy to resist penetration until its complete failure. The variation of Von Mises stress in the perimeter silicon sealant joints is illustrated in Figure 5.6. Figure 5.6 (a)

illustrates that the Von Mises stress in sealant joints initially shows higher values at the mid-span region of the longest edge under the mid-impact as the shock waves reach the sealant joints after the impact. After that, stress waves propagate towards the corners of the panel through the sealant joints (see Figure 5.6 (b)).

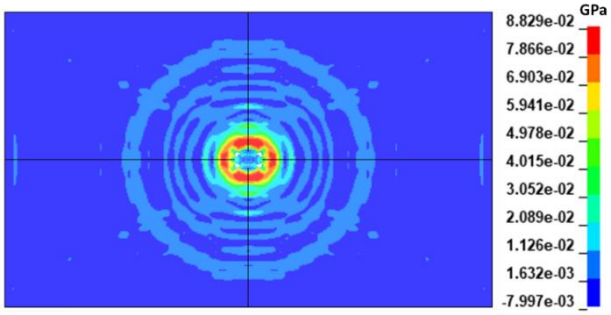

(a) At t = 0.3 ms

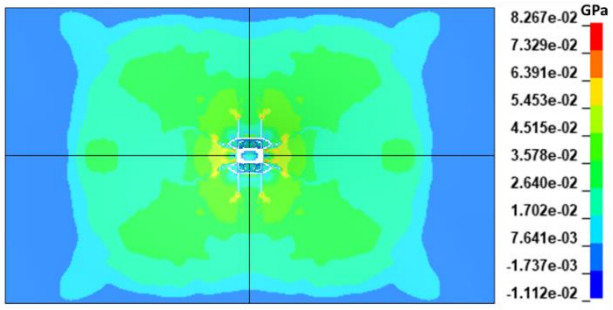

(b) At t = 4.6 ms

Figure 5.3 - Variation of 1st principal stress on the top surface of the front glass pane

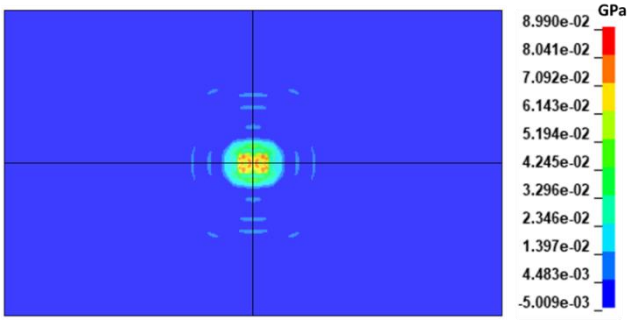

(a) At t = 0.3 ms

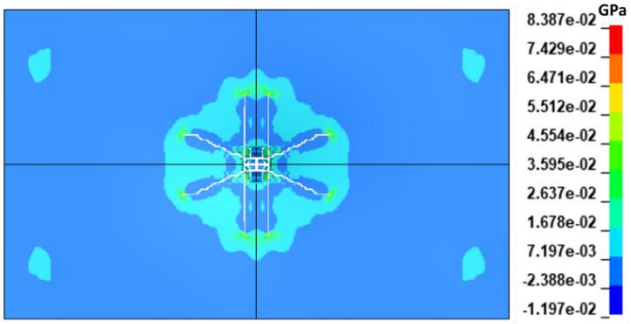

(b) At t = 4.6 ms

Figure 5.4 - Variation of 1st principal stress on the inner surface of the back glass pane

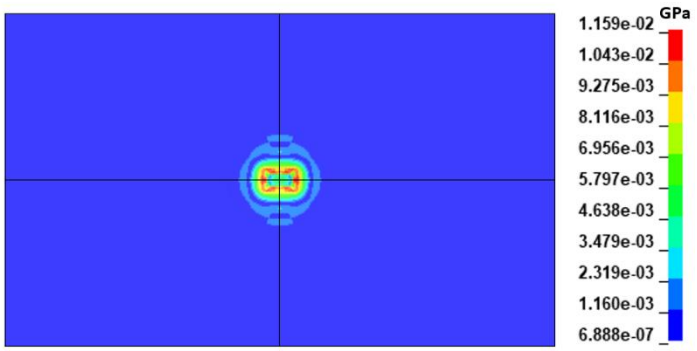

(a) At t = 0.3 ms

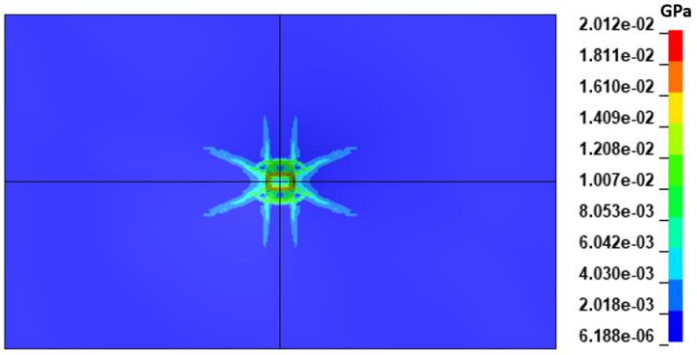

(b) At t = 4.6 ms

Figure 5.5 - Variation of Von Mises stress in the PVB interlayer

(a) At t = 0.3 ms

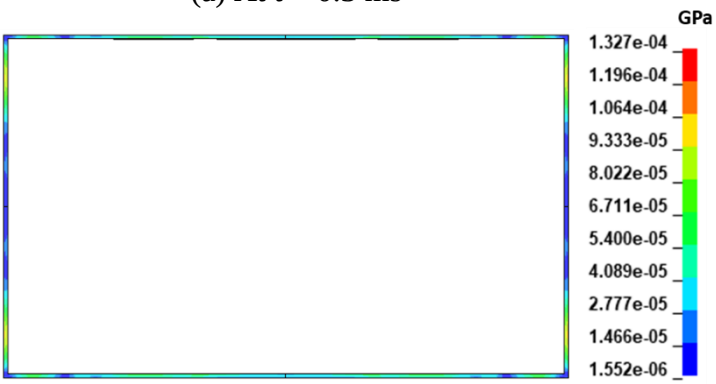

(b) At t = 4.6 ms

Figure 5.6 - Variation of Von Mises stress in the silicone sealant joints

Therefore, when the debris impact location is distant from the perimeter sealant joints of the panel, the likelihood of sealant failing is reduced. However, further research is necessary to examine the behaviour of perimeter sealant joints when the LG panels are subjected to impacts near the sealant joints. Therefore, the behaviour of different parts of the LG panel when subjected to impact at various critical locations of the panel is investigated in Chapter 6.

5.5 Effect of Glass Thickness on the Impact Performance

This section discusses the effect of glass thickness of the LG panel on its impact performance. Firstly, the PVB interlayer was replaced with a thin glass pane that has a thickness of 1.88 mm and the total energy absorption of the different parts of the window panel was assessed. Subsequently, the study was extended to investigate the effect of glass thickness on the impact performance of the LG panel when incorporating the PVB interlayer. This study considered three different glass thicknesses: 3 mm; 5 mm; 8 mm. Figure 5.7 illustrates the aforementioned four cases considered in this study.

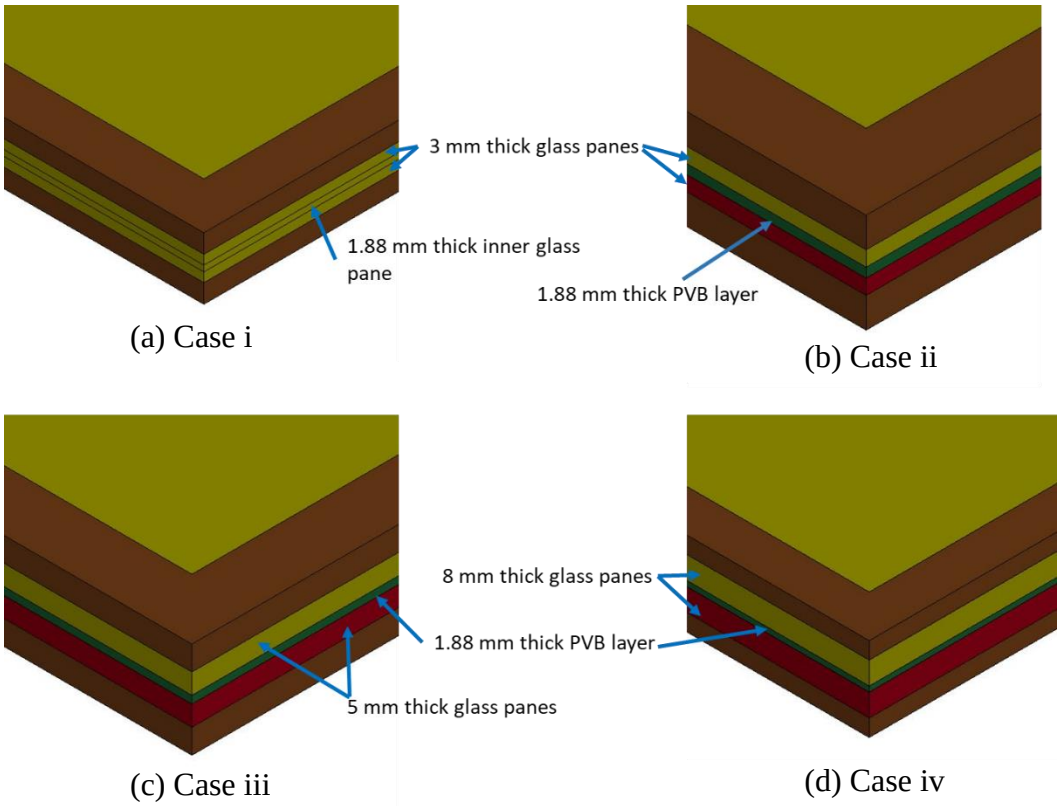

(a) Case i (b) Case ii

(c) Case iii (d) Case iv

Figure 5.7 - Four cases considered in the study

Figure 5.8 demonstrates the energy absorption of the different parts of the window panel when the PVB interlayer is replaced with a 1.88 mm thick glass pane (case i). Figure 5.9 depicts the variation in the maximum dynamic deflection and total energy of the panel under the same conditions.

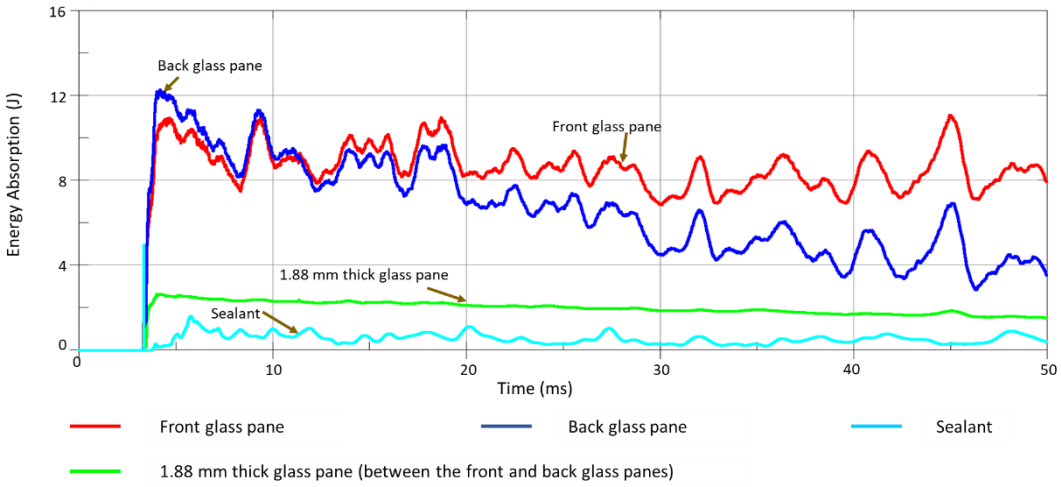

Figure 5.8 - Variation of the energy absorption (case i)

Figures 5.8 and 5.9 demonstrate that the window panel exhibits notably low energy absorption and dynamic deflection when the PVB interlayer is replaced with a thin glass pane. As the window panel experiences low deflection values, the energy and the load transferred to the sealant joints are relatively minimal. Hence, it is evident that an annealed glass panel offers minimal resistance to the sudden impact loads.

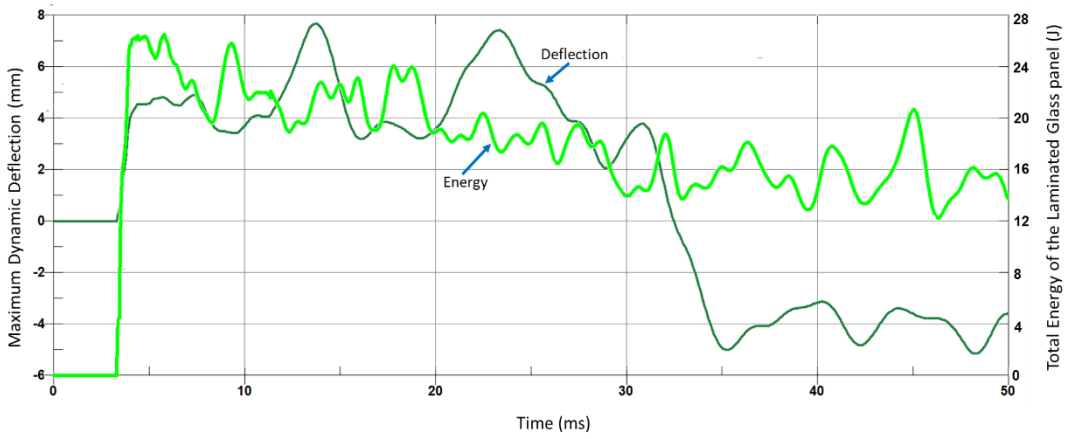

Figure 5.9 – Variation of the maximum dynamic deflection and total energy of the window panel (case i)

Figure 5.10 illustrates the energy absorption of the various components of the LG panel shown in Figure 3.2, designated as case ii in this section. Figure 5.11 depicts the variation of the maximum dynamic deflection and total energy of the same panel. Figures 5.12 and 5.14 show the energy absorption of the individual components of the LG panel when it incorporates 5 mm thick glass panes (case iii) and 8 mm thick glass panes (case iv), respectively. Meanwhile, Figures 5.13 and 5.15 showcase the variation in the maximum dynamic deflection and total energy of the panel for cases iii and iv, respectively.

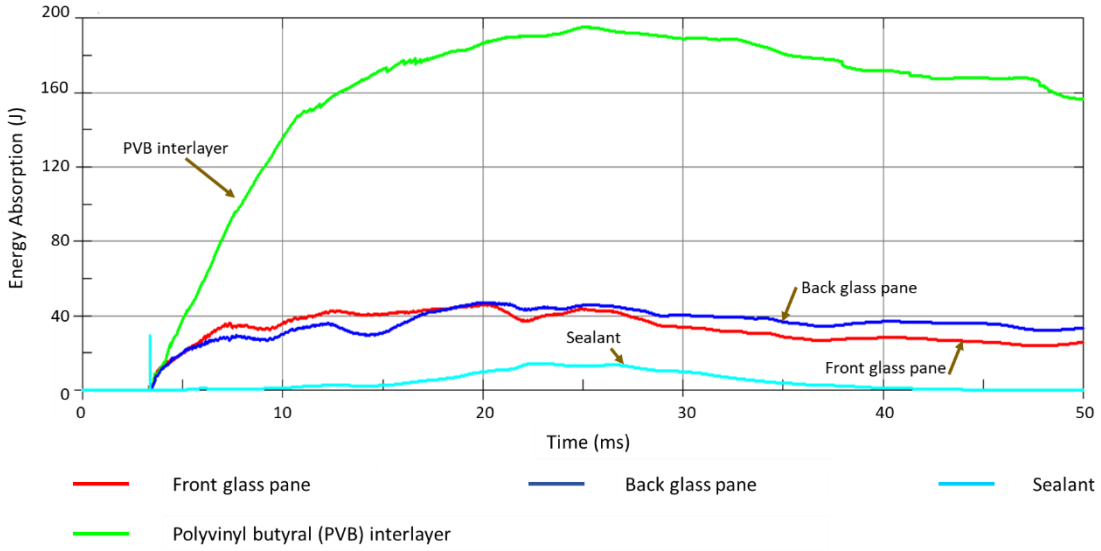

Figure 5.10 - Variation of the energy absorption (case ii)

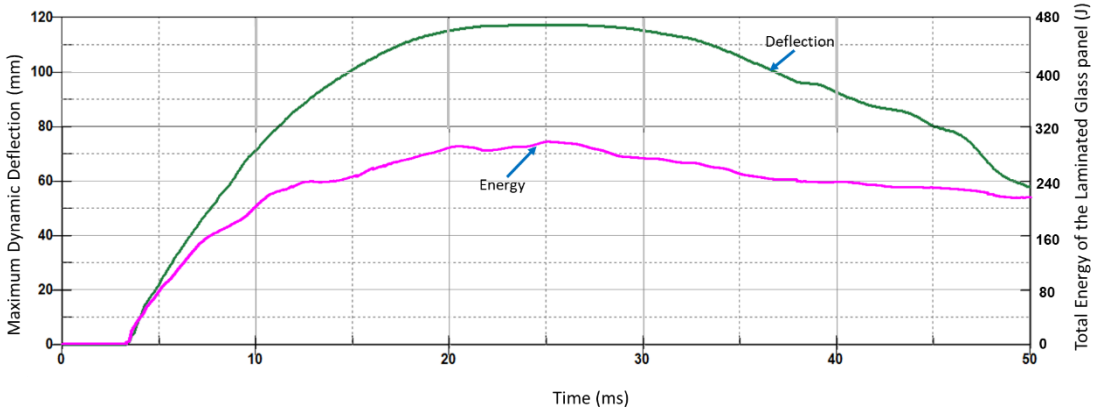

Figure 5.11 - Variation of the maximum dynamic deflection of the LG panel (case ii)

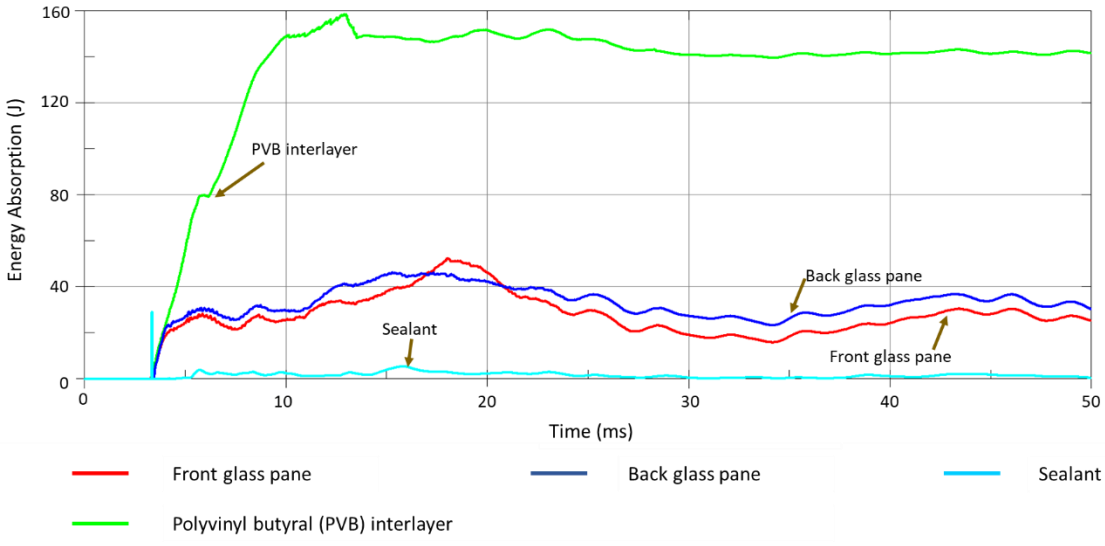

Figure 5.12 - Variation of the energy absorption (case iii)

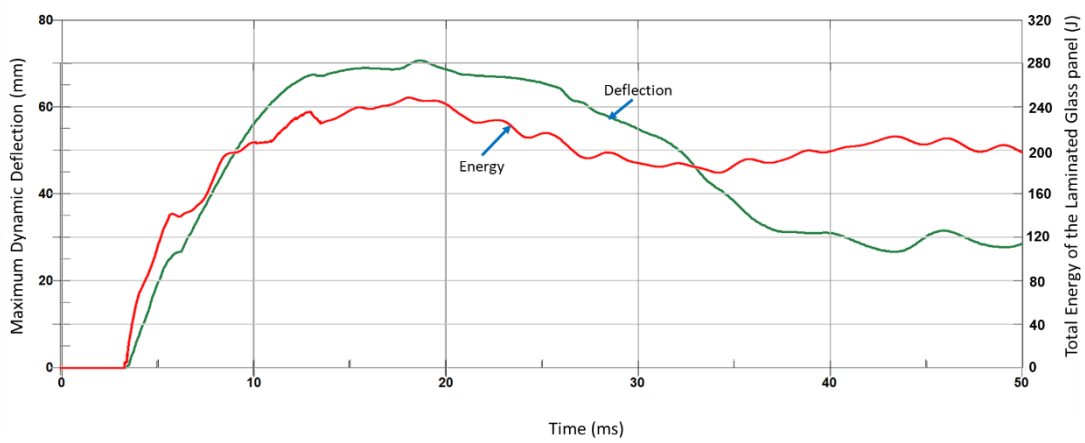

Figure 5.13 - Variation of the maximum dynamic deflection of the LG panel (case iii)

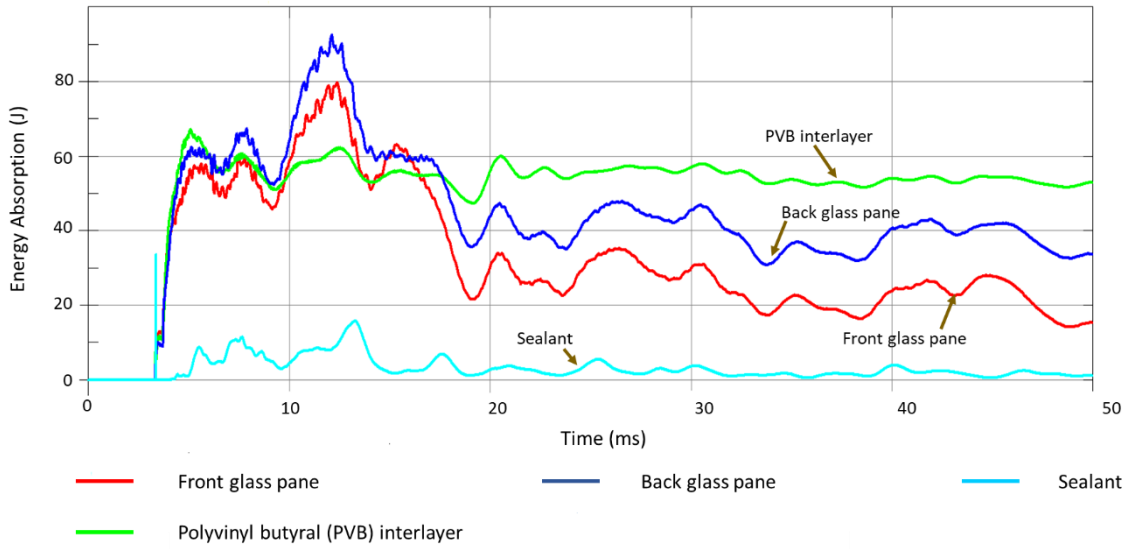

Figure 5.14 - Variation of the energy absorption (case iv)

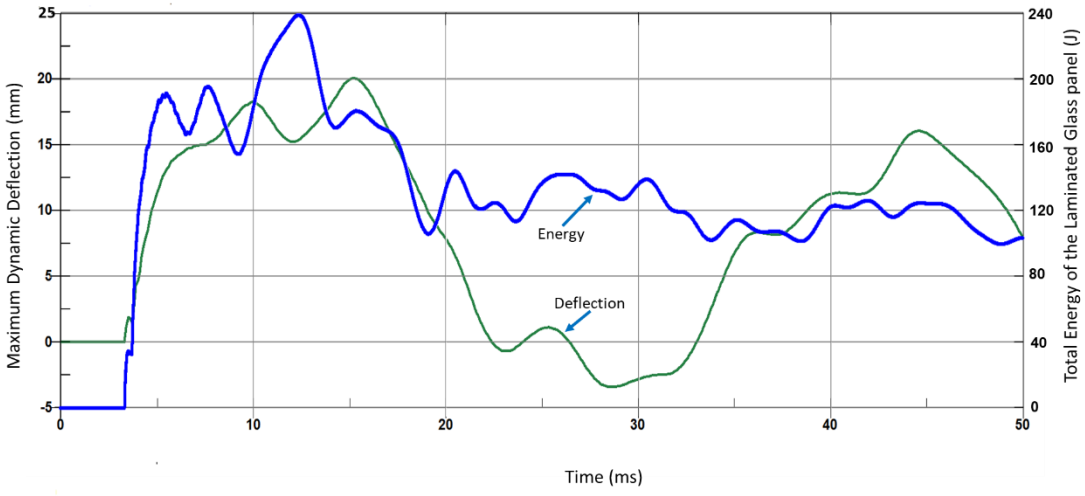

Figure 5.15 - Variation of the maximum dynamic deflection of the LG panel (case iv)

In Figures 5.9, 5.11, 5.13, and 5.15, it is evident that the LG panel achieves the highest total energy when it experiences the maximum dynamic deflection during the impact event.

Figure 5.16 presents a comparison of the total energy variations respectively for each respective case.

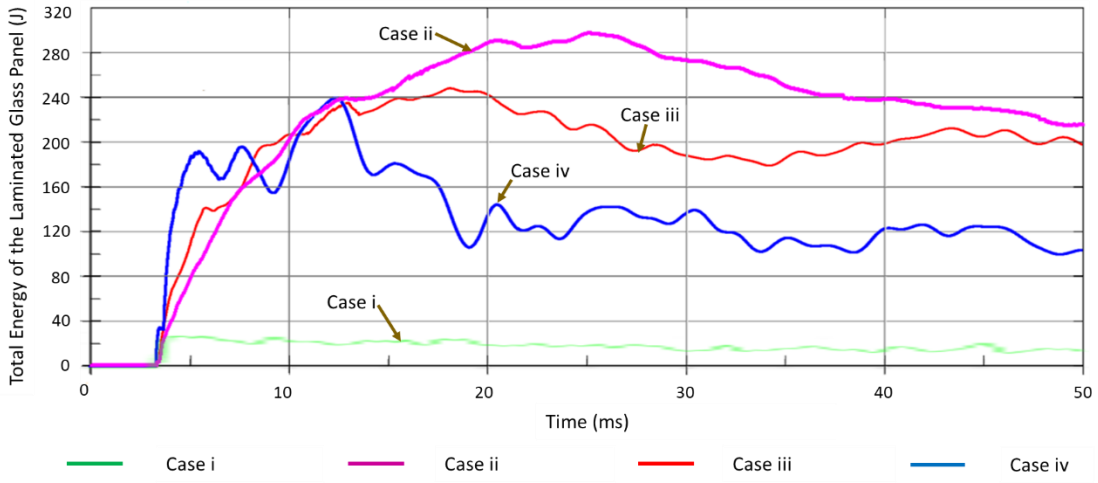

Figure 5.16 – Variation of total energy of the LG panel

Figure 5.16 demonstrates that the energy absorption of the PVB interlayer decreases as the glass thickness increases. This variation arises due to the diminished panel deflections observed in the LG panel with increasing the glass thickness (see Figures 5.11, 5.13, and 5.15). In case iv, the maximum energy absorption of the front glass pane (i.e. 80 J) and the back glass pane (i.e. 94 J) exceeds that of the PVB interlayer (i.e. 68 J). In addition, the energy absorption of both glass panes tends to increase with greater glass thickness. It is observed that the energy absorption of the perimeter sealant joints increases as the glass thickness increases. It occurs due to the stiff behaviour introduced by the thicker glass panes. Consequently, the load transferred to the sealant joints increases as the glass thickness increases, leading to a notable energy absorption within the sealant joints. Case ii represents the optimal layer configuration among four cases discussed in this section.

Therefore, it is worth mentioning that enhancing the impact performance of the LG panel cannot be achieved solely by adding thicker glass panes to the LG window panels without a well-thought-out design. The most effective strategy in impact-resistant glazing is to design the LG window panel as a sacrificial element, allowing it to fail by tearing the interlayer after absorbing a greater amount of impact energy.

5.6 Chapter Summary

The response of LG panel subjected to the impact that hit the geometric centre of the panel (mid-impacts) was investigated in this chapter.

The effect of the support condition of the panel on its impact behaviour was examined by using FE models. It was found that the behaviour of the LG panel with perimeter silicone sealant joints exhibits a behaviour that lies between pinned and fixed conditions when the panel is subjected to the same impact loads. However, it was noted that the LG panel with pinned support conditions can approximately capture the test results under the mid-impacts. By analysing the energy absorption of the different components of the LG panel subjected to mid-impacts, it was found that the PVB interlayer plays a dominant role in resisting sudden impact loads and avoiding penetrations by effectively absorbing a greater amount of impact energy compared to glass, and silicon sealant. While examining the material failure, the stress variation of materials was analysed. The annealed glass panes were considered to be failed when the maximum stress component of glass (σ_{11}) exceeds its dynamic breaking strength (T_b) which is about 80 MPa (Cormie et al., 2009; Hidallana-Gamage et al., 2014). Meanwhile, the PVB and silicone sealant materials were considered to be failed when the Von Mises stress (σ_v) exceeds the yield stress (σ_y) of the material (Hidallana-Gamage et al., 2014). The yield stress of PVB and silicone sealant materials were considered as 11.41 MPa and 2.3 MPa respectively (Hidallana-Gamage, 2015; Nawar et al., 2021). It was found that for mid-impacts, the cracks start at the debris impact zone after hitting the debris on the panel. Afterwards, cracks spread in radial directions towards the perimeter boundary of the panel. It was also noticed that the crack density gradually reduces away from the impact zone as cracks spread. In addition, it was observed that the likelihood of PVB failure is higher at the debris impact zone compared to the other locations of the panel. It is worth noting that the PVB interlayer can prevent penetrations until its complete failure even though it slightly fails at the debris impact region. It is evident from the simulation results that the likelihood of silicone sealant failure is reduced when the panel is subjected to impacts that strike away from the perimeter sealant joints. However, it was identified that further research is necessary to investigate the response of LG panels and silicone sealant joints when subjected to impacts near the perimeter boundary.

Furthermore, this section discussed the effect of glass thickness of the LG panel on its impact performance. It was found that the PVB interlayer plays a pivotal role in impact resistance by absorbing a significant amount of impact energy. The LG panel achieves the highest total energy when it experiences the maximum dynamic deflection. It was observed that the energy absorption of the perimeter sealant joints increases as the glass thickness increases. Upon a comprehensive analysis, it was identified that the most optimal approach for impact-resistant glazing is to design the LG window panel as a sacrificial element, permitting it to fail after absorbing a greater amount of impact energy.

The response of the LG panel and the silicone sealant joints subjected to impacts at the ASTM specified critical impact locations is discussed in Chapter 6.

CHAPTER 6

RESPONSE OF LAMINATED GLASS (LG) PANEL SUBJECTED TO IMPACTS AT VARIOUS IMPACT LOCATIONS

6.1 Introduction

After investigating the behaviour of LG panels subjected to mid-impacts, it was realised that it is worth examining their response under the impacts that strike the panel at different impact locations. As discussed previously in Section 2.4, ASTM specified critical impact locations were considered in this study. In addition, the findings from the comprehensive literature review were considered to identify the critical impact locations. Firstly, a mesh convergence study was conducted by using validated FE models to identify the optimum mesh configurations of the FE models and it is illustrated in Section 6.2. Consequently, the identified optimum mesh configuration was used in the study. The energy absorption of different parts of the window panel, and stress variation of the materials were analysed while investigating the impact performance of the LG window panel in this Chapter. The behaviour of the panel was analysed at different impact locations: corner of the panel; long-span mid; and short-span mid, and results are presented in Sections 6.3, 6.4, and 6.5 respectively.

6.2 Mesh Convergence Study

This section presents the details of the extensive mesh convergence study conducted in this study. The same window panel and impact loadings presented in Chapter 3 were considered in this study to investigate its response under different impact locations. While developing the FE models to simulate the impact strike at the different impact locations of the panel, the entire panel was modelled with the perimeter silicone sealant joints. Figure 6.1 shows the different impact locations of the panel considered in the present study.

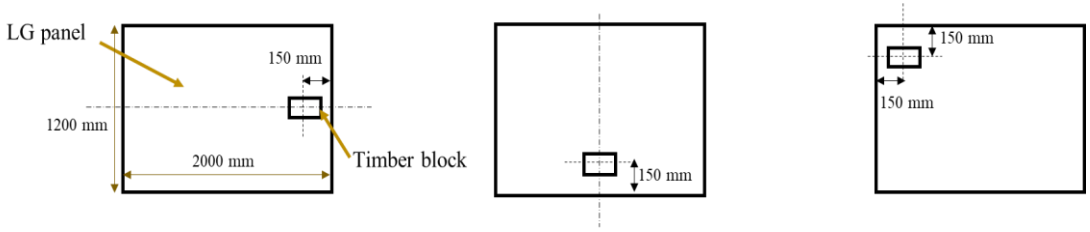

(a) Short-span mid (b) Long-span mid (c) Corner

Figure 6.1 - Different impact locations considered in the study

While conducting the mesh convergence study, three different mesh configurations were considered. They are: (300 × 180 × 6); (400 × 240 × 6); and (500 × 300 × 6). The notation used here to denote the mesh configurations was explained previously in

Section 4.2. Two of these mesh configurations (i.e. 300 × 180 × 6, and 400 × 240 × 6) were selected based on the mesh convergence study results obtained from mid-impacts. In addition, a finer mesh configuration (i.e. 500 × 300 × 6) compared to the optimum mesh configuration used under mid-impacts (see Section 4.2) was also considered. As it was noted previously, here the entire panel was modelled. Therefore, the element sizes of the mesh configurations of 300 × 180 × 6, and 400 × 240 × 6 are similar to the element sizes of the 150 × 90 × 6, and 200 × 120 × 6 configurations respectively (see Section 4.2).

The maximum dynamic deflection-time history curves of the back glass pane of the panel were examined while conducting the mesh convergence study. Figures 6.2, 6.3, and 6.4 illustrate the variation of the maximum dynamic deflection of the back glass pane concerning distinct impact locations: corner; long-span mid; and short-span mid of the panel respectively.

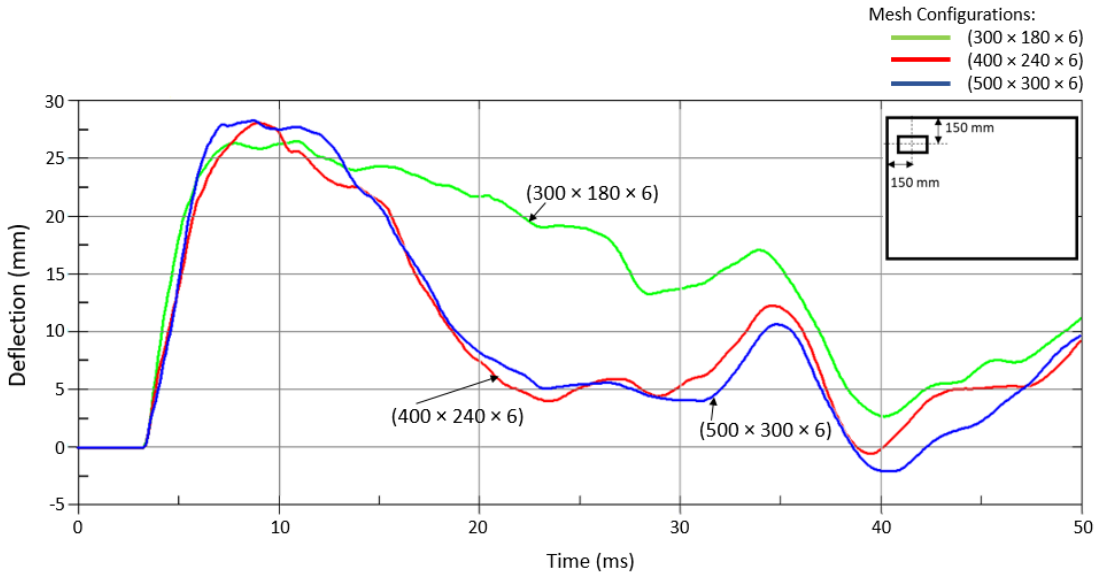

Figure 6.2 - Variation of maximum dynamic deflection of the panel subjected to corner impact

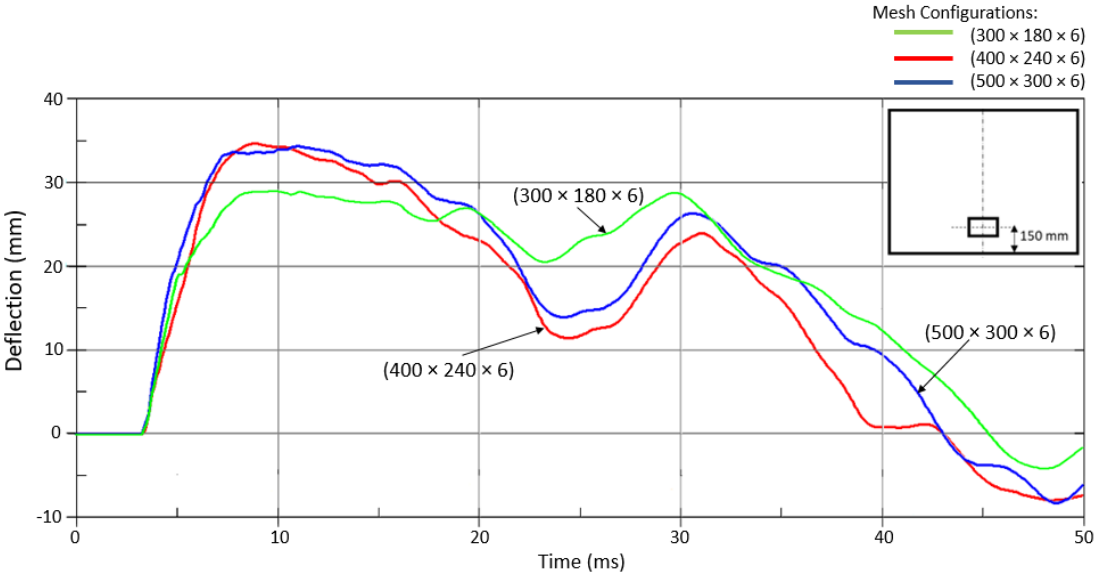

Figure 6.3 - Variation of maximum dynamic deflection of the panel subjected to long-span mid-impact

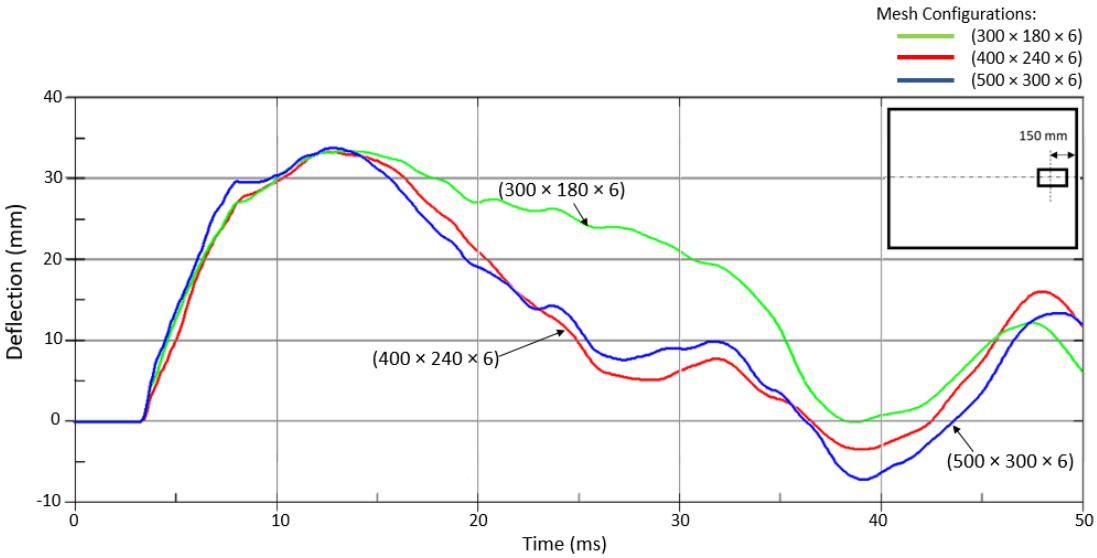

Figure 6.4 - Variation of maximum dynamic deflection of the panel subjected to short-span mid-impact

By thoroughly examining the deflection-time history curves depicted in Figures 6.2, 6.3, and 6.4, an obvious convergence of the FE results becomes evident at the finer mesh configuration of 500 × 300 × 6. Furthermore, it was observed that further mesh refinement beyond the aforementioned mesh configuration of 500 × 300 × 6 does not depict a significant improvement in the results.

In addition, the peak values of the maximum dynamic deflection-time history curves were also compared concerning distinct mesh configurations, and the outcomes are presented in Figures 6.5, 6.6, and 6.7.

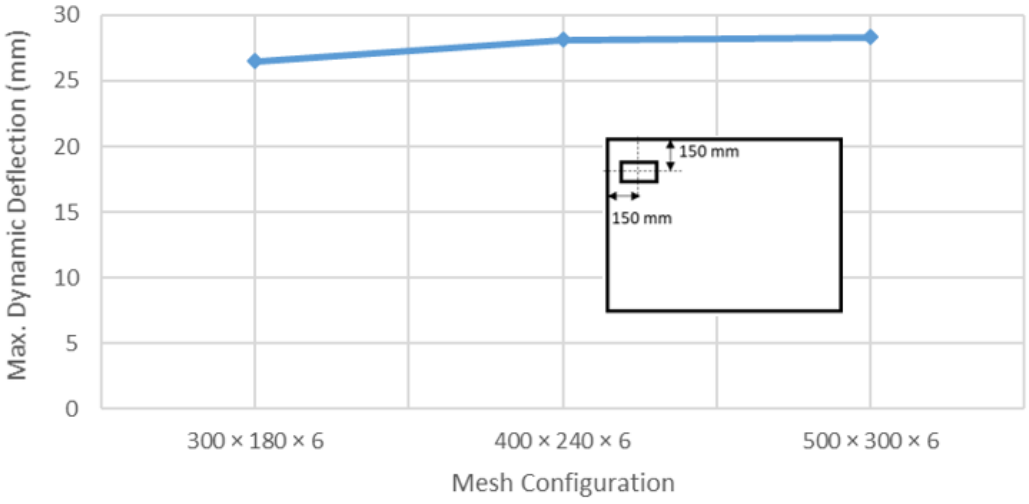

Figure 6.5 - Variation of the peak value of the maximum dynamic deflection for varying mesh configurations (corner impact)

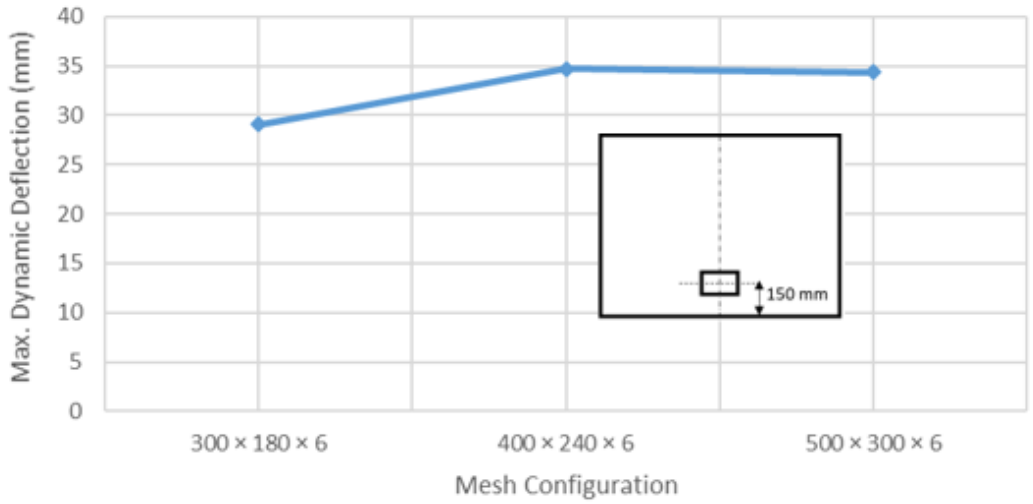

Figure 6.6 - Variation of the peak value of the maximum dynamic deflection for varying mesh configurations (long-span mid-impact)

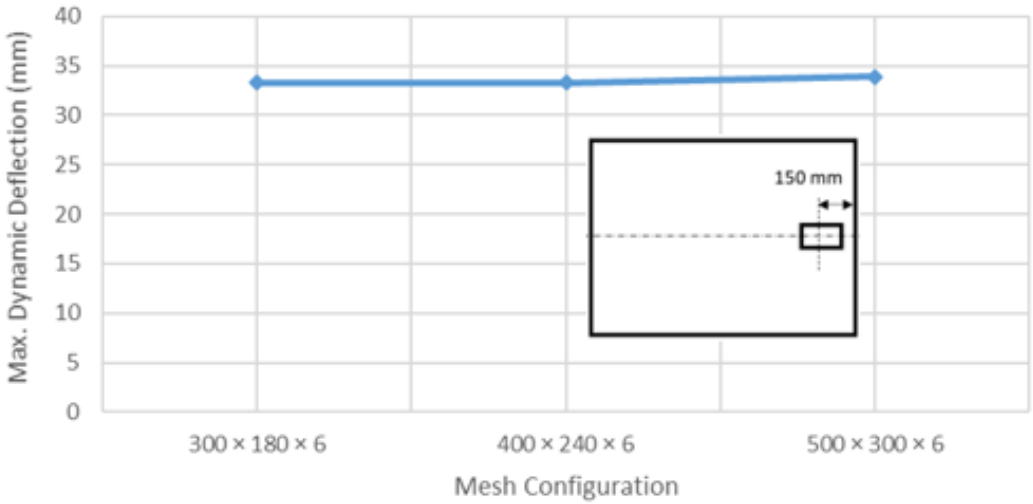

Figure 6.7 - Variation of the peak value of the maximum dynamic deflection for varying mesh configurations (short-span mid-impact)

Upon a comprehensive analysis of the deflection results shown in Figures 6.5, 6.6, and 6.7, a convergence of the outcomes becomes apparent at the mesh configuration of 500 × 300 × 6. It should be noted that further refinement of the element sizes will not show a significant enhancement in the results.

Figures 6.8, 6.9, and 6.10 illustrate the total energy variation of the LG panel under corner impacts, long-span mid-impact, and short-span mid-impact, respectively for varying mesh configurations.

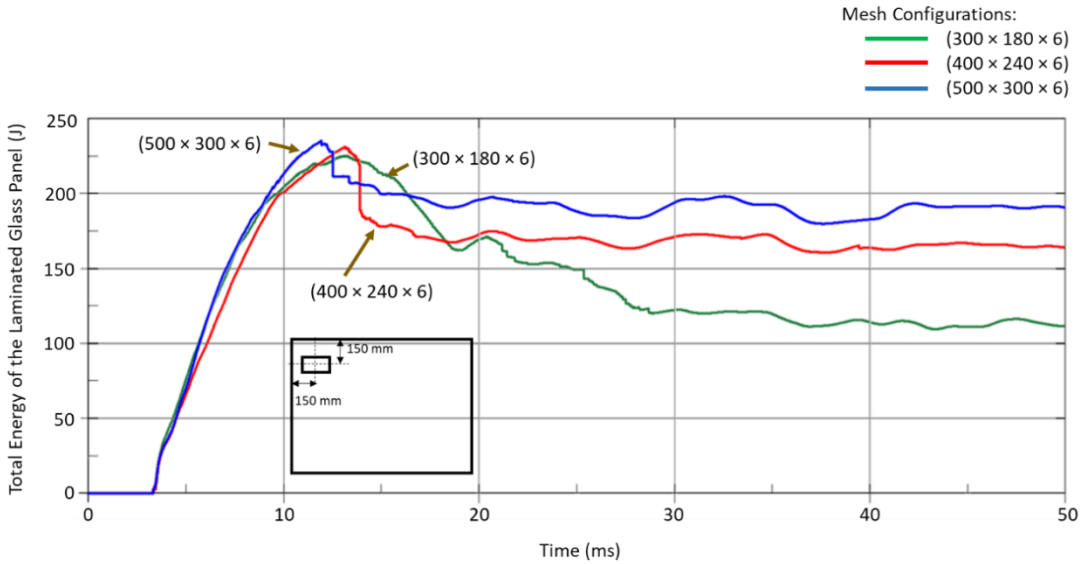

Figure 6.8 - Total energy variation of the LG panel (corner impact)

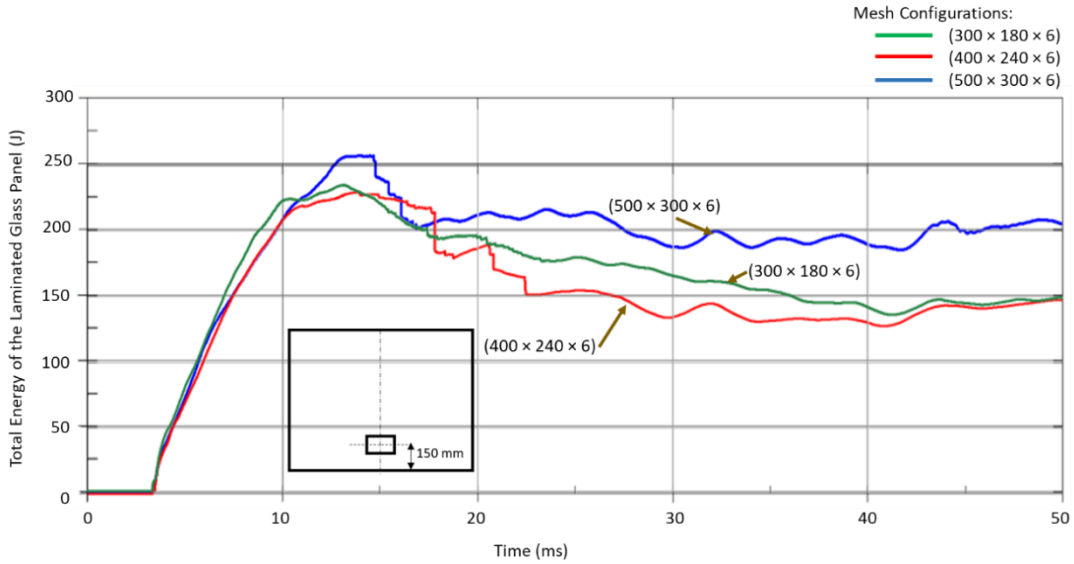

Figure 6.9 - Total energy variation of the LG panel (long-span mid-impact)

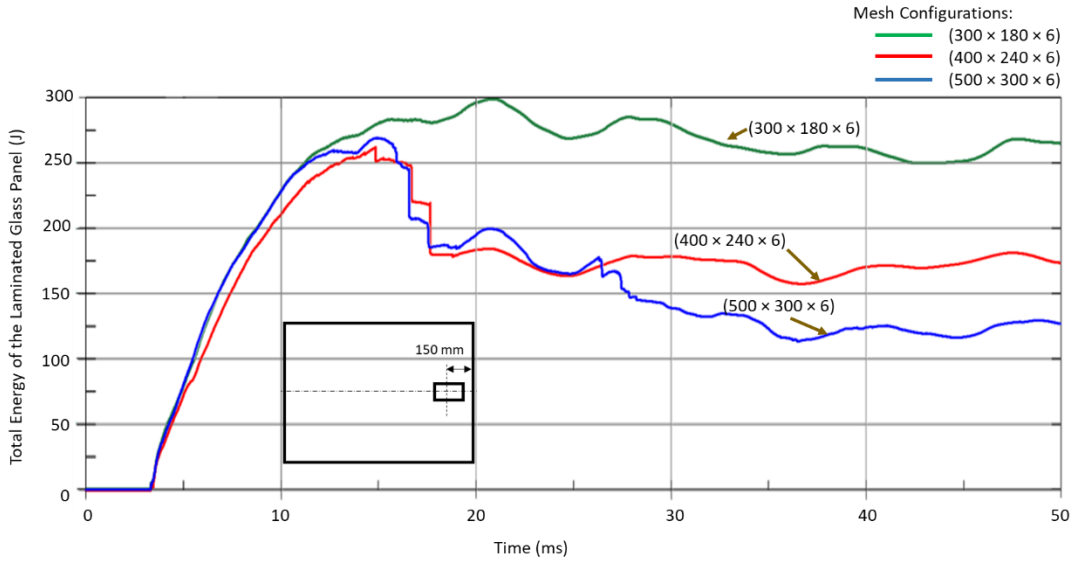

Figure 6.10 - Total energy variation of the LG panel (short-span mid-impact)

Figures 6.8, 6.9, and 6.10 demonstrate that the total energy of the LG panel exhibits consistent trends when using mesh configurations of 400 × 240 × 6 and 500 × 300 × 6. Therefore, the mesh arrangement of 500 × 300 × 6 was used to study the response of the panel concerning aforementioned impact locations.

6.3 Variation of Maximum Dynamic Deflection of the Panel

The variation of maximum dynamic deflection of the back glass pane of the window panel is discussed in this section. The dynamic deflection curves of the back glass pane from 0 ms to 50 ms are compared concerning the different impact locations, and curves are illustrated in Figure 6.11. The wooden debris hits the panel at 3.3 ms in these simulations.

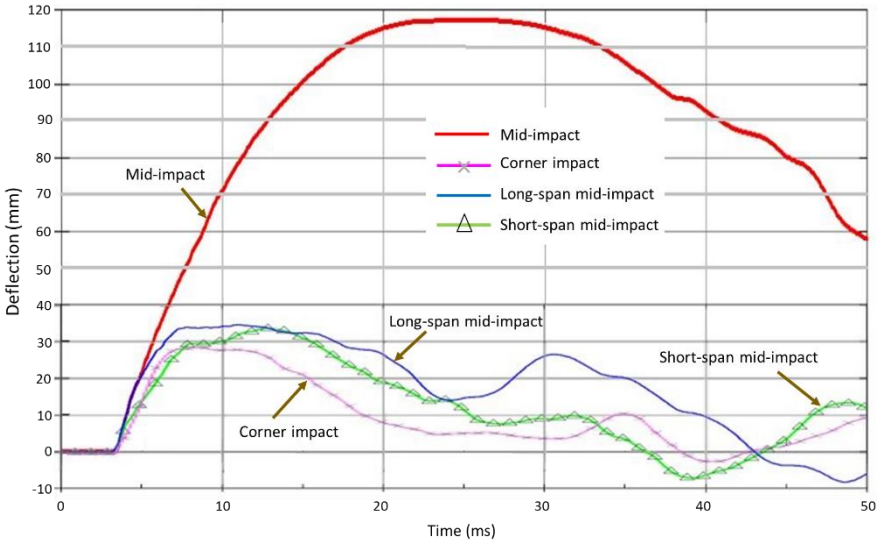

Figure 6.11 - Variation of maximum dynamic deflection of the back glass pane

Figure 6.11 demonstrates that the peak value of the maximum dynamic deflection under corner impact is about 28.3 mm, which is slightly lower than that of long-span and short-span mid-impacts. The panels subjected to long-span mid-impact and short-span mid-impact show peak values of 34.4 mm and 33.9 mm respectively. However, when debris hits the geometric centre of the panel, the maximum dynamic deflection is about 118 mm. Therefore, it is evident that the perimeter support conditions along the two edges of the panel limit the ability to deform. The long-span and short-span mid-impact cases have slightly higher maximum deflection values compared to the corner impact case. Because in these two cases, the glass panel has comparatively more freedom to deform than that in corner impact case. Figure 6.12 illustrates the penetration status of the LG panel in the four cases considered in this study. It was observed that the panel has been penetrated by the wooden debris when subjected to corner, long-span, and short-span mid-impacts. However, under the same impact loading, the panel was not penetrated by debris when it hit the geometric centre of the panel (see Figure 6.12). Therefore, it is noticeable that the penetration vulnerability is comparatively higher when debris hits the region near the window frame. This

occurrence arises due to the limited deformations of the panel imposed by the support constraints near the impact locations. In addition, up to 43 ms, the panel subjected to long-span mid-impact shows higher deflections than that of the corner impact and short-span mid-impact cases. Figure 6.11 illustrates that following the 1st peak deflection, the dynamic deflection reduces with time. However, it is evident that before coming back to the original position of the panel, the deflection tends to increase again up to its 2nd peak because of the influence of the reflected shock waves. After the 2nd peak, the deflection gradually decreases and returns to the original position. Upon a comprehensive analysis of deflection-time history curves, it is important to note that the panel, subjected to mid-impact and long-span mid-impact, take comparatively longer time to reach its original position while short-span mid-impact exhibits the shortest time. After returning back to the original position, the panel starts to deform in the opposite direction. In Figure 6.11, the deflections in opposite directions are depicted as negative deflections. The panel, subjected to corner impact, exhibits the lowest deflection in the opposite direction while the case of long-span mid-impact exhibits the largest deflection in the opposite direction within the selected period.

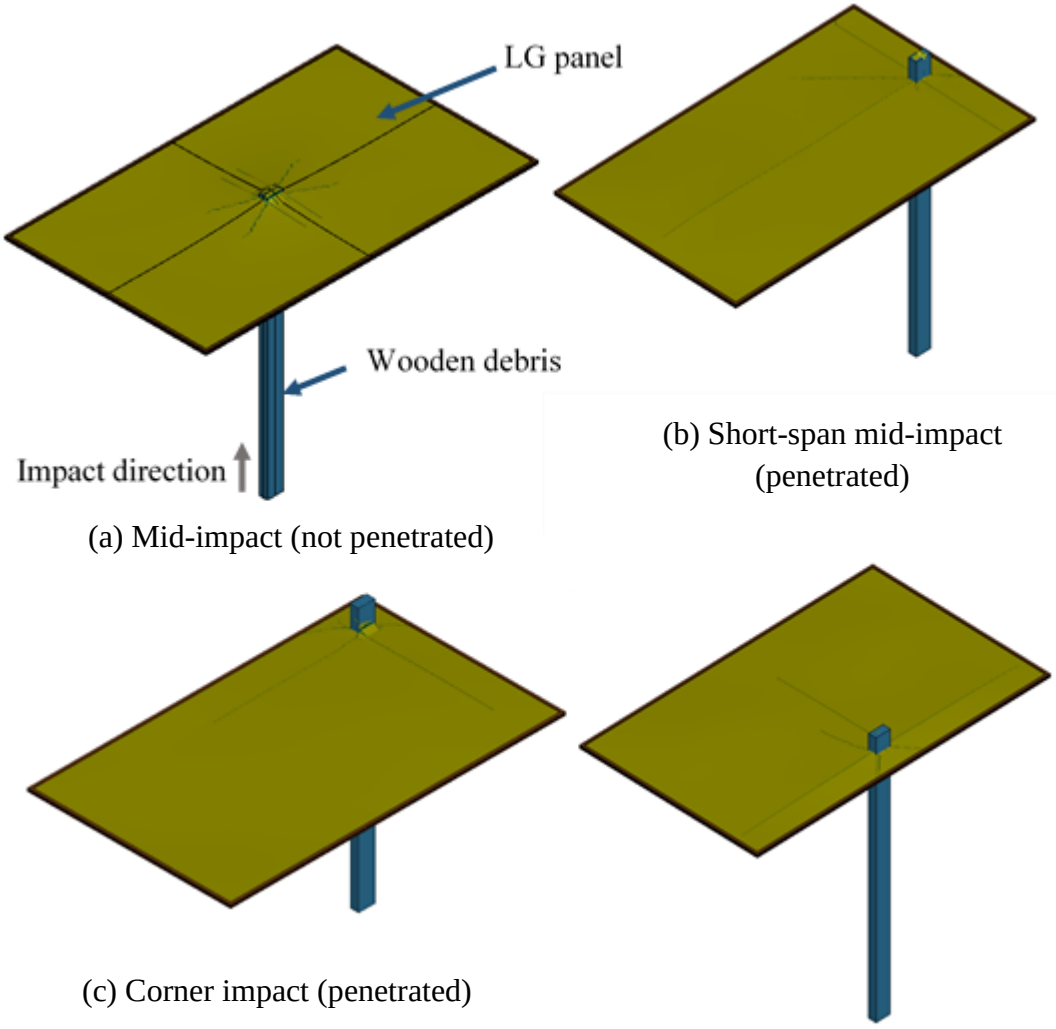

(a) Mid-impact (not penetrated)

(b) Short-span mid-impact (penetrated)

(c) Corner impact (penetrated)

(d) Long-span mid-impact (penetrated)

Figure 6.12 – Penetration status of the LG panel

6.4 Deformation of Perimeter Silicone Sealant Joints

When debris impacts the LG window panel, as discussed in Section 6.3, the window panel exhibits a deflection. Consequently, this deflection causes deformations in the perimeter silicone sealant joints that are attached to the window panel. In this section, deformations of the sealant joints are thoroughly analysed for the distinct impact locations considered in the study.

Figures 6.13, 6.14, and 6.15 illustrate the deformed sealant joints subjected to debris impact at different impact locations: corner; long-span mid; and short-span mid respectively. These figures exhibit the maximum deformations of silicone sealant in the impact direction (i.e. in the Z direction). Upon a comprehensive analysis of Figures 6.13 (a), 6.14 (a), and 6.15 (a), it is noticeable that sealant joints that are affixed to the front glass pane demonstrate stretching at the beginning as the LG panel exhibits a dynamic deflection towards the impact direction. At the same time, the sealant joints attached to the back glass pane experience compression. Therefore, the sealant elements in the impact zone demonstrate noticeable positive displacements.

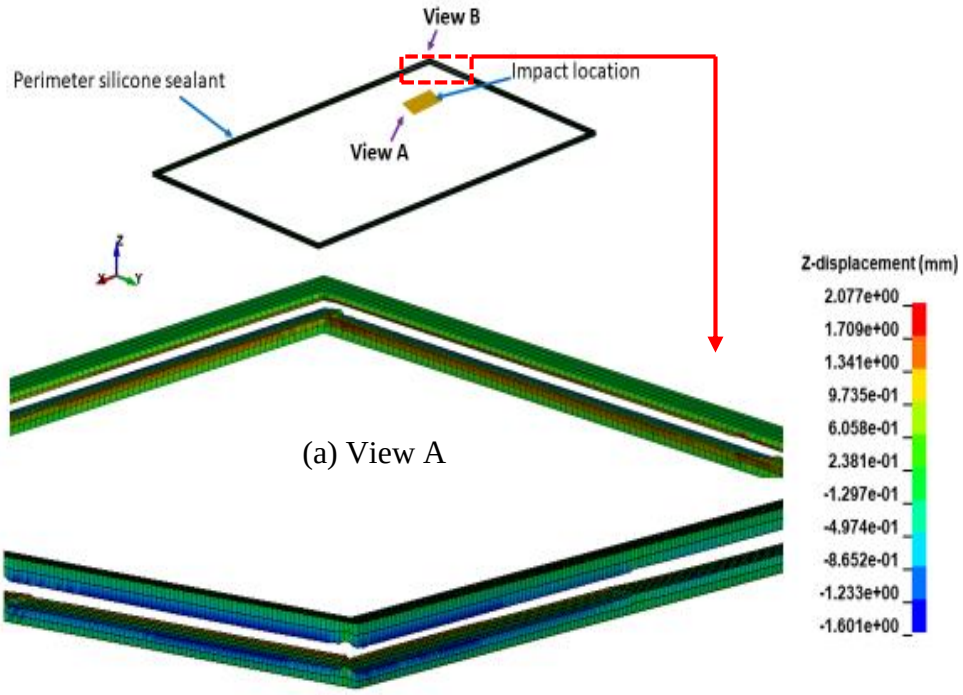

(a) View A

(b) View B

Figure 6.13 - Deformed sealant joints subjected to corner impact

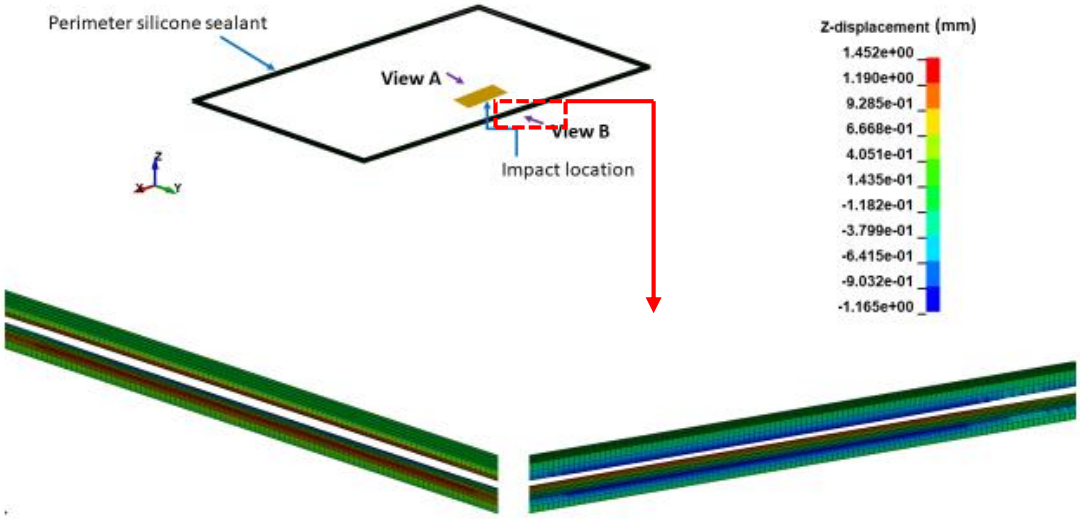

(a) View A (b) View B

Figure 6.14 - Deformed sealant joints subjected to long-span mid-impact

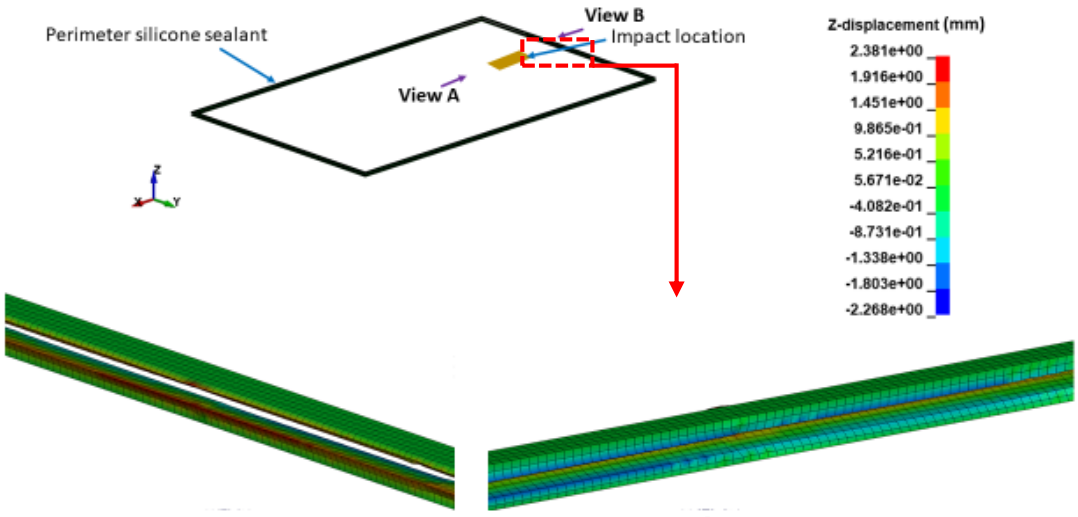

(a) View A (b) View B

Figure 6.15 - Deformed sealant joints subjected to short-span mid-impact

However, as illustrated in Figures 6.13 (b), 6.14 (b), and 6.15 (b), sealant elements on the opposing side of the same sealant layer exhibit slight variations. View B shows that these sealant elements affixed to the glass panes demonstrate noticeable negative displacements as the glass panes undergo deformations. Hence, the sealant elements affixed to the back glass pane experience stretching whereas those affixed to the front glass pane undergo compression. It is worth mentioning that the aforementioned deformations of the sealant joints are significantly noticeable exclusively near the impact location. The deformations of the sealant joints along the remaining perimeter edges are negligible compared to those depicted in Figures 6.13, 6.14, and 6.15. As sealant joints within the impact zone experience significant deformations, there is a potential for window frames near the impact area to deform when the sealant joints

undergo excessive deflections. Consequently, the LG panel becomes susceptible to dislodging from the supporting frame under a sudden impact load. In addition, as depicted in Figure 6.13, when the window panel is subjected to corner impact, there is a notable risk of the panel becoming dislodged from the corner as the sealant joints experience non-uniform deformations at the corner. Hence, special precautions should be taken while designing the sealant layers for impact-resistant glazing.

6.5 Variation of Internal Energy of the Materials

The variation of internal energy of different parts of the LG panel is analysed in this section concerning various impact locations. Figures 6.16, 6.17, and 6.18 depict the internal energy variation with time for the selected impact locations: corner impact; long-span mid-impact; and short-span mid-impact respectively. As it was mentioned previously, the debris hits the panel at 3.3 ms.

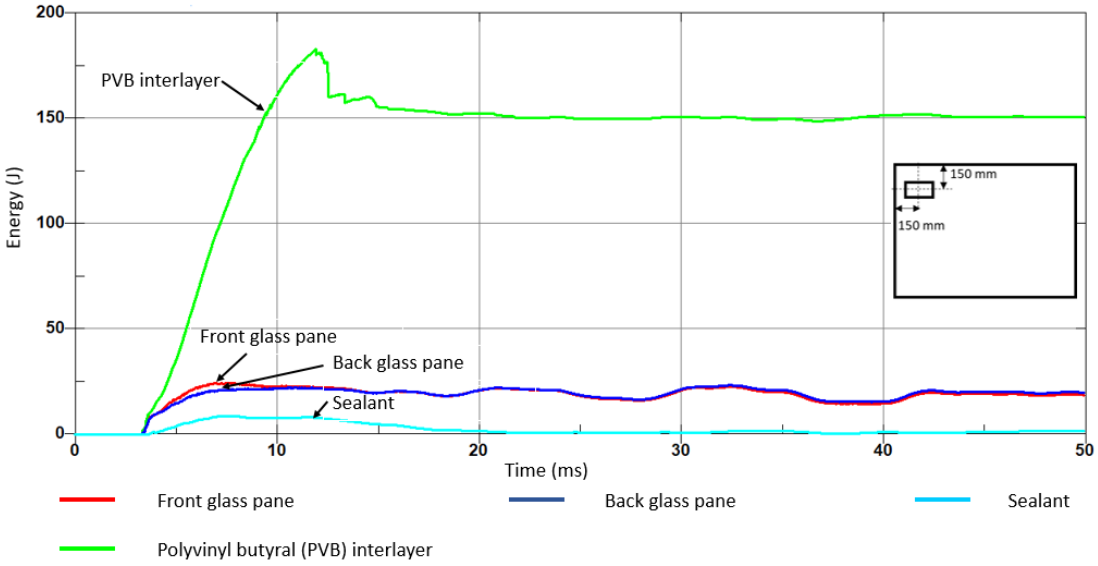

Figure 6.16 - Variation of internal energy of different parts of the LG panel subjected to corner impact

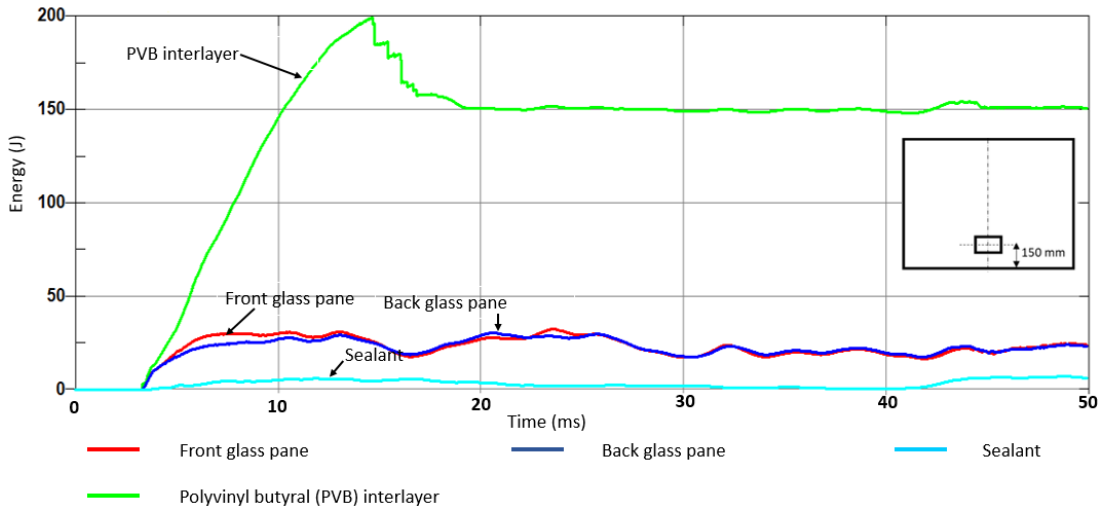

Figure 6.17 - Variation of internal energy of different parts of the LG panel subjected to long-span mid-impact

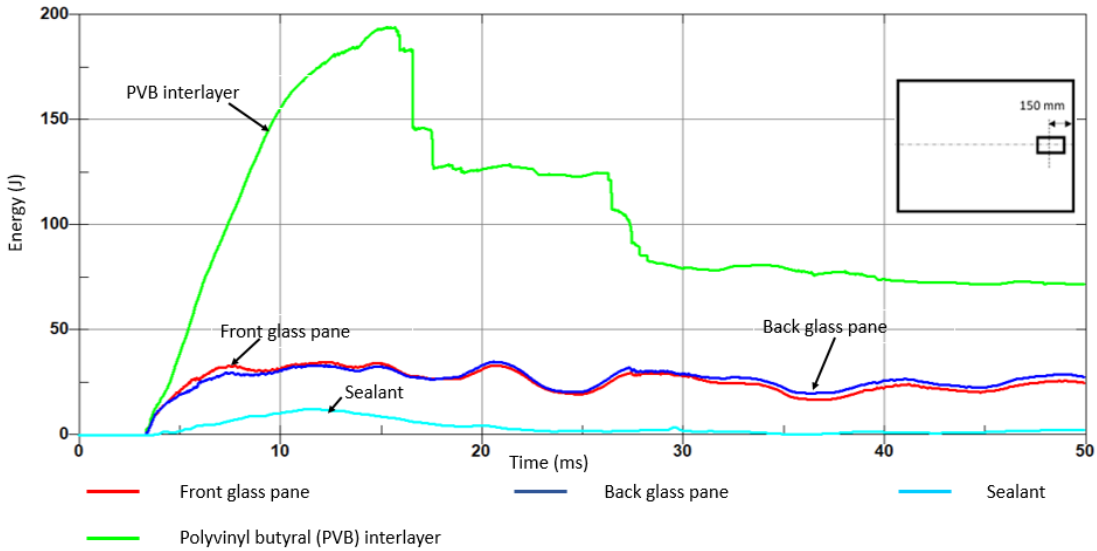

Figure 6.18 - Variation of internal energy of different parts of the LG panel subjected to short-span mid-impact

Figures 6.16, 6.17, and 6.18 demonstrate that the front glass pane and back glass pane exhibit similar patterns of internal energy with time. It is evident that the PVB interlayer absorbs a significant amount of impact energy. Hence, it exhibits comparatively higher internal energy values in its variation due to its identical viscoelastic behaviour. As the impact occurs, an obvious increase in the internal energy could be identified in the PVB interlayer. It arises due to the potential deformations of the interlayer. Furthermore, after a certain time, the interlayer exhibits a notable decrease and subsequent stabilisation which indicates that it has reached its maximum deformation and energy absorption capacity at this point. It is important to remember that the panel is penetrated by the debris in all the cases depicted in Figures 6.16, 6.17, and 6.18. In addition, it is evident that the PVB behaviour is significantly influenced by different interplaying parameters such as the impact load, impact duration, and the mechanical properties of PVB. It is worth mentioning that the internal energy of the sealant joints demonstrates comparatively low values and it is attributed by the deformations of the sealant joints exclusively near the impact location. As it was explained previously in Section 6.4, the deformations of the sealant joints along the remaining perimeter edges of the panel except those near the impact location are negligible. Consequently, the energy absorption of these silicone sealant joints also becomes minimal in all the cases. Subsequently, it is evident that the perimeter sealant joints considered in the selected fully frame arrangement do not have the ability to prevent the debris penetrations from effectively absorbing a significant amount of energy when the impact occurs at different impact locations. Hence, it is worth mentioning that the designers should take sufficient measures to improve the impact energy dissipation mechanism while designing the glass window panels of the building envelopes in cyclone-prone areas. With an efficient energy dissipation mechanism, the susceptibility of potential penetrations of the PVB interlayer can be minimised.

Figure 6.19 depicts the total energy variation of the LG panel over time in the four cases considered in the study.

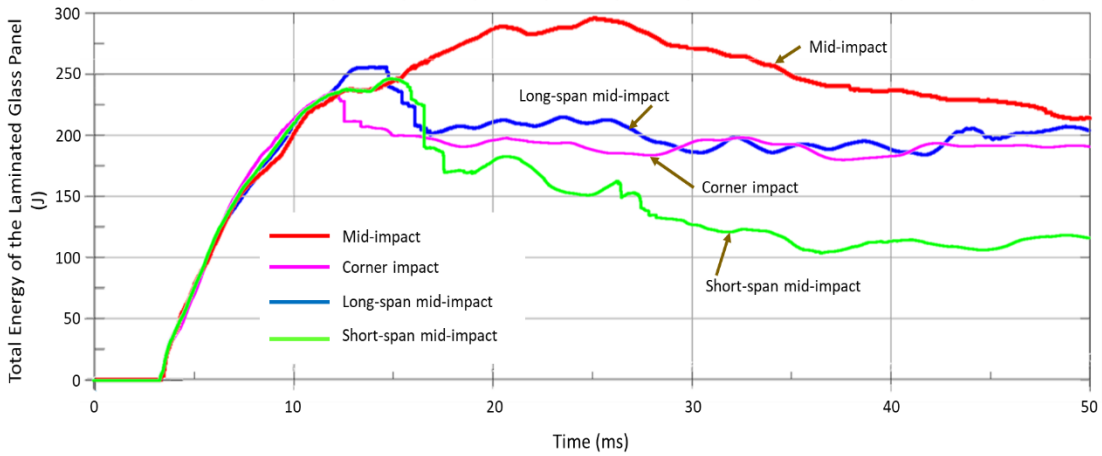

Figure 6.19 – Total energy variation of the LG panel

Among the four cases illustrated in Figure 6.19, the mid-impact case demonstrates the highest energy absorption value, reaching 298 J at the moment it reaches the maximum deflection. However, the other three cases demonstrate slightly lower maximum deflection values when compared to the mid-impact case. Among these three cases, long-span mid-impact case exhibits the highest energy, reaching 256 J.

6.6 Stress Variation and Material Failure

As the impact occurs at 3.3 ms, the variation of stress in the front glass pane, back glass pane, PVB interlayer, and silicone sealant joints are illustrated in this section. Material failure is also discussed in this section concerning the critical stress values of the materials. Figures 6.20, 6.21, and 6.22 demonstrate the stress variation of the front glass pane at 4 ms and 7 ms for different impact locations: corner of the panel; long-span mid; and short-span mid respectively.

The glass panes are considered to be failed when the maximum principal stress exceeds its dynamic breaking strength which is approximately 80 MPa. As it is demonstrated by the stress colour contours in Figures 6.20, 6.21, and 6.22, just after the impact occurs, the glass damage starts at the impact location showcasing 1st principal stress values higher than 80 MPa near the impact area (see Figures 6.20 (a), 6.21 (a), and 6.22 (a)). As stress waves propagate with time, the perimeter glass elements that are near the impact location gradually reach their failure (see Figures 6.20 (b), 6.21 (b), and 6.22 (b)). It is noticeable that the concentration of the stress waves is comparatively higher in the cases of corner impact and short-span mid-impact than in those of long-span mid-impact.

The stress contours of the back glass pane at 4 ms and 7 ms are illustrated in Figures 6.23, 6.24, and 6.25 concerning different impact locations: corner of the panel; long-span mid-section; and short-span mid-section respectively.

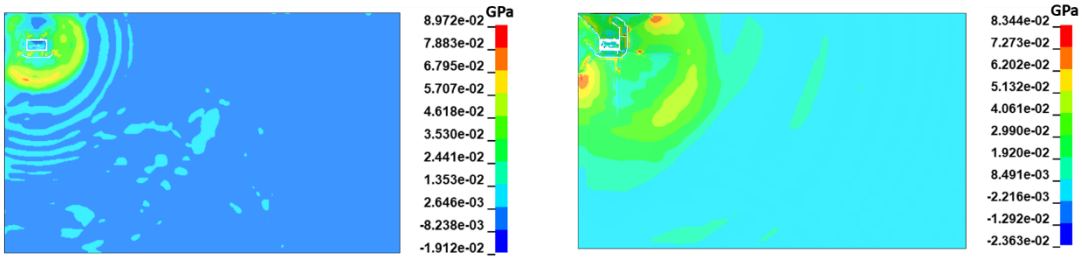

(a) At t = 4 ms (b) At t = 7 ms

Figure 6.20 - Variation of 1st principal stress on the top surface of the front glass pane (corner impact)

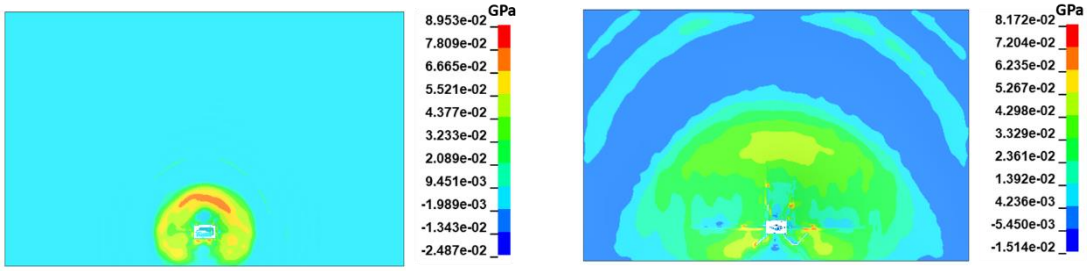

(a) At t = 4 ms (b) At t = 7 ms

Figure 6.21 - Variation of 1st principal stress on the top surface of the front glass pane (long-span mid-impact)

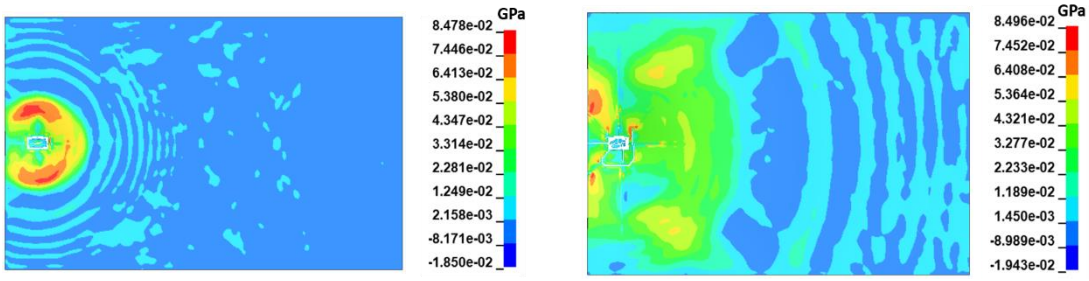

(a) At t = 4 ms (b) At t = 7 ms

Figure 6.22 - Variation of 1st principal stress on the top surface of the front glass pane (short-span mid-impact)

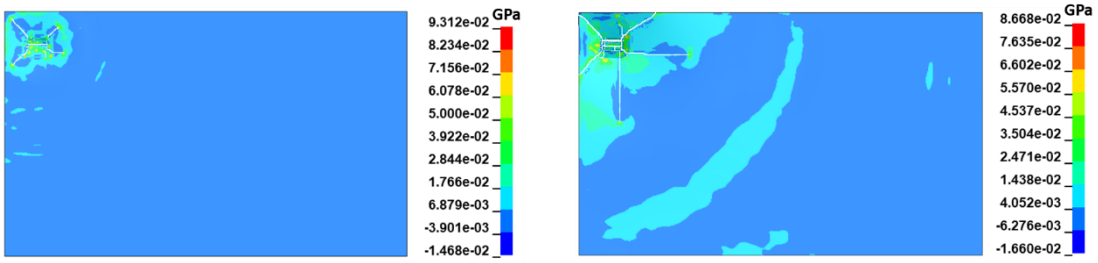

(a) At t = 4 ms (b) At t = 7 ms

Figure 6.23 - Variation of 1st principal stress on the inner surface of the back glass pane (corner impact)

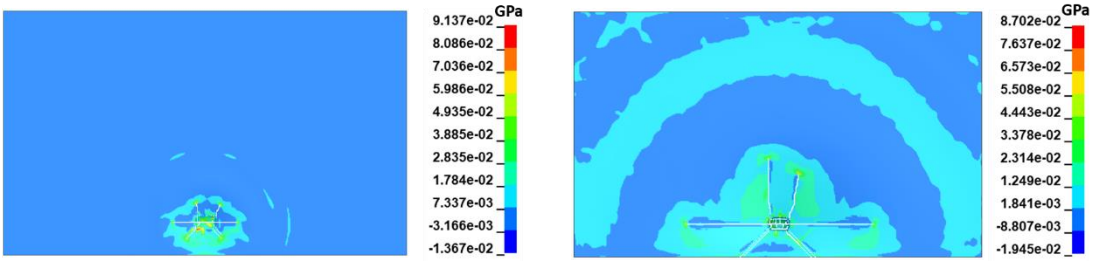

(a) At t = 4 ms (b) At t = 7 ms

Figure 6.24 - Variation of 1st principal stress on the inner surface of the back glass pane (long-span mid-impact)

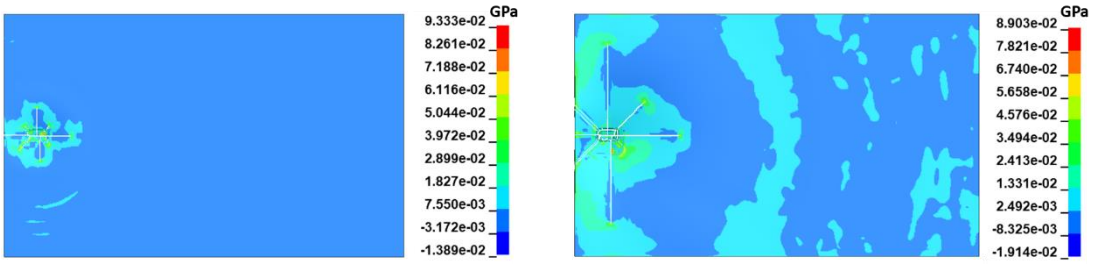

(a) At t = 4 ms (b) At t = 7 ms

Figure 6.25 - Variation of 1st principal stress on the inner surface of the back glass pane (short-span mid-impact)

Figures 6.23, 6.24, and 6.25 demonstrate that cracks in the back glass pane start at the impact point (see Figures 6.23 (a), 6.24 (a), and 6.25 (a)) and spread in the radial direction away from the impact point over the time (see Figures 6.23 (b), 6.24 (b), and 6.25 (b)). It is evident from the stress colour contours that the 1st principal stress values of glass near the cracks exceed the dynamic breaking strength of glass, ultimately resulting in more cracks and gradual expansion of cracks in radial directions. It is worth mentioning that, as cracks expand with time, there exists a potential risk of damaging the sealant joints affixed to the front and back glass panes, which arises due to the shattered glass fragments attached to the interlayer, especially when cracks reach the perimeter sealant joints.

The variation of Von Mises stress in the PVB interlayer is shown in Figures 6.26, 6.27, and 6.28 at 4 ms and 7 ms for the aforementioned impact locations. Upon a comprehensive analysis of Figures 6.26, 6.27, and 6.28, it is evident that immediately following the impact, the Von Mises stress at the impact location exceeds the yield stress of PVB (i.e. 11.41 MPa). Therefore, it is noticeable that the failure of the PVB interlayer initiates at the impact location as it is subjected to sudden concentrated impact load and stress concentrations at the point of impact. In addition, it becomes clear that the PVB interlayer is penetrated by the wooden projectile. It should be noted that the PVB interlayer experiences the highest stress values along the fractures of the glass panes.

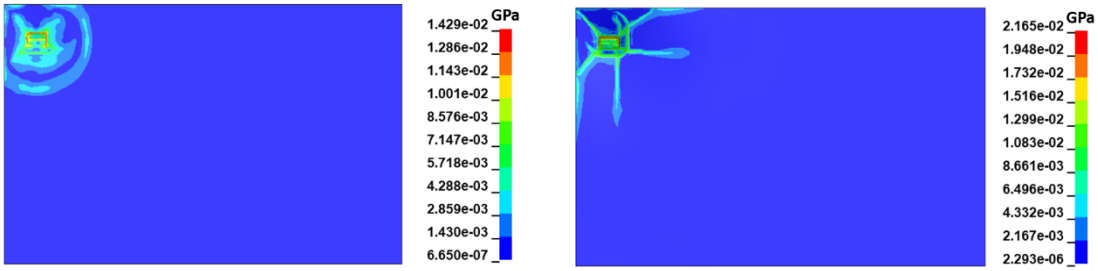

(a) At t = 4 ms (b) At t = 7 ms

Figure 6.26 - Variation of Von Mises stress in the PVB interlayer (corner impact)

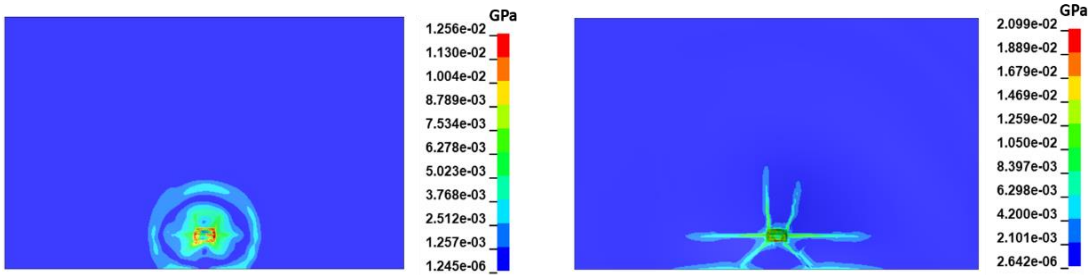

(a) At t = 4 ms (b) At t = 7 ms

Figure 6.27 - Variation of Von Mises stress in PVB interlayer (long-span mid-impact)

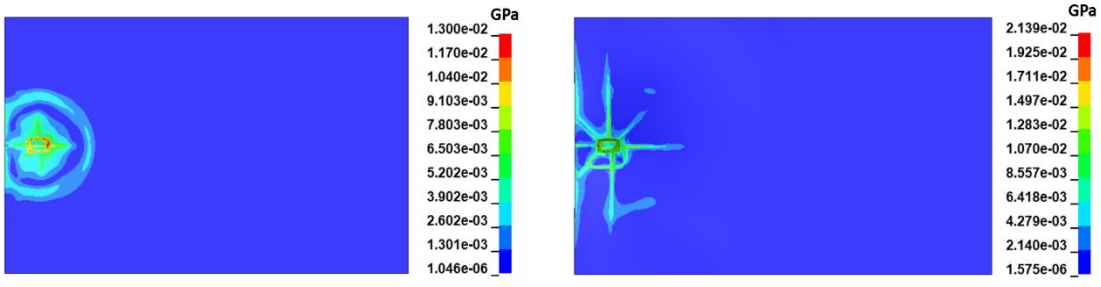

(a) At t = 4 ms (b) At t = 7 ms

Figure 6.28 - Variation of Von Mises stress in the PVB interlayer (short-span mid-impact)

Figures 6.29, 6.30, and 6.31 illustrate the variation of Von Mises stress of perimeter silicon sealant joints of the LG panel subjected to corner impact, long-span mid-span impact, and short-span mid-impact respectively.

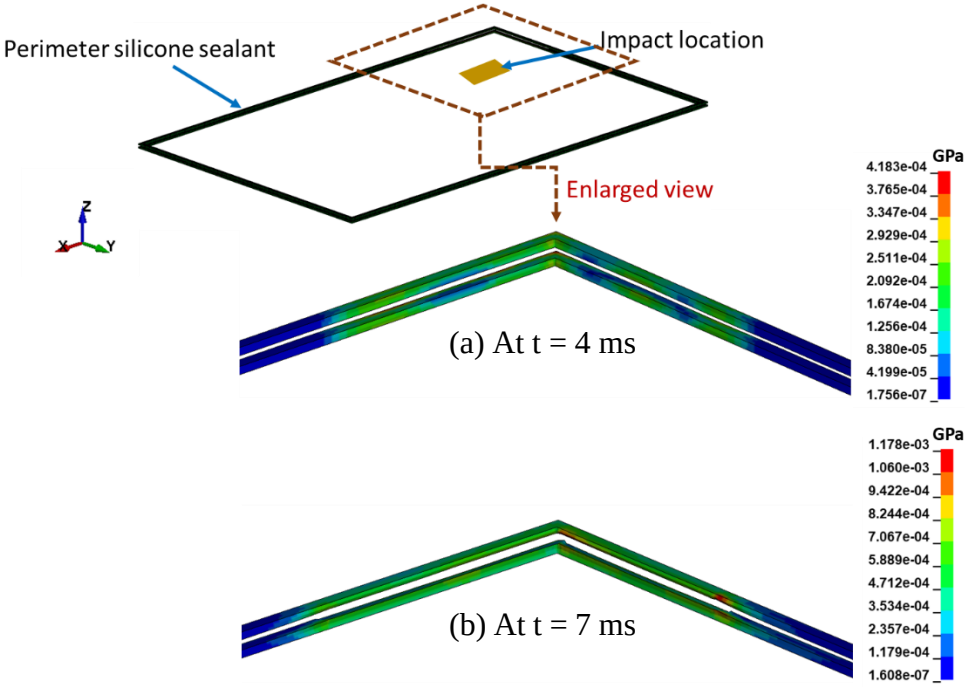

Figure 6.29 - Variation of Von Mises stress in the silicone sealant joints (corner impact)

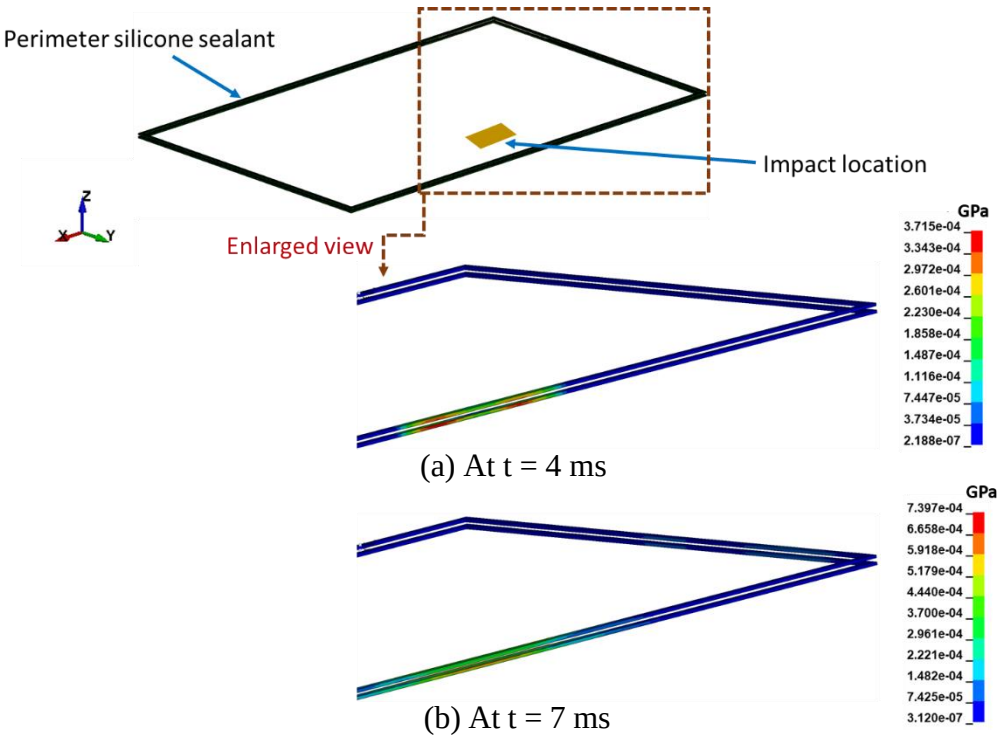

Figure 6.30 - Variation of Von Mises stress in the silicone sealant joints (long-span mid-impact)

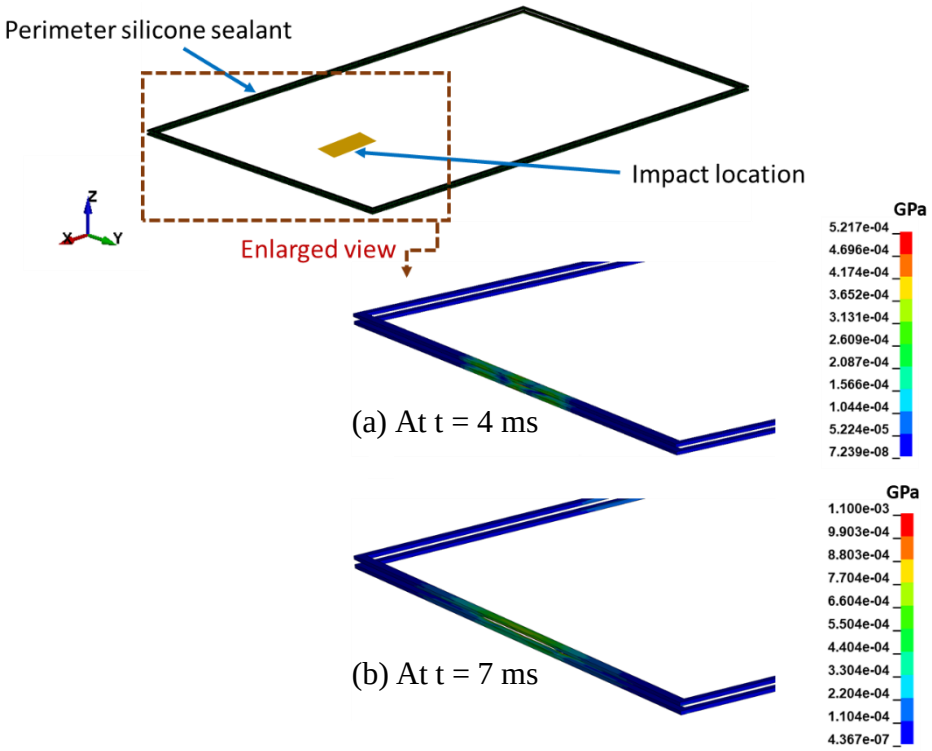

Figure 6.31 - Variation of Von Mises stress in the silicone sealant joints (short-span mid-impact)

Figures 6.29 (a), 6.30 (a), and 6.31 (a) demonstrate that immediately following the impact, the Von Mises stress in sealant joints near the impact location slightly increases. It is noticeable that the Von Mises stress in sealant joints increases with time (see Figures 6.29 (a), 6.30 (a), and 6.31 (a)). However, the Von Mises stress in sealant material does not exceed its yield stress (i.e. 2.3 MPa) under the aforementioned impact scenarios. Although the Von Mises stress does not surpass the threshold stress limit, it exhibits stress values that approach the yield point. It is evident that the likelihood of sealant failure is comparatively higher at the locations with localised stress concentrations. For example, Figures 6.29, 6.30, and 6.31 exhibit the highest stress concentrations at the points closest to the impact location. Consequently, these locations are susceptible to failure resulting in detachments and abnormal joint deformations when the panel is subjected to higher impact loads. It was found that the Von Mises stresses in perimeter sealant joints are highest for corner impacts, decreasing for short-span mid-impacts, long-span mid-impacts, and mid-impacts (see Figure 5.6), respectively

6.7 Chapter Summary

This chapter explored the behaviour of the LG window panel when subjected to impact from windborne debris at different locations of the panel. Firstly, a mesh convergence study was conducted to identify the optimum mesh configurations. After that, the optimum mesh arrangement that was identified by conducting the mesh convergence study was used in the study to investigate the response of the LG panel.

Upon a thorough examination, this chapter investigated the variations in the maximum dynamic deflection of the panel, changes in the deformation of perimeter silicone sealant joints, variations in the internal energy of the different parts and total energy of the LG panel, and the progression of stress variation in various segments and material failure. This study identified a notable contrast in the behaviour of the panel when subjected to corner impact, long-span mid-impact, and short-span mid-impact as compared to the impact that occurs at the geometric centre of the panel. It was observed that the penetration vulnerability was comparatively higher when subjected to impacts near the perimeter sealant joints. The changes in deformations are significantly higher in the sealant elements exclusively near the impact location. However, the deformations in the sealant elements away from the impact point are comparatively lower compared to those near the impact point. It was also noted that the PVB interlayer played a dominant role in dissipating the kinetic energy of the wooden projectile by absorbing a significant amount of energy until its failure compared to the other parts of the LG panel. Both the front and back glass panes exhibited an identical fluctuation in their internal energy. The energy absorption of the LG panel is highest for mid-impacts, decreasing for long-span mid-impacts, short-span mid-impacts, and corner impacts, respectively. This observation was reinforced by instances where the impactor could not penetrate the LG panel during mid-impacts, coinciding with the panel's maximum energy absorption. However, there was an increase in energy transferred to the support in the reverse scenario. It is worth mentioning that designers

should focus on designing effective energy dissipation mechanisms for building façades, especially when designing building envelopes in cyclone-prone regions. After a thorough examination of stress contours, it was found that cracks in glass panes start at the impact point and gradually spread in radial directions with time towards the perimeter edges. As the PVB interlayer is subjected to concentrated impact load and stress concentrations at impact locations, PVB failure initiates at the impact location. In addition, it was noticed that the likelihood of sealant failure is higher at the points of the sealant joints nearest to the impact location. Consequently, the sealant joints are susceptible to detachments, excessive deformations, or rupture at the points near the impact location.

After a comprehensive analysis of FE results, design strategies were formulated and they are presented in Chapter 7.

CHAPTER 7

CONCLUSION

7.1 Introduction

This chapter commences with an overview of the research study and it is presented in Section 7.2. Then, the main findings of the research are presented in Section 7.3, which is followed by the formulated design strategies are presented in Section 7.4. Finally, in Section 7.5, it presents the recommendations for future research with the limitations identified in the present study.

7.2 Summary of the Research Study

The research study presented in this thesis investigates the response of laminated glass (LG) panels subjected to windborne debris impact. A reliable finite element (FE) procedure was used in this study and the FE techniques were validated using the past experimental results available in the literature.

After identifying the research area, a preliminary literature survey was conducted, which was followed by a comprehensive literature review carried out throughout the research study. The key findings from the comprehensive literature review are presented in Chapter 2. LS-DYNA explicit FE code was used to develop three-dimensional (3D) FE models in the present study. Firstly, FE models were developed to simulate the impact occurring at the geometric centre of the LG panel. The FE results exhibited a reasonably good agreement with the previous experimental results available in the literature. After that, validated FE models were used to investigate the response of LG panels under varying support conditions: pinned conditions; fixed conditions; and silicone sealant support. In addition, energy absorption of different parts of the LG panel, stress variation, and material failure were thoroughly analysed. The impact response of the LG panel was numerically analysed by varying the thickness of the panel. Furthermore, the response of the LG panel was examined when subjected to impact at different locations of the panel: corner; long-span mid-section; and short-span mid-section. Upon a comprehensive analysis of the FE results, this research investigated the variations in maximum dynamic deflection of the panel, changes in deformations of silicone sealant joints, fluctuations in internal energy of different parts of the LG panel, and stress variation and material failure. Finally, design strategies for impact-resistant glazing were developed using the key findings of this study and those strategies are presented in Section 7.4.

It should be noted that the reliable FE modelling approach presented in this thesis can be utilised to study the impact behaviour of LG panels when subjected to different impact scenarios. The main findings of this study are presented in Section 7.3.

7.3 Main Findings of the Research

1. The validated FE models and modelling approach developed in this research are capable of predicting the response of the LG panels when subjected to windborne debris impact. The FE results, encompassing maximum dynamic deflection, energy absorption, internal energy in different parts of the panel, deformation of perimeter silicone sealant joints, and stress variation in glass, PVB, and sealant can be used to predict the impact resistance or potential failure of different constituent parts of the LG panel. Consequently, it becomes possible to evaluate the overall impact performance of the LG window panel.
2. When a panel, supported by perimeter silicone sealant joints, experiences an impact occurring at its geometric centre (i.e. mid-impact), it exhibits a behaviour that lies between the pinned and fixed conditions. However, the LG panel with pinned support conditions approximately predicts the impact behaviour of the panel with silicone sealant joints.
3. For mid-impact, the PVB interlayer plays a dominant role in resisting penetration by absorbing a significant amount of impact energy compared to the other constituent components of the LG panel. PVB exhibits its maximum energy absorption value when it reaches its maximum centre deflection.
4. Immediately following the mid-impact, glass cracking initiates at the impact point (i.e. panel centre) and extends towards the boundary edges in radial directions. However, as cracks spread away from the impact point, the crack density becomes lower. The likelihood of PVB failing at the impact location is notably higher. However, PVB can absorb the impact energy until its complete failure. As shock waves reach the panel edges, the perimeter sealant joints exhibit stress values initially at the mid-span of the longest edge of the panel. Then, stress waves spread towards the corner edges of the window panel. In mid-impact cases, silicone sealant joints experience considerably low-stress levels that are well below their yield stress.
5. When the LG panel is subjected to corner impact, it exhibits slightly lower dynamic deflection values than those of long-span mid-impact and short-span mid-impact. It is worth mentioning that although the panel is not penetrated by the debris during mid-impact exposure, FE simulations indicate that the same debris can penetrate the panel when subjected to identical impact loading at different locations, such as corner of the panel, long-span mid-section, or short-span mid-section.
6. When debris impacts the panel at the aforementioned distinct locations, there exists a potential risk of distorting the window frame near the impact point due to excessive deformation in the silicone sealant within that impact area. As a result, the panel becomes susceptible to dislodging from its supporting frame. In addition, during the corner impact situations, the panel is vulnerable to dislodging

from the corner as the silicone joints undergo non-uniform deformations at the corner.

7. PVB interlayer displays the highest internal energy compared to the other parts because of its ability to absorb a substantial amount of impact energy, owing to its identical viscoelastic properties. Both the front and back glass panes follow a similar pattern in their internal energy variations. By implementing an effective energy dissipation mechanism for building façades, the potential risk of PVB failure or penetration can be reduced.
8. The energy absorption of the LG panel is highest for mid-impacts, decreasing for long-span mid-impacts, short-span mid-impacts, and corner impacts, respectively. However, there was an increase in energy transferred to the support in the reverse scenario.
9. When debris impacts the LG panel at the specific locations illustrated in this thesis, glass cracking starts at the impact point and swiftly propagates away from the impact location in radial directions. PVB failure also initiates at the point of impact. Glass panes and PVB interlayer undergo localised stress concentrations at the impact point, which leads to the initiation of their failure at that location. It is worth mentioning that tiny glass shards adhered to the PVB interlayer and sealant joints can cause the tearing of the interlayer film and sealant material as the panel undergoes cyclic deformations with time after the impact occurs. Moreover, silicone sealant joints experience substantially higher stress levels than those in the mid-impact situation when the impact point is closer to the sealant joints. Sealant joints become susceptible to detachments, excessive deformations, or rupture in the areas near the impact point.
10. It was found that enhancing the impact performance of the LG panel cannot be achieved solely by adding thicker glass panes to the LG window panels without a well-thought-out design. The most appropriate strategy for impact-resistant glazing is to purposefully design the LG window panels as a sacrificial element, allowing it to fail by tearing the interlayer after absorbing a greater amount of impact energy.

Hence, the findings of this research will support manufacturers in developing innovative materials that exhibit good energy absorption characteristics. This, in turn, will encourage façade engineers to implement impact-resistant glazing technologies in practice by adopting to optimised and safe design concepts to create aesthetically pleasing glass façades in cyclone-prone regions.

7.4 Design Strategies for Impact-Resistant Glazing

This section presents the design strategies identified in the context of impact-resistant glazing based on the findings of this study.

It is obvious that the LG panel is prone to break upon impact. In this research, glass cracking was simulated by activating element deletion criterion in the numerical

model. In addition, the tearing of the interlayer was noted to occur when the Von Mises stress exceeded the yield stress of the PVB material. Hence, after a thorough analysis presented in this thesis, it became evident that the most appropriate approach for impact resistant glazing is to intentionally design the LG window panel as a sacrificial element, permitting it to fail by tearing the interlayer after absorbing a greater amount of impact energy. The tearing of the polymeric interlayer was identified as the safer failure mode compared to failure at the supports. As demonstrated by results presented in this thesis, the potential risk of debris penetration and support failure can be effectively reduced by adopting this approach, thus helping prevent total collapse or catastrophic failure of the glass façade. Consequently, the damaged window panel can be replaced with a new window panel. The use of LG in window panels also helps minimise the potential risk of free-flying glass fragments. Furthermore, in Section 5.5, it was found that enhancing the impact performance of the LG panel cannot be achieved solely by incorporating thicker glass panes into the LG window panels without careful design considerations. Through an analysis of the results via an iterative process, it has been identified that (case ii) has the most appropriate layer configuration for impact-resistant glazing among the four cases considered in Section 5.5. Similarly, a designer must undertake an iterative process to propose the most suitable layer thicknesses and configurations when designing impact-resistant glazing. Otherwise, additional material costs may be incurred for thicker glass panels that do not exhibit satisfactory impact resistance.

7.5 Recommendations for Future Research

This research formulates design strategies for impact-resistant glazing based on its key findings. Façade engineers can apply the novel insights presented in this thesis to develop optimised and safe designs. Nonetheless, there is a need for further research to fulfil specific knowledge gaps revealed while conducting the current study. The recommendations for future research and the limitations of the present study can be outlined as follows.

1. An extensive experimental program can be implemented to calibrate the FE models developed in this study, in addition to the past experimental results used in the present research to validate the modelling techniques.
2. This research aims to formulate design strategies for impact-resistant glazing, concerning different impact locations and support conditions. In this study, a standard timber block with a mass of 4 kg and an impact velocity of 15 ms^{-1} was considered. Hence, this study can be extended to conduct a comprehensive parametric study for investigating the effect of glass thickness, interlayer thickness, sealant properties, layer configurations, window dimensions, debris mass, and impact velocity on the impact performance of LG window panels. As a result, comprehensive guidance can be developed for impact-resistant glazing based on the results from the parametric study.

3. While developing FE models in this research, the deformations of the window frame were neglected and it was treated as a rigid frame. However, the sealant joints attached to the window frame were modelled to allow for free deformations upon impact. Therefore, the modelling techniques presented in this thesis can be extended to account for the flexibility of the window frame, thus investigating the effects of support flexibility on the impact performance of the LG panel.
4. In this study, an adhesive contact between the glass panes and the interlayer was not considered, and the interaction between these two components was treated to be fully bonded. Hence, the material delamination could not be simulated in the present study. Therefore, the established modelling techniques can be improved to simulate the material delamination phenomenon by modelling the adhesive contact between the glass and the interlayer.
5. The windborne debris impact phenomenon was exclusively considered in this research. It would be intriguing to conduct additional research studies to examine the impact performance of LG panels when exposed to specific cyclic pressure loading, exploring their post-breakage behaviour.
6. The fracture process of PVB and the initiation and propagation of cracks in glass panes were simulated in this study using an element deletion criterion. The FE modelling techniques established in this thesis can be enhanced by implementing the cohesive zone modelling method and the extended FE method to simulate the fracture process of the constituent components of the LG panel.
7. The behaviour of LG is significantly affected by the presence of random surface flaws, micro scratches in glass panes, and the existence of air bubbles between the layers. Therefore, advanced multi-scale modelling techniques can be used to investigate the effect of random surface flaws, micro scratches, and air bubbles in the LG composite on its performance under impact loads.

REFERENCES

ABRISA Technologies. (n.d.). *Glass strengthening methods*. Retrieved January 06, 2022, from ABRISA Technologies Website: https://abrisatechnologies.com/fabrication-facts/glass-strengthening-methods/.

Achintha, M. (2016). Chapter 5 - Sustainability of glass in construction. In Khatib, J.M., *Sustainability of Construction Materials* (2nd edition) (pp. 79-104). Woodhead Publishing. doi:10.1016/B978-0-08-100370-1.00005-6.

AIS Windshield Experts. (2014, April 09). *Process of manufacturing of laminated glass.* Retrieved January 22, 2022, from AIS Windshield Expert Website: https://www.flickr.com/photos/102443579@N03/13736252093/.

American Society of Civil Engineers (ASCE)/SEI 7-22. (2022)., *Minimum design loads for buildings and other structures.* 1801 Alexander Bell Drive, Reston, Virginia: ASCE. Retrieved from https://www.asce.org/publications-and-news/asce-7

American Society for Testing and Materials (ASTM) E 1886-05. (2005). *Standard test method for performance of exterior windows, curtain walls, doors, and impact protecting systems impacted by missile(s) and exposed to cyclic pressure differentials.* West Conshohocken, PA: ASTM International.

American Society for Testing and Materials (ASTM) E 1996-09. (2009). *Standard specification for performance of exterior windows, curtain walls, doors, and impact protective systems impacted by windborne debris in hurricanes.* West Conshohocken, PA: ASTM International.

Architecture & Design. (2017, May 08). *Jackson Architecture among firms to tackle health challenges in the tropics*. Retrieved May 10, 2022, from Architecture & Design Website: https://www.architectureanddesign.com.au/projects/education-research/jackson-architecture-among-firms-to-tackle-health.

Architectuul. (n.d.). *Parada Tokyo Building*. Retrieved January 10, 2022, from Architectuul Website: https://architectuul.com/architecture/prada-tokyo-building.

Australian Standard (AS) 1288:2021. (2021). *Glass in buildings - Selection and installation.* Australia: Standards Australia Limited.

Australian/New Zealand Standard (AS/NZS) 1170.2:2011. (2011). *Structural design actions. Part 2: Wind actions.* Sydney, NSW 2001 and Wellington 6011: SAI Global Limited.

Behr, R.A., and Minor, J.E. (1994). A survey of glazing system behaviour in multi-story buildings during Hurricane Andrew. *The Structural Design of Tall Buildings, 3*, 143-161. doi:10.1002/tal.4320030302.

Chen, S., Zang, M., Wang, D., Yoshimura, S., and Yamada, T. (2017). Numerical analysis of impact failure of automotive laminated glass: A review. *Composites Part B*. doi:10.1016/j.compositesb.2017.04.007.

Choy, C.W., Wu, M.C., and Lee, T.C. (2020). Assessment of the damages and direct economic loss in Hong Kong due to Super Typhoon Mangkhut in 2018. *Tropical Cyclone Research and Review, 9*(4), 193-205. doi:10.1016/j.tcrr.2020.11.001.

Cormie, D., Mays, G., and Smith, P. (2009). *Blast effects on buildings.* (2nd edition). Thomas Telford Services Ltd. Retrieved from https://www.amazon.com/Blast-Effects-Buildings-2nd-Cormie/dp/0727735217.

Cyclone Testing Station, James Cook University, Australia. (2017). *Simulated windborne debris impact testing of building envelope components - Technical Note No.04.* Townsville QLD 4811 Australia: Cyclone Testing Station, James Cook University, Australia. Retrieved August 05, 2022, from https://www.jcu.edu.au/__data/assets/pdf_file/0003/1171362/Tech-Note-4-Windborne-Debris-Impact-Testing.pdf.

Department of Public Works, Queensland Government. (2006). *Design guidelines for Queensland public cyclone shelters.* Queensland: The State of Queensland, Department of Public Works. Retrieved August 05, 2022, from https://www.housing.qld.gov.au/__data/assets/pdf_file/0023/5558/designguidelinesqueenslandpubliccycloneshelters.pdf.

Department of Science, Bureau of Meteorology. (1977). *Report on cyclone Tracy December 1974.* Canberra: Australian Government Publishing Service.

Experimental Building Station. (1978). *Technical Record 440 – Guidelines for the testing and evaluation of products for cyclone-prone areas.* Experimental Building Station.

Fowza, M.J.F. and Hidallana-Gamage, H.D. (2020). Study on use of glass in Sri Lankan construction industry. *2020 Moratuwa Engineering Research Conference (MERCon)* (pp. 107-112). Moratuwa: Institute of Electrical and Electronics Engineers. doi:10.1109/MERCon50084.2020.9185303.

Francis, L.F. (2016). Chapter 3 - Melt processes. In L. Francis, *Materials Processing: A Unified Approach to Processing of Metals, Ceramics and Polymers* (pp. 105-249). Academic Press. doi:10.1016/B978-0-12-385132-1.00003-3.

Gilani, G. (2020). *MCDM approach for assessing the sustainability of buildings' facades* [PhD Thesis]. Barcelona, Spain: University Research Institute for Sustainability Science and Technology (IS.UPC). Retrieved from https://www.tdx.cat/bitstream/handle/10803/669822/TGG1de1.pdf?sequence=1&isAllowed=y.

Glass Academy. (2016, September 06). *Heat-strengthened glass, tempered glass, and laminated glass*. Retrieved January 22, 2022, from Glass Academy Website: http://glass-academy.com/blog/.

GW News. (2021, May 02). *How the float glass process has revolutionised the glass industry*. Retrieved January 16, 2022, from GW News Website: https://www.gw-news.eu/node/160746/print.

Hadhi, I. (2019, January 30). *Future of building envelopes (façades) in Sri Lanka*. Retrieved October 02, 2021, from Daily FT: https://www.ft.lk/propertyconstruction/Future-of-building-envelopes--fa%C3%A7ades--in-Sri-Lanka/10516-671904.

Hidallana-Gamage, H.D. (2015). *Response of laminated glass panels to near field blast events* [PhD Thesis]. Queensland University of Technology, School of Civil Engineering and Built Environment, Faculty of Science and Engineering. Brisbane, Australia: Queensland University of Technology. Retrieved from https://eprints.qut.edu.au/85263/1/Hasitha%20Damruwan_Hidallana%20Gamage_Thesis.pdf.

Hidallana-Gamage, H.D., Thambiratnam, D.P., and Perera, N.J. (2013). Computational analysis of laminated glass panels under blast loads: A comparison of two dimensional and three dimensional modelling approaches. *International Journal of Engineering and Science, 2*(8), 69-79.

Hidallana-Gamage, H.D., Thambiratnam, D.P., and Perera, N.J. (2014). Numerical modelling and analysis of the blast performance of laminated glass panels and the influence of material parameters. *Engineering Failure Analysis, 45*, 65-84. doi:10.1016/j.engfailanal.2014.06.013.

Holmes, J.D., Kwok, K.C.S., and Ginger, J.D. (2012). Wind loading handbook for Australia and New Zealand - Background to AS/NZ 1170.2 wind actions. Australian Wind Engineering Society.

Holmquist, T.J., Johnson, G.R., Lopatin, C., Grady, D., and Hertel Jr, E.S. (1995). *High strain rate properties and constitutive modelling of glass.* Sandia National Lab. (SNL-NM), Albuquerque, NM (United States). doi:10.2172/41367.

Honfi, D., Reith, A., and Vigh, L. G. (2014). Why glass structures fail? - Learning from failures of glass structures. *Challenging Glass 4 & COST Action TU0905 Final Conference* (pp. 791-800). Taylor & Francis Group, London. doi:10.1201/b16499-109.

Hong Kong Observatory. (2020, February 11). *Super Typhoon Mangkhut (1822): 7 to 17 September 2018*. Retrieved March 12, 2022, from Hong Kong Observatory Website: https://www.hko.gov.hk/en/informtc/mangkhut18/report.htm.

Huang, X.H., Wang, X.E., Yang, J., Pan, Z., Wang, F., and Azim, I. (2021). Nonlinear analytical study of structural laminated glass under hard body impact in the pre-crack stage. *Thin-Walled Structures, 167*, 1-17. doi:10.1016/j.tws.2021.108137.

Inhabit Group. (n.d.). *Integrated Marine Operations Centre*. Retrieved September 12, 2022, from Inhabit Group Website: https://inhabitgroup.com/project/integrated-marine-operations-centre/.

Jayaweera, G.C.S., Hidallana-Gamage, H.D., and Baleshan, B. (2022). Case studies on blast behaviour of glass façades: Sri Lanka Easter bombings. *2022 Moratuwa Engineering Research Conference (MERCon)* (pp. 1-6). Moratuwa, Sri Lanka: The Institute of Electrical and Electronics Engineers. doi:10.1109/MERCon55799.2022.9906182.

Johnson, G.R., and Holmquist, T.J. (1993). An improved computational constitutive model for brittle materials. *AIP conference proceedings* (pp. 981-984). Colorado, USA: Colorado Springs.

Kragh, M.K. (2011). The decade of the facade engineer. *Intelligent Glass Solutions*(1). Retrieved from https://www.cibse.org/media/frvkksbu/kragh-4.pdf

Landsea, C.W., Franklin, J.L., McAdie, C.J., Beven, J.L., Gross, J.M., Jarvinen, B.R., Pasch, R.J., Rappaport, E.N., Dunion, J.P., and Dodge, P.P. (2004). A reanalysis of Hurricane Andrew's intensity. Bulletin of the American Meteorological Society, 85(11), 1699-1712. doi:10.1175/bams-85-11-1699.

Lee, B.E., and Wills, J. (2002). Vulnerability of fully glazed high-rise buildings in tropical cyclones. *Journal of Architectural Engineering, 8*(2), 42-48. doi:10.1061/(ASCE)1076-0431(2002)8:2(42).

Legislative Council. (2018). *The Government's preparations, emergency response and recovery efforts arising from Super Typhoon Mangkhut.* Discussion Paper of House Committee Meeting on 4th October , 2018, Legislative Council Paper No. CB(2)2055/17-18(01). Retrieved from https://www.legco.gov.hk/yr17-18/english/hc/papers/hc20181004cb2-2055-1-e.pdf.

Li, Y., and Stewart, M.G. (2011). Cyclone damage risks caused by enhanced greenhouse Conditions and economic viability of strengthened residential construction. *Natural Hazards Review, 12*(1), 9-18. doi:10.1061/(asce)nh.1527-6996.0000024.

Lin, N. (2005). *Simulation of windborne debris trajectories* [MSc Thesis]. Texas Tech University, Department of Civil, Environmental, & Construction Engineering. Lubbock, Texas: Texas Tech University, US.

Lin, N., Holmes, J.D., and Letchford, C.W. (2007). Trajectories of wind-borne debris in horizontal winds and applications to impact testing. *Journal of Structural Engineering, 133*(2), 274-282. doi:10.1061/(ASCE)0733-9445(2007)133:2(274).

Liu, B., Xu, T., Xu, X., Wang, Y., Sun, Y., and Li, Y. (2015). Energy absorption mechanism of polyvinyl butyral laminated windshield subjected to head impact: Experiment and numerical simulations. *International Journal of Impact Engineering, 90*, 26-36. doi:10.1016/j.ijimpeng.2015.11.010.

Magic Glass. (n.d.). *How is laminated glass made?* Retrieved January 22, 2022, from Magic Glass Website: https://magicglass.com.au/blogs/glass-blog-glazing-glass-projects-rope-access-news/how-is-laminated-glass-made.

Makwana, R.R. (2013). Design consideration of facade wall system. *International Journal of Engineering Research & Technology (IJERT), 2*(4), 2449-2453.

Mason, M., and Haynes, K. (2010). *Historical case studies of extreme events: Adaptation lessons from cyclone Tracy.* Gold Coast: National Climate Change Adaptation Research Facility.

Mejorin, A., Trabucco, D., and Stelzer, I. (2019). *Cyclone-resistant façades: Best practices in Australia, Hong Kong, Japan, and the Philippines.* Chicago, USA: Council on Tall Buildings and Urban Habitat.

Meyland, M.J., and Nielsen, J.H. (2020). Ongoing research into the failure of glass at high strain rates. Paper presented at Challenging Glass 7, Conference on Architectural and Structural Applications of Glass. 7. Ghent University, Belgium: Belis, Bos & Louter (Eds.). doi:10.7480/cgc.7.4428.

Minor, J.E. (2005). Lessons learned from failures of the building envelope in windstorms. *Journal of Architectural Engineering, 11*(1), 10-14. doi:10.1061/(ASCE)1076-0431(2005)11:1(10).

Minor, J.E., McDonald, J.R., and Mehta, K.C. (1993). The tornado: an engineering-oriented perspective. Washington DC: National Oceanic and Atmospheric Administration, US Department of Commerce. Retrieved from https://repository.library.noaa.gov/view/noaa/7227.

Minor, J.E., and Mehta, K.C. (1979). Wind damage observations and implications. *Journal of the Structural Division, 105*, 2279-2291. doi:10.1061/JSDEAG.0005277.

Nascimento, M.L.F. (2014). Brief history of the flat glass patent - Sixty years of the float process. *World Patent Information, 38*(2014), 50-56. doi:10.1016/j.wpi.2014.04.006.

National Hurricane Centre. (2018). *Costliest U.S. tropical cyclones tables updated.* Miami: US Department of Commerce. Retrieved from https://www.nhc.noaa.gov/news/UpdatedCostliest.pdf.

Nawar, M., Salim, H., Newberry, M., and El-Sisi, A. (2021). High strain rate response of laminated glass interlayer materials. *Construction and Building Materials, 299*, 1-12. doi:10.1016/j.conbuildmat.2021.123934.

Nayer, M. (2011, December 18). Hyatt Regency New Orleans re-opens after Katrina (Photos). Retrieved January 20, 2022, from HuffPost Contributor Website: https://www.huffpost.com/entry/hyatt-regency-new-orleans_b_1013756.

Netherton, M.D., and Stewart, M.G. (2009). Probabilistic modelling of safety and damage blast risks for window glazing. *Canadian Journal of Civil Engineering, 36*(8), 1321-1331. doi:10.1139/L08-144.

Nippon Sheet Glass Co. Ltd. (n.d.). *The float process*. Retrieved January 16, 2022, from NSG Group Website: https://www.pilkington.com/en/global/knowledge-base/glass-technology/the-float-process/the-float-process.

Owen, J.S. (2015). Windborne debris in the urban environment. *Technical Journal, Construction Issue 2-B*(12), 145-165. doi:10.4467/2353737XCT.15.130.4167.

Peng, L., and Li, Y. (2019). Wind impacts on buildings in Hong Kong due to Mangkhut. Research Forum 2019 Impacts of Super Typhoon Mangkhut May 3, 2019. Retrieved from https://www.hko.gov.hk/en/research_forum/files/RF2019_Prof_YGLi.pdf.

Peroni, M., Solomos, G., Pizzinato, V., and Larcher, M. (2011). Experimental investigation of high strain-rate behaviour of glass. Applied Mechanics and Materials, 82(2011), 63-68. doi:10.4028/www.scientific.net/AMM.82.63.

Pilkington, L.A.B. (1969). Review lecture: The float glass process. *Proc. R. Soc. Lond. A. 314*, pp. 1-25. London: The Royal Society. doi:10.1098/rspa.1969.0212.

Powar, O., and Jayachandran A. (2021). Learning from façade failures over urban landscape: Aftermath of cyclone vardah. *Natural Hazards Review, 22*(1). doi:10.1061/(ASCE)NH.1527-6996.0000424.

Pratama, Y.T., and Susetyo, B. (2019). Cost analysis of facade work in high-rise building by value engineering method. *International Journal of Engineering Research and Advanced Technology (IJERAT), 5*(7), 100-109. doi:10.31695/ IJERAT.2019.3537.

Qingdao Morn Building Materials Co. Ltd. (2019, June 15). *Glass processing - Laminated glass processing*. Retrieved January 22, 2022, from MORN Glass Website: https://www.mornglass.com/glass-processing-laminated-glass.html.

Rappaport, E.N. (1993). *Preliminary Report: Hurricane Andrew, 16 - 28 August, 1992.* Miami: National Hurricane Center, US Department of Commerce. Retrieved February 05, 2022, fromhttps://web.archive.org/web/20160906055141/http: //www.nhc.noaa.gov/1992andrew.html.

Shetty, M.S., Wei, J., Dharani, L.R., and Stutts, D.S. (2013). Analysis of damage in laminated architectural glazing subjected to wind loading and windborne debris impact. *Buildings, 3*(2), 422-441. doi:10.3390/buildings3020422.

Silvestru, V.A., Englhardt, O., and Schneider, J. (2019). Linear adhesive connections at the edge of laminated glass panes: an experimental study under tensile, compressive and shear loading. *Glass Structures & Engineering, 4*, 45–68. doi:10.1007/s40940-018-0080-y.

Suwen, C., Xing, C., and Xiqiang, W. (2018). The mechanical behaviour of polyvinyl butyral at intermediate strain rates and different temperatures. *Construction and Building Materials, 182*, 66-79. doi:10.1016/j.conbuildmat.2018.06.080.

Swift Glass. (2016, November 08). *Thermal glass tempering vs. Chemical strengthening: What's the difference?* Retrieved January 06, 2022, from Swift Glass Website: https://www.swiftglass.com/blog/thermal-glass-tempering-vs-chemical -strengthening-whats-difference/.

Tachikawa, M. (1983). Trajectories of flat plates in uniform flow with application to wind-generated missiles. *Journal of Wind Engineering and Industrial Aerodynamics, 14*(1-3), 443-453. doi:10.1016/0167-6105(83)90045-4.

Tamura, Y. (2009). Wind-induced damage to buildings and disaster risk reduction. The Seventh Asia-Pacific Conference on Wind Engineering, APCWE-VII. Taipei, Taiwan.

Taywade, P., and Shejwal, S. (2015). Structural design of a glass facade. *International Journal of Scientific and Research Publications, 5*(3), 1-6. Retrieved from http://www.ijsrp.org/research-paper-0315.php?rp=P393822.

Teotia, M., and Soni, R.K. (2018). Applications of finite element modelling in failure analysis of laminated glass composites: A review. *Engineering Failure Analysis, 94*, 412-437. doi:10.1016/j.engfailanal.2018.08.016.

Uematsu, Y., Suzuya, J., and Nozawa, T. (1992). Building damage in Aomori and Akita prefectures due to Typhoon No.19 of 1991. *Journal of Wind Engineering, 1992*(51), 35-47. doi:10.5359/jawe.1992.51_35.

Viridian Glass. (2011). *Test procedure to evaluate the performance of cyclone-resistant glazing when subject to the test criteria of AS1170.2-2011*. Viridian Glass.

Walker, G.R. (1975). *Report on cyclone Tracy: Effect on buildings.* Department of Housing and Construction, Australia.

Walker, G.R. (1991). The application of wind engineering technology to the mitigation of damage to housing from tropical cyclones - an Australian achievement. *International Conference on Impact of Disasters.* Los Angeles, USA.

Walker, G.R. (2010). A review of the impact of Cyclone Tracy on building regulations and insurance. Australian Meteorological and Oceanographic Journal, 60(3), 199-206. doi:10.22499/2.6003.008.

Wang, X.E., Huang, X.H., Yang, J., Hou, X., Zhu, Y., and Xie, D. (2021). Experimental and analytical study on the pre-crack impact response of thick multi-layered laminated glass under hard body impact. *International Journal of Mechanical Sciences, 206*, 1-20. doi:10.1016/j.ijmecsci.2021.106613.

Wikimedia. (2018, September 17). *Hang Seng Bank Headquarters Building after Typhoon Mangkhut*. Retrieved January 20, 2022, from Wikimedia: https://commons.wikimedia.org/wiki/File:Hang_Seng_Bank_Headquarters_Building_after_Typhoon_Mangkhut.jpg.

Wikimedia. (2018, September 17). *Immigration Tower in Wan Chai damaged by Typhoon Mangkhut 2018*. Retrieved January 20, 2022, from Wikimedia: https://commons.wikimedia.org/wiki/File:Immigration_Tower_in_Wan_Chai_damaged_by_Typhoon_Mangkhut_%282018%29.jpg.

Wikimedia. (2018, September 18). *Two Harbourfront after Typhoon Mangkhut 2018*. Retrieved January 20, 2022, from Wikimedia: https://commons.wikimedia.org/wiki/File:Two_Harbourfront_after_Typhoon_Mangkhut_201809.jpg.

Wikipedia. (2013, March 23). Aldar Headquarters in Abu Dhabi [image]. Retrieved January 10, 2022, from Wikipedia: https://en.wikipedia.org/wiki/Aldar_Headquarters_building#/media/File:Aldar_Headquarters_Building.jpg.

Williams, D.J., and Redgen, B.N. (2012). *Investigation into Australian impact testing methods and criteria for glass façades* [Project Thesis]. Brisbane: Queensland University of Technology, Australia.

Wills, J.A.B, Lee, B.E., and Wyatt, T.A. (2002). A model of wind-borne debris damage. *Journal of Wind Engineering and Industrial Aerodynamics, 90*(4-5), 555-565. doi:10.1016/S0167-6105(01)00197-0.

Yarosh, K., Wolf, A.T., and Sitte, S. (2008). Evaluation of silicone sealants at high movement rates relevant to bomb mitigating window and curtainwall design. *Journal of ASTM International, 6*(2). doi:10.1520/JAI101953.

Yuan, Y., Xu, C., Xu, T., Sun, Y., Liu, B., and Li, Y. (2017). An analytical model for deformation and damage of rectangular laminated glass under low-velocity impact. *Composite Structures*. doi:10.1016/j.compstruct.2017.06.029.

Zavadskas, E.K., Kaklauskas, A., Turskis, Z., and Tamošaitien, J. (2008). Selection of the effective dwelling house walls by applying attribute values determined at intervals. Journal of Civil Engineering and Management, 14(2), 85-93.

Zhang, X., Hao, H., and Ma, G. (2013). Laboratory test and numerical simulation of laminated glass window vulnerability to debris impact. *International Journal of Impact Engineering, 55*, 49-62. doi:10.1016/j.ijimpeng.2013.01.002.

Zhang, X., Hao, H., and Ma, G. (2014). Dynamic material model of annealed soda-lime glass. *International Journal of Impact Engineering, 77*(2015), 108-119. doi:10.1016/j.ijimpeng.2014.11.016.

Zhang, X., Hao, H., Shi, Y., and Cui, J. (2015). The mechanical properties of Polyvinyl Butyral (PVB) at high strain rates. *Construction and Building Materials, 93*, 404-415. doi:10.1016/j.conbuildmat.2015.04.057.

Zhang, X., Liu, H., Maharaj, C., Zheng, M., Mohagheghian, I., Zhang, G., Yan, Y., and Dear, J.P. (2020). Impact response of laminated glass with varying interlayer materials. *International Journal of Impact Engineering, 139*, 1-15. doi:10.1016/j.ijimpeng.2020.103505.

Zhang, X., Zou, Y., Hao, H., Li, X., Ma, G., and Liu, K. (2012). Laboratory test on dynamic material properties of annealed float glass. *International Journal of Protective Structures, 3*(4), 407-430. doi:10.1260/2041-4196.3.4.407.

Zhao, C., Yang, J., Wang, X.E., and Azim, I. (2019). Experimental investigation into the post-breakage performance of pre-cracked laminated glass plates. *Construction and Building Materials, 224*, 996-1006. doi:10.1016/j.conbuildmat.2019.07.286.

Zhou, X.Q., Wang, M.Y., and Li, L.X. (2019). Dynamic damage assessment of float glass under blast loading. *Advances in Structural Engineering*, *22*(11), 1-13. doi:10.1177/1369433219845691.